First commissioning of the ARES focusing system and its possible upgrade for accelerator R&D experiment

Dissertation

zur Erlangung des Doktorgrades
an der Fakultät für Mathematik, Informatik und Naturwissenschaften
Fachbereich Physik
der Universität Hamburg

vorgelegt von

Sumera Yamin

Hamburg
2021

Gutachter/innen der Dissertation	Dr. Ralph Aßmann Prof. Dr. Wolfgang Hillert
Zusammensetzung der Prüfungskommission	Dr. Ralph Aßmann Prof. Dr. Markus Drescher Dr. Klaus Floettmann Prof. Dr. Wolfgang Hillert Prof. Dr. Daniela Pfannkuche
Vorsitzende/r der Prüfungskommission	Prof. Dr. Daniela Pfannkuche
Datum der Disputation	24.11.2021
Vorsitzender des Fach-Promotionsausschusses Physik	Prof. Dr. Wolfgang Hansen
Leiter des Fachbereichs Physik	Prof. Dr. H. W. Günter Sigl
Dekan der Fakultät für Mathematik, Informatik und Naturwissenschaften	Prof. Dr. Heinrich Graener

Abstract

The SINBAD (Short INnovative Bunches and Accelerators at DESY) facility at DESY is a dedicated accelerator research and development project for the production of ultra-short electron bunches and development of novel high gradient accelerator technology. The ARES linac (Accelerator Research Experiment at SINBAD) is the first infrastructure implemented at SINBAD and has a focus on the generation and characterization of ultra-short, small emittance electron pulses, ultimately aiming at the few femto-second regime. Those ultra-short, low emittance electron bunches are required, amongst others, for testing laser based novel external injection concepts such as laser driven dielectric acceleration structures or plasma wakefields. This thesis focuses on the optimization of the required high quality beam transport and focusing from the electron source to the end of the linac or into the experimental area. As part of the thesis, an algorithm has been developed to optimize the beam transport from the photo-injector and through the travelling wave structures by a beam based alignment of the ARES focusing solenoids. The algorithm was validated against simulations with the ASTRA computer code. A MATLAB user interface was developed for beam commissioning and data taking at ARES. In various experimental campaigns offsets of solenoids were determined and a realignment implemented into the machine. At the end a very good alignment of the beam trajectory with the magnetic axis along the beamline has been achieved, a major step in successful commissioning of the ARES linac. The measurement results, the outcome of the data analysis and the alignment results are presented.

As part of the thesis the design of a focusing system was developed. The system would allow for injection into a laser wakefield acceleration experiment at ARES. For such an experiment, ultra-short bunches from ARES, ranging from sub-fs to few fs, would be injected into a plasma cell. The injection of short bunches requires strong transverse focusing to match the beam into small accelerating channels of the plasma. Transverse matching of the electron beam to the plasma channel prevents emittance growth in the finite energy spread beams. The conceptual design of a final focus system for injection into a laser plasma experiment at ARES is presented. The performance of the design is evaluated by means of ASTRA simulations of the beamline. The design includes sensitivity studies on relevant sources of error. The performed error analysis, which could be generalized for any quadrupole triplet, gives a useful estimate about the performance of the final focus system and suggests critical parameters in the implementation of the experiment.

Zusammenfassung

Die SINBAD Anlage (Short INnovative Bunches and Accelerators at DESY) ist eine Forschungs- und Entwicklungsplattform am DESY, die Projekte zur Erzeugung ultrakurzer Elektronenpakete und zur Entwicklung neuartiger Hochgradienten-Beschleuniger ermöglicht. Der ARES Linearbeschleuniger (Accelerator Research Experiment at SINBAD) ist die erste bei SINBAD implementierte Infrastruktur und konzentriert sich auf die Erzeugung und Charakterisierung von ultrakurzen Elektronenpulsen, mit kleiner Emittanz, die letztendlich auf das wenige Femtosekunden-Regime abzielen.Diese ultrakurzen Elektronenpakete mit niedriger Emittanz werden unter anderem zum Testen von laserbasierten neuartigen externen Injektionskonzepten wie lasergetriebenen dielektrischen Beschleunigungsstrukturen oder Plasma-Wakefields benötigt. Diese Arbeit konzentriert sich auf die Optimierung des erforderlichen qualitativ hochwertigen Strahltransports und der Fokussierung von der Elektronenquelle bis zum Ende des Linacs oder in den experimentellen Bereich. Im Rahmen der Diplomarbeit wurde ein Algorithmus entwickelt, um den Strahltransport vom Photoinjektor und durch die Wanderwellenstrukturen durch eine strahlbasierte Ausrichtung der ARES Fokussiermagnete zu optimieren. Der Algorithmus wurde gegen Simulationen mit dem Computercode von ASTRA validiert. Für die Strahlinbetriebnahme und Datenaufnahme bei ARES wurde eine MATLAB-Benutzeroberfläche entwickelt. In verschiedenen Versuchskampagnen wurden Versätze von Magnetspulen ermittelt und eine Neuausrichtung in die Maschine implementiert. Am Ende wurde eine sehr gute Ausrichtung der Strahltrajektorie mit der magnetischen Achse entlang der Strahllinie erreicht, ein wichtiger Schritt zur erfolgreichen Inbetriebnahme des ARES linac. Die Messergebnisse, das Ergebnis der Datenanalyse und die Alignment-Ergebnisse werden präsentiert.

Im Rahmen der Diplomarbeit wurde das Design eines Fokussiersystems entwickelt. Das System würde die Injektion in ein Laser-Wakefield-Beschleunigungsexperiment bei ARES ermöglichen. Für ein solches Experiment würden ultrakurze Bündel von ARES, die von subfs bis zu wenigen fs reichen, in eine Plasmazelle injiziert. Die Injektion kurzer Bunche erfordert eine starke transversale Fokussierung, um den Strahl in die beschleunigenden Plasmastrukturen mit sehr kleiner transversaler Akzeptanz einzukoppeln. Eine transversale Anpassung des Elektronenstrahls an die Plasmastruktur verhindert ein Emittanzwachstum in den Teilchenstrahlen. Die Anpassungsanforderungen hängen von der Stärke des Plasmakanals ab. Der konzeptionelle Entwurf eines finalen Fokussystems zur Injektion in ein Laser-Plasma-Experiment bei ARES wird vorgestellt. Die Leistungsfähigkeit des Entwurfs wird mit Hilfe von ASTRA-Simulationen bewertet. Die Untersuchungen beinhalten Sensitivitätsstudien zu relevanten Fehlerquellen. Die durchgeführte Fehleranalyse ermöglicht eine realistische Abschätzung der erreichbaren Strahlparameter mit dem entwickelten Fokussierungssystem und identifiziert kritische Parameter bei der Durchführung des Experimentes.

Contents

List of Figures

List of Tables

List of Acronyms

ACHIP	Accelerator on a chip international program
ARES	Accelerator research experiment at SINBAD
ASTRA	A space charge tracking algorithm
AXSIS	Frontiers in attosecond X-ray science: imaging and spectroscopy
BBA	Beam based alignment
BC	Bunch compressor
BPM	Beam position monitor
CERN	European organization for nuclear research
CSR	Coherent synchrotron radiation
DESY	Deutsches Elektronen-Synchrotron
DLA	Dielectric laser acceleration
DORIS	Doppel-Ring-Speicher
ELEGANT	Electron generation and tracking
EMQ	Electromagnetic quadrupoles
FEL	Free-electron laser
FLASH	Free-electron laser in Hamburg
FWHM	Full width at half maximum
LLRF	Low-level radio frequency
LWFA	Laser wakefield acceleration
PMQ	Permanent magnetic quadrupoles
REGAE	Relativistic electron gun for atomic exploration
RF	Radio frequency
rms	Root mean square
SC	Space charge
SINBAD	Short innovative bunches and accelerators at DESY
TWS	Traveling wave structure
WP	Working point

1
Introduction

In the past few decades, particle accelerators have emerged as great tools for cutting edge research in various fields of science. Accelerators have a broad range of applications in high energy physics as particle colliders, photon science, molecular and structural biology, medical imaging including cancers treatment, radiation generation, electron diffraction and microscopy to name a few. All these applications require different beam properties from purpose built accelerators in various shapes and sizes. The particle machines in present day research facilities are based on well established RF based accelerator technology [1]. The demand for higher energies, for example in the field of high energy physics and photon science, to perform breakthrough science is ever increasing. The electrical breakdown of metals in the presence of high electric fields limits the acceleration gradient to tens of MV/m. The demand for higher energies with state of the art beam properties make accelerator facilities large and expensive like CERN [2] , Eu-XFEL [3] and DESY [4] founded under national and international collaboration. Not only higher energies but also higher beam quality with striking properties, such as ultrashort bunch lengths from few fs to sub-fs to even attoseconds regime, are desired to realize new science. One application of such ultrashort beams is the injection into laser driven novel acceleration concepts like dielectric structures or plasma cells.

Novel acceleration concepts like dielectric laser acceleration (DLA) [5] and laser wakefield acceleration (LWFA) [6] have been a subject of extensive research in past few years [7, 8, 9, 10]. They leverage on increasing the accelerating gradients orders of magnitude higher than the conventional technology, hence reducing the size and cost of future accelerator facilities. Many important milestones such as achieving GeV energies in only cm scale range have been demonstrated [11, 12]. The quality and stability of beam from novel acceleration concepts have been improved over the recent years but they are still in developmental stage and fall behind the conventional accelerators in this regard. The beams from conventional accelerators provides stability to inject in the novel accelerator channels. This combination of conventional and novel concepts can increase our understanding of the novel technologies [13]. One such accelerator facility SINBAD, is being developed at DESY. It includes research in the field of ultrashort electron bunches and will host multiple independent experiments [14] on laser driven advanced high gradient acceleration techniques such as DLA [15], LWFA [16], THz-driven acceleration in the AXSIS

project [17] and LUX [18]. ARES, acronym for Accelerator Research Experiment at SINBAD, is a conventional S-band technology based linear electron accelerator (linac) with a photo-injector gun [19, 20]. It aims to deliver reliable high-brightness electron beams in 100 MeV to 150 MeV energy range, charge from 0.5 to 30 pC, ultrashort from fs to sub-fs bunch duration with excellent timing stability of ∼10 fs rms at 10-50 Hz repetition rate. This is ideal for injection into novel high-gradient acceleration devices with several advantages. The ARES linac on one hand will allow advancing R&D on the "conventional" production of high brightness ultrashort electron bunches. On the other hand, the well-characterized bunches can be used to explore compact novel accelerators, characterized by accelerating fields with short wavelengths and therefore require the injection in short "acceleration buckets". The ARES bunches have been designed to constitute excellent probes to measure the energy gain and the quality of the acceleration.

In a LWFA, an intense laser pulse propagating in a plasma generates charge separation through the excitation of wakefields, inducing strong electric fields. LWFAs can provide an accelerating gradient in the range of ∼100 GV/m, which is several orders of magnitude higher than what can be achieved with conventional RF technology. This reduces the size of the acceleration channel from meters to millimeters, to achieve GeV energy range, and hence offers the possibility of compact and cost-effective accelerators. Since the LWFA concept was first introduced [6], it has been a subject of extensive studies with significant progress in recent years [9, 10]. Many important milestones have been demonstrated such as achieving GeV energies in only cm scale [12]. Today's focus for these devices is to reach beam stability, similar to established RF accelerators, by deploying feedback control systems. Recently another milestone has been successfully demonstrated at DESY with 24 hours of stable operation of laser plasma acceleration [21]. The external injection LWFA experiment studied for ARES, investigated a possible step towards usable LWFA from a combination of reproducible conventional RF-based accelerator technology with the high gradient fields from plasma wakefields [13]. The RF-based technology allows for a precise manipulation of the phase space of the electron bunches before entering the plasma, hence providing independent control and quality adjustments as well as optimization of the plasma experiment. The beam quality in novel accelerators depends on the detailed parameters and quality of the injected beam e.g. bunch shape, bunch length, emittance, arrival time stability and beam energy. ARES provides the option of widely tunable working points (WP) and bunch shapes for external injection LWFA accelerator R&D.

This thesis is devoted to the optimization of focusing solenoids of the ARES linac to ensure high quality beam transport till the experimental area where it could be potentially injected into LWFA. The thesis also includes the studies for design and optimization of focusing system for LWFA experiment beamline. A beam based alignment algorithm has been developed for the solenoids at ARES. The developed alignment algorithm has been tested and used for aligning the solenoids during ARES commissioning. The alignment of focusing solenoids enables the ARES beam to achieve its design parameters and maintains the beam quality till the experimental area. In the later part of the thesis, a design of the final focus system is presented, which enables the ARES beam to focus efficiently into tiny accelerating structures of a plasma

cell for efficient acceleration and to get usable beam quality after it has been accelerated by the plasma. An important feature of advanced acceleration concepts, like LWFA, is the small size of the acceleration channel in both transverse and longitudinal dimensions. This results in stringent requirements on the transverse and longitudinal sizes of the externally injected beam for efficient acceleration. Moreover applications such as FEL requires peak currents on the order of kA. This makes the beam transport and focusing more challenging due to space-charge effects at low energy beams in the 100 to 150 MeV range and ultrashort, fs to sub-fs, duration. The thesis is organized in the following ways:

Chapter 2 briefly introduces the standard theory of accelerator physics relevant to the work presented in the thesis. The simulation codes used for the work are also discussed. Chapter 3 describes an over view of the ARES linac at the SINBAD facility. The novel acceleration concepts with dielectric laser acceleration and laser induced plasma acceleration are introduced with corresponding experimental area planned at ARES.

In Chapter 4 the algorithm developed for the beam based alignment of solenoids of ARES is discussed. The developed routine is bench marked with detailed simulations for ARES beam. Moreover, the possible sources of errors in the alignment studies are introduced and their impacts are described in detail. The author also participated in the commissioning of ARES linac with regular shifts. After the ARES beam has been commissioned, the measurements were performed for beam based alignment of solenoids of ARES. The measurement results are discussed in detail.

Once the ARES beam has been optimized to achieve the desired beam parameters, it is transported further downstream to the experimental area where a potential laser induced laser plasma acceleration could be performed. In chapter 6 various working points of ARES beam, with different range of beam parameters, have been optimized and transported to the injection of a plasma cell. A final focus system has been designed for beam matching into small acceleration channel of the plasma. The matching criterion and constraints for the LWFA beamline are discussed in detail. The studies also include the focusing and optimization of the working points of ARES for a possible future energy upgrade where a third travelling wave structure could be installed in the context of the ATHENAe project [22].

Chapter 7 summarizes the work done in the thesis and points to the importance and potential applications of the developed algorithm for BBA of focusing solenoids of an accelerator facility and the final design of the focusing system for LWFA experiment at ARES.

2

Theory of Charged Particle Beams

In this chapter, basic theory of charged beam dynamics is reviewed.

2.1. Dynamics of charged particle beams

Accelerator physics deals with the interaction of charged particles with externally applied electromagnetic fields and fields generated by other charged particles. Understanding the physics behind this interaction allows for the accurate prediction of charged particle beam behavior in particle accelerators. In accelerator physics, the dynamics of a charge particle beam is described in a six dimensional phase space system [23]. The coordinated of this six dimensional phase space system are in general represented as

$$\mathbf{X} = \begin{pmatrix} x \\ x' \\ y \\ y' \\ z \\ \delta \end{pmatrix} \tag{2.1}$$

Here x and y are the horizontal and vertical distances from the reference trajectory s, $x' = p_x/p_z$ and $y' = p_y/p_z$ where p_x, p_y and p_z are the particle momentum in their respective directions. z is the longitudinal distance along the reference trajectory. A reference particle is defined for this reference trajectory which in real beams corresponds to center of mass of the distribution. The quantity $\delta = \Delta p/p_o$ represents the relative momentum spread with p_o being the reference momentum and $\Delta p = p - p_o$. It is worthwhile to mention that the coordinate space using (x, x', y, y') to describe the transverse motion instead of (x, p_x, y, p_y) is also referred to as trace space with later being called phase space. The coordinate vector $\mathbf{X}$ can be written for every particle in the beam distribution and hence allows to determine the statistical properties. The covariance matrix for this six dimensional phase space is given by

$$\Sigma = \begin{pmatrix} \Sigma_{XX} & \Sigma_{XY} & \Sigma_{XZ} \\ \Sigma_{YX} & \Sigma_{YY} & \Sigma_{YZ} \\ \Sigma_{ZX} & \Sigma_{ZY} & \Sigma_{ZZ} \end{pmatrix} = \begin{pmatrix} \langle x^2 \rangle & \langle xx' \rangle & \langle xy \rangle & \langle xy' \rangle & \langle xz \rangle & \langle x\delta \rangle \\ \langle xx' \rangle & \langle x'^2 \rangle & \langle x'y \rangle & \langle x'y' \rangle & \langle x'z \rangle & \langle x'\delta \rangle \\ \langle xy \rangle & \langle x'y \rangle & \langle y^2 \rangle & \langle yy' \rangle & \langle yz \rangle & \langle y\delta \rangle \\ \langle xy' \rangle & \langle x'y' \rangle & \langle yy' \rangle & \langle y'^2 \rangle & \langle y'z \rangle & \langle y'\delta \rangle \\ \langle xz \rangle & \langle x'z \rangle & \langle yz \rangle & \langle y'z \rangle & \langle z^2 \rangle & \langle z\delta \rangle \\ \langle x\delta \rangle & \langle x'\delta \rangle & \langle y\delta \rangle & \langle y'\delta \rangle & \langle z\delta \rangle & \langle \delta^2 \rangle \end{pmatrix} \tag{2.2}$$

where $\Sigma_{XX}...\Sigma_{ZZ}$ are the 2×2 covariance matrices. The beam covariance matrix completely characterizes the beam distribution including correlations between the planes. Here $\langle\rangle$ defines the central second moment of the particle distribution. For example for x the central second moment is calculated by equation 2.3. Similarly, it can be calculated for other terms as well.

$$\langle x^2 \rangle = \frac{\sum x^2}{n} - \left(\frac{\sum x}{n} \right)^2 \tag{2.3}$$

$$\langle xx' \rangle = \frac{\sum xx'}{n} - \frac{\sum x \sum x'}{n^2} \tag{2.4}$$

$$\langle x'^2 \rangle = \frac{\sum x'^2}{n} - \left(\frac{\sum x'}{n} \right)^2 \tag{2.5}$$

The rms parameters for beam distribution can be calculated by

$$\sigma_x = \sqrt{\langle x^2 \rangle}, \quad \sigma_y = \sqrt{\langle y^2 \rangle}, \quad \sigma_z = \sqrt{\langle z^2 \rangle}, \quad \sigma_\delta = \sqrt{\langle \delta^2 \rangle} \tag{2.6}$$

If there is no correlation between the evolution of phase space coordinates in x and y planes, the horizontal, vertical and longitudinal motion are independent of each other. The off diagonal terms in equation 2.2 are zero and can be treated as three subspace vectors separately.

$$\mathbf{x} = \begin{pmatrix} x \\ x' \end{pmatrix} \quad \text{transverse phase space in x}$$

$$\mathbf{y} = \begin{pmatrix} y \\ y' \end{pmatrix} \quad \text{transverse phase space in y}$$

$$\mathbf{z} = \begin{pmatrix} z \\ \delta \end{pmatrix} \quad \text{longitudinal phase space}$$

In the following subsections, the beam properties from the phase space vectors are discussed.

2.1.1. Emittance

One of the most important property to characterize a beam is the emittance. It is a measure of average spread of electrons in phase space. The numerical values multiplied by π is equal to the area occupied by the beam in the respective phase plane. Liouville's theorem states that in a Hamiltonian system, the density in phase space of non-interacting particles, measured along the particle trajectory is invariant [23]. This implies that the phase space volume of a beam along any trajectory in six dimensional phase space is

a conserved quantity provided only conservative forces are present. Liouville's theorem is also valid for the transverse and longitudinal sub spaces if they are uncoupled with each other. Liouville's theorem provides a powerful concept to describe a beam in phase space. Knowledge of the area occupied by particles in phase space at the start of a beam transport line allows to specify the location and distribution of the beam at any other point along the transport line without having to calculate the trajectory of every individual particle. Liouville's theorem is the outcome of Hamiltonian mechanics which uses the three space (x, y, z) and three momentum coordinates (p_x, p_y, p_z) instead of trace space coordinates (x', y', δ) as defined in previous section. The trace space emittance is preserved as long as p_o is a constant and no magnetic vector potential is present. For smaller energy spread beams, in the absence of solenoidal and accelerating fields, this assumption is valid. This is mostly the case in high energy transport lines in conventional accelerators where trace space emittance is also conserved.

The trace space emittance is defined as

$$\epsilon_{tr} = \sqrt{\langle x^2 \rangle \langle x'^2 \rangle - \langle x x' \rangle^2} \tag{2.7}$$

Since the trace space emittance is momentum dependent and decreases as the momentum increases, often referred to as adiabatic damping of the emittance. It is useful to define the momentum independent normalized emittance as

$$\epsilon_{n,tr} = \beta\gamma\epsilon_{tr} \tag{2.8}$$

where β is the average speed relative to speed of light c and γ is the Lorentz factor. Statistically, the normalized rms emittance, also referred to as beam emittance, is defined as

$$\epsilon_{n,rms} = \frac{1}{m_e c}\sqrt{\langle x^2 \rangle \langle (p_x)^2 \rangle - \langle x p_x \rangle^2} \tag{2.9}$$

The geometric emittance is defined as

$$\epsilon_{rms} = \frac{\epsilon_{n,rms}}{\beta\gamma} \tag{2.10}$$

In general the beam emittance and trace space emittance are not equal specially in beams with high energy spread and the divergence. This can happen in bunch compressors and in novel accelerators like plasma cells where energy spread is large. The normalized rms emittance is usually calculated for electron beams and is used through out this work unless otherwise specified.

Another term associated with the emittance is 'Slice emittance'. Slice emittance usually refers to emittance calculated for a specified longitudinal slice of the beam. This eliminates the emittance contribution due to correlations in the phase space along the bunch. The slice emittance is an important parameter for free electron laser (FEL) facilities and for accelerations in a plasma cell.

2.1.2. Beam brightness

Another important parameter to determine the beam quality for high-current low emittance beam applications, such as FELs, is beam brightness. Steenboergen [24] introduced the beam brightness definition as

$$B = \frac{I}{V_4} \tag{2.11}$$

Here I is the current and V_4 is the hypervolume occupied by a beam distribution in four dimensional phase space. Beam brightness measures the achievable current density for a given angular acceptance. Higher the phase space density of an electron beam, the higher is the beam brightness. Since the volume of beam in 4D phase space is related to transverse beam emittance, beam brightness can be calculated in different ways by using various beam emittance definitions. The relation by [25] is commonly used to calculate beam brightness as

$$B_{5D} = \frac{\eta I}{\pi^2 \epsilon_x \epsilon_y} \tag{2.12}$$

where η is a form factor of order unity that depends on the definitions of the hyper volume used. The beam brightness may be normalized by using the normalized emittance values in the relation above. This represents the 5D brightness since the longitudinal beam property is included via the current. In high average power applications, 4D brightness is used, by introducing bunch charge rather than current. This is also the case for bunch compressors, where bunches are compressed to shorten the bunch length and increase the final charge. The 4D transverse brightness is then defined as

$$B_{4D} = \frac{\eta Q}{\pi^2 \epsilon_x \epsilon_y} \tag{2.13}$$

The average 5D brightness is then $B_{4D} \cdot f$ where f is the repetition rate of the source [26].

2.1.3. Courant Snyder parameters

The linear motion of a charged particle in a periodic system, with periodic focusing function K(s) is described by Hills's equation, named after the astronomer George William Hill, as

$$x'' + K(s)x = 0 \tag{2.14}$$

The solution of Hills equation is a harmonic oscillator of the form [23, 1].

$$x'(s) = A\sqrt{\beta(s) cos\left(\phi(s) + \phi_o\right)} \tag{2.15}$$

which describes the sc called transverse betatron oscillations around the design trajectory. Here $\beta(s)$ and $\phi(s)$ are amplitude and phase functions respectively. $\phi(s)$ defines the phase advance between the start position and a given longitudinal position s on the design trajectory. The constants A and ϕ_o are

dependent on initial conditions. The amplitude and phase functions $\beta(s)$ and $\phi(s)$ are related by

$$\phi(s) = \int \frac{ds}{\beta(s)} \tag{2.16}$$

In accelerator physics, the two other functions are defined as

$$\alpha(s) = -\frac{1}{2}\frac{d\beta(s)}{ds} \tag{2.17}$$

$$\gamma(s) = \frac{\left(1+\alpha(s)^2\right)}{\beta(s)} \tag{2.18}$$

The quantities $\alpha(s)$, $\beta(s)$ and $\gamma(s)$ are called "Courant Snyder parameters" or "Twiss parameters" [27]. The solution x given in equation 2.15 and its derivative x', expressed in terms of Courant Snyder parameters, satisfies the equation

$$\gamma(s)x^2 + \alpha(s)xx' + \beta(s)x'^2 = A^2 \tag{2.19}$$

Equation 2.19 is the general equation of ellipse with area πA^2 centered on the (x, x') phase space. As discussed in section 2.1.1, the area occupied in trace space is defined as emittance. Hence defining area of ellipse as trace space emittance, $A^2 = \epsilon_{tr}$ and amplitude of oscillation as the beam size $A\sqrt{\beta(s)} = \sigma_x$, equation 2.19 can be generalized to define the collective trajectory of beam distribution as

$$\gamma_x x^2 + 2\alpha_x xx' + \beta_x x'^2 = \epsilon_{tr} \tag{2.20}$$

The ellipse is visualized in (x,x') phase space in figure 2.1

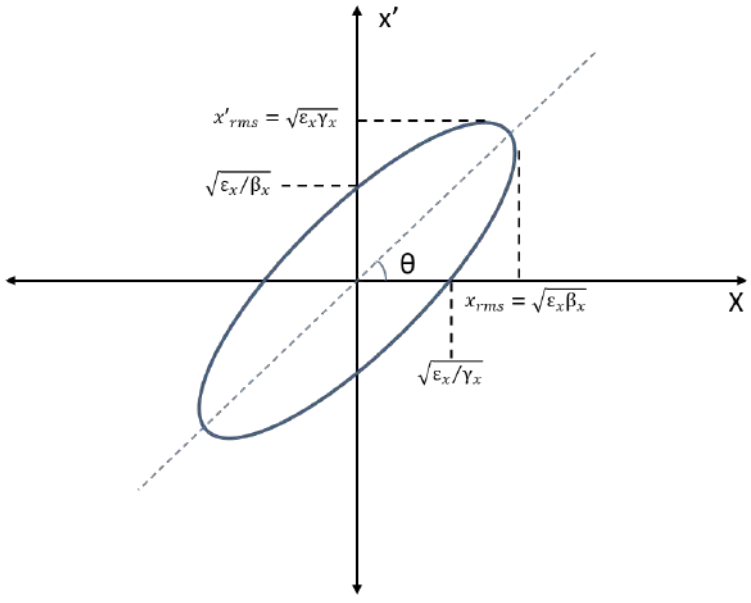

Figure 2.1.: Transverse phase space ellipse with coordinate definitions. Schematics adopted from [28].

Twiss parameters are then given by

$$\beta_x = \frac{\langle x^2 \rangle}{\epsilon_{tr}} \quad \gamma_x = \frac{\langle x'^2 \rangle}{\epsilon_{tr}} \quad \alpha_x = -\frac{\langle xx' \rangle}{\epsilon_{tr}} \tag{2.21}$$

Twiss parameters α, β and γ relates to the shape of the ellipse. β is related to beam size in x, γ is related to beam size in x' or angular spread of the beam and alpha is related to the tilt angle of the ellipse xx'. While the above-mentioned theory deals with circular accelerators, the results apply equally to beam transport systems in linear accelerators as well[1, 23].

2.1.4. Dispersion

Equation 2.14 describes the motion of a particle with no momentum deviation. If this is not the case, Hill's equation including the first order momentum perturbation term becomes

$$x'' + K(s)x = \frac{\delta}{\rho(s)'} \tag{2.22}$$

Here $\rho(s)$ is the bending radius of the reference orbit. The general solution can be represented in matrix form as

$$\begin{pmatrix} x_s \\ x'_s \\ \delta_s \end{pmatrix} = \begin{pmatrix} C(s) & S(s) & D(s) \\ C'(s) & S'(s) & D'(s) \\ 0 & 0 & 1 \end{pmatrix} \begin{pmatrix} x_0 \\ x'_0 \\ \delta_0 \end{pmatrix} \tag{2.23}$$

where $D(s)$ and $D'(s)$ are the dispersion function and its derivative respectively. The dispersion function correlates the momentum deviation to the transverse position of a particle at position s along the trajectory, where the dispersion function is given by

$$D(s) = S(s) \int_{s_0}^{s} \frac{C(\tilde{s})}{\rho(\tilde{s})} d(\tilde{s}) - C(s) \int_{s_0}^{s} \frac{S(\tilde{s})}{\rho(\tilde{s})} d(\tilde{s}) \tag{2.24}$$

The dispersion affects the beam spot size along the particle trajectory. The higher the dispersion, the bigger will be the beam size along the trajectory. In other words, the higher the relative momentum deviation, the bigger will be the relative displacement of particle from the axis. For example, the path of a particle passing through a dipole magnet is momentum dependent hence a dipole introduces dispersion in a beam. The distance of a particle from the reference trajectory is proportional to its energy and is given by

$$x_\delta = D\delta \tag{2.25}$$

2.2. Transfer matrix formalism for beam line elements

In linear beam optics, each beamline element is represented by a transfer matrix defined by the following relation

$$\mathbf{x} = M \cdot \mathbf{x_0} \tag{2.26}$$

where $\mathbf{x_0} = \begin{pmatrix} x_0 \\ x_0' \end{pmatrix}$ is the initial phase space coordinate. The transfer matrices for the beam line elements can easily be derived by solving the Hill's equation of motion 2.14. The general solution is [29]

$$x(s) = C(s)x_0 + S(s)x_0' \tag{2.27}$$

where $C(s)$ and $S(s)$ are the sine and cosine functions and K is the focusing strength of the lattice. The $C(s)$ and $S(s)$ depends on the magnitude and direction of K.

$$\begin{aligned} &K \geq 0 : \\ &\quad C(s) = cos\left(\sqrt{Ks}\right) \\ &\quad S(s) = \frac{1}{\sqrt{K}} sin\left(\sqrt{Ks}\right) \\ &K \leq 0 : \\ &\quad C(s) = cosh\left(\sqrt{|K|s}\right) \\ &\quad S(s) = \frac{1}{\sqrt{|K|}} sin\left(\sqrt{|K|s}\right) \end{aligned} \tag{2.28}$$

Here $K < 0$ corresponds to defocusing magnet. The general solution x and its derivative x' from equation 2.27 are

$$\begin{aligned} x(s) &= C(s)x_0 + S(s)x_0' \\ x'(s) &= C'(s)x_0 + S'(s)x_0' \end{aligned}$$

which can be rewritten in matrix form as

$$\begin{pmatrix} x(s) \\ x'(s) \end{pmatrix} = \begin{pmatrix} C(s) + S(s) \\ C'(s) + S'(s) \end{pmatrix} \begin{pmatrix} x_0(s) \\ x_0'(s) \end{pmatrix} = M \begin{pmatrix} x_0(s) \\ x_0'(s) \end{pmatrix} \tag{2.29}$$

The 2x2 matrix for a drift space of length l can be easily derived by taking the limit $K \to 0$ in equation 2.29, which leads to

$$\begin{pmatrix} 1 & l \\ 0 & 1 \end{pmatrix} \tag{2.30}$$

The Twiss parameters, at a given point in a lattice can be calculated using a similar matrix formalism. Exploiting the conservation of emittance under Liouville's theorem, and using equation 2.26 and 2.20, the Twiss parameters transforms as

$$\begin{pmatrix} \beta \\ \alpha \\ \gamma \end{pmatrix} = \begin{pmatrix} C^2(s) & -2S(s)C(s) & S^2(s) \\ -C(s)C'(s) & S'(s)C(s) + S(s)C'(s) & -S(s)S'(s) \\ C'^2(s) & -2S'(s)C'(s) & S'(s)^2 \end{pmatrix} \begin{pmatrix} \beta_0 \\ \alpha_0 \\ \gamma_0 \end{pmatrix} \tag{2.31}$$

Alternatively, matrix elements of transfer matrix can also be written in terms of known initial and final Twiss parameters as

$$M = \begin{pmatrix} \sqrt{\frac{\beta}{\beta_0}}\,(cos\Delta\phi + \alpha_o sin\Delta\phi) & \sqrt{\beta\beta_0}sin\Delta\phi \\ -\frac{1+\alpha\alpha_0}{\sqrt{\beta\beta_0}}sin\Delta\phi + \frac{\alpha_0-\alpha}{\sqrt{\beta\beta_0}}cos\Delta\phi & \sqrt{\frac{\beta_0}{\beta}}\,(cos\Delta\phi - \alpha sin\Delta\phi) \end{pmatrix} \tag{2.32}$$

The transformation matrix can be extended to six dimensional phase space, where generally, it is written as

$$\mathbf{R} = \begin{pmatrix} R_{11} & R_{12} & R_{13} & R_{14} & R_{15} & R_{16} \\ R_{21} & R_{22} & R_{23} & R_{24} & R_{25} & R_{26} \\ R_{31} & R_{32} & R_{33} & R_{34} & R_{35} & R_{36} \\ R_{41} & R_{42} & R_{43} & R_{44} & R_{45} & R_{46} \\ R_{51} & R_{52} & R_{53} & R_{54} & R_{55} & R_{56} \\ R_{61} & R_{62} & R_{63} & R_{64} & R_{65} & R_{66} \end{pmatrix} \tag{2.33}$$

The 6D transfer matrix of a drift length l is

$$M_{drift} = \begin{pmatrix} 1 & l & 0 & 0 & 0 & 0 \\ 0 & 1 & 0 & 0 & 0 & 0 \\ 0 & 0 & 1 & l & 0 & 0 \\ 0 & 0 & 0 & 1 & 0 & 0 \\ 0 & 0 & 0 & 0 & 1 & l/\gamma^2 \\ 0 & 0 & 0 & 0 & 0 & 1 \end{pmatrix} \tag{2.34}$$

The particle distribution over a drift length is sheared in transverse phase space. The particle positions in a drift space is energy dependent specially at low energies. This term, known as R_{56}, connecting the longitudinal displacement to momentum deviation, is utilized in magnetic chicanes for bunch compression.

The general transfer matrix given in equation 2.33 do not include non linear elements. The nonlinear terms can be included, in the form of a Taylor expansion. Conventionally, the coefficients of linear terms are denoted as R_{ij} , second order terms as T_{ijk} and third order term as U_{ijkl}. The relationship between the final phase space coordinate vector X and the initial phase space coordinate vector X_0, including non-linear terms, can be extended to

$$X_i = \sum_{j=1}^{6} R_{ij}X_{jo} + \sum_{j=1}^{6}\sum_{k=1}^{6} T_{ijk}X_{jo}X_{ko} + \sum_{j=1}^{6}\sum_{k=1}^{6}\sum_{l=1}^{6} U_{ijkl}X_{jo}X_{ko}X_{lo} \tag{2.35}$$

2.3. Magnets for beam transport

In an accelerator, external fields are applied to transport an electron beam. The Lorentz force responsible for bending and focusing of charged particle beams to keep it on the design orbit is given by the equation 2.36

$$F = q \cdot (E + (v \times B)) \tag{2.36}$$

where E and B is the electric and magnetic field seen by the particle with charge q travelling with

velocity v. Magnetic fields are used in accelerators to provide the forces for bending and focusing of charged particle beams. Electric fields can also be used, in principle, but at higher momentum closer to the speed of light magnetic field is much more efficient. For a magnetic field of 1 T, force acting on a relativistic particle with $v \approx c = 3x10^8 m/s$ according to equation 2.36 is 300 MV/m. An equivalent force from a static electric field is far beyond the technical limits set by the field breakdown and discharges. In some particular cases, e.g low energy heavy ion rings or few keV range applications for electron beam, electrostatic fields can be the more efficient choice.

Consider a moving charged particle with momentum p in a magnetic field. The Lorentz forced is confronted by the centripetal force, for a bending radius ρ given by equation 2.37.

$$F = \frac{mv^2}{\rho} \tag{2.37}$$

This leads to equation 2.38

$$B\rho = \frac{p}{q} \tag{2.38}$$

where the quantity $B\rho$ is called beam rigidity and is the fundamental starting point to define the requirements of a magnet from particle momentum and charge.

For a 2D cross section of an infinitely long magnet, the horizontal and vertical magnetic field components B_x and B_y can be expressed as complex Fourier series

$$B_y + iB_x = \sum_{n=1}^{\infty} (B_n + iA_n) \cdot (x + iy)^{(n-1)} \tag{2.39}$$

where B_n and A_n are the so called multipoles of the field and determine the shape of the field lines. The magnets for particle accelerators are designed to minimize the undesirable higher order multipoles and to achieved desired design parameters within technical limits. Iron dominated magnets are most commonly used for beam transport. Only where very high particle energies and magnetic fields are required, super conducting magnets are used. They can reach field values much higher compared to maximum field in an iron dominated magnet of about 1.6 T. The saturation of ferromagnetic material imposes a maximum limit on the strength of iron dominated magnets. However, for most electron accelerators up to few tens of GeV energy ranges, the design needs can be accommodated within this limit. The commonly used magnets for beam bending and focusing in a particle accelerators are briefly described below.

2.3.1. Dipoles

Dipoles magnets have a constant field between the two poles and are used for bending the charged particle beams. The dipole field corresponds to first term of equation 2.39. From equation 2.39, a magnetic field in which only the B_1 term is non zero corresponds to a perfect dipole field, which is constant in amplitude and direction and is oriented in y direction, so $B_x = 0$; $B_y = 1$. This bends the particle in the plane of

the accelerator i-e the horizontal plane. This is usually called a *normal* dipole in contrast to *skew* dipole. The skew dipole field results from a magnet for which which only A_1 term of equation 2.39 is non zero resulting in $B_y = 0; B_x = 1$, providing bending in the vertical direction. In general, normal magnets are used in the accelerators. In case of pure normal multipoles, the field amplitudes from equation 2.39 can be written as function of the radius r

$$B_{x,y} = B_n \cdot (y, x)^{(n-1)} \tag{2.40}$$

Dipole magnets are commonly of two types: Sector magnet and bending magnet. In a sector magnet, the beam trajectory is perpendicular to the dipole field while in a rectangular magnet, the beam enters at an angle. The dipole field also has a small geometric focusing effect. In a uniform field sector magnet particles travel longer paths for x $>$ 0 and a shorter path for x $<$ 0 leading to a focusing effect in the deflecting plane. In the non deflecting plane there is no focusing [23]. The rectangular magnet will focus the beam in the perpendicular plane and defocus in the other plane.

The linear transfer matrix for a sector dipole magnet deflecting the beam in the horizontal plane is [30]:

$$M_{dipole} = \begin{pmatrix} cos\theta & \rho sin\theta & 0 & 0 & 0 & \rho\,(1 - cos\theta) \\ -1/\rho sin\theta & cos\theta & 0 & 0 & 0 & sin\theta \\ 0 & 0 & 1 & \rho\theta & 0 & 0 \\ 0 & 0 & 0 & 1 & 0 & 0 \\ -sin\theta & -\rho\,(1 - cos\theta) & 0 & 0 & 1 & \rho\theta/\gamma^2 - rho\,(\theta - sin\theta) \\ 0 & 0 & 0 & 0 & 0 & 1 \end{pmatrix} \tag{2.41}$$

2.3.2. Quadrupole

A quadrupole magnets is used to focus the charged particle beam. A quadrupole magnet consists of four poles in which the magnetic field amplitude increases linearly with the distance from the center deduced from equation 2.40 as $B_y = G.x \quad and \quad B_x = G.y$ where coefficient B_2 is called the gradient G of the quadrupole. The quadrupole strength K is defined as the ratio between gradient and beam rigidity (in m^{-2}) given by equation 2.42.

$$K = \frac{G}{B\rho} \tag{2.42}$$

The focal length of the quadrupole is defined as $f = 1/Kl$ where l is the length of the quadrupole. A quadrupole magnet is always focusing in one plane and defocusing in the other plane. Hence they are used in combination as doublet or triplets to attain net focusing. If the field is vertical on the mid plane, the quadrupole focuses in the horizontal plane and is called the normal quadrupole as opposed to skew quadrupoles in which the field is horizontal on the mid plane. Using a general solution of Hill's equation 2.27 and 2.28, the linear transfer matrix for a quadrupole magnet of length l, focusing in x and

defocusing in y plane, is represented as following [30]

$$M_{quad} = \begin{pmatrix} cos\left(\sqrt{K}l\right) & \frac{sin\left(\sqrt{K}l\right)}{\sqrt{K}} & 0 & 0 & 0 & 0 \\ -\sqrt{K}sin\left(\sqrt{K}l\right) & cos\left(\sqrt{K}l\right) & 0 & 0 & 0 & 0 \\ 0 & 0 & cosh\left(\sqrt{K}l\right) & \frac{sinh\left(\sqrt{K}l\right)}{\sqrt{K}} & 0 & 0 \\ 0 & 0 & \sqrt{K}sinh\left(\sqrt{K}l\right) & cosh\left(\sqrt{K}l\right) & 0 & 0 \\ 0 & 0 & 0 & 0 & 1 & L/\gamma^2 \\ 0 & 0 & 0 & 0 & 0 & 1 \end{pmatrix} \tag{2.43}$$

It should be noted that the K is energy dependent. Particles with different energies will be focused at different positions leading to phase advance. This variation is known as chromaticity and can lead to undesirable orbit errors especially in circular accelerators. The chromatic effects can be compensated by applying higher order sextupole magnets.

2.3.3. Solenoids

Solenoids are made by electrical conductors wound in the form of a helix and used for focusing at low energies. Solenoids can be built by an iron less magnets or can have an external ferromagnetic yoke for shielding and increasing the magnetic field uniformity. Solenoid provides a focusing force simultaneously in both horizontal and vertical planes. The beam in a solenoidal field also experience rotation in (x,y) space. The total transfer matrix of a solenoid is given in equation 2.44 which can be written as a product of rotation matrix M_{rot} and M_{foc} [31, 28]. The focusing with a solenoid forms an important part of this work and is discussed in detail in chapter 4. The derivation of transfer matrix of a solenoid is given in appendix A.

$$M_{sol} = \begin{pmatrix} cos^2(Kl) & sin(Kl)cos(Kl)/k & sin(Kl)cos(Kl) & sin^2(Kl)/K & 0 & 0 \\ -Ksin(Kl)cos(Kl) & cos^2(Kl) & -Ksin^2(Kl) & sin(Kl)cos(Kl) & 0 & 0 \\ -sin(Kl)cos(Kl) & -sin^2(Kl)/K & cos^2(Kl) & sin(Kl)cos(Kl)/K & 0 & 0 \\ Ksin^2(Kl) & -sin(Kl)cos(Kl) & -Ksin(Kl)cos(Kl) & cos^2(Kl) & 0 & 0 \\ 0 & 0 & 0 & 0 & 1 & L/\gamma^2 \\ 0 & 0 & 0 & 0 & 0 & 1 \end{pmatrix} \tag{2.44}$$

where

$$M_{rot} = \begin{pmatrix} cos\,(Kl) & 0 & sin\,(Kl) & 0 & 0 & 0 \\ 0 & cos\,(Kl) & 0 & sin\,(Kl) & 0 & 0 \\ -sin\,(Kl) & 0 & cos\,(Kl) & 0 & 0 & 0 \\ 0 & -sin\,(Kl) & 0 & cos\,(Kl) & 0 & 0 \\ 0 & 0 & 0 & 0 & 1 & L/\gamma^2 \\ 0 & 0 & 0 & 0 & 0 & 1 \end{pmatrix}$$

$$M_{foc} = \begin{pmatrix} cos\,(Kl) & sin\,(Kl)\,/K & 0 & 0 & 0 & 0 \\ -Ksin\,(Kl) & cos\,(Kl) & 0 & 0 & 0 & 0 \\ 0 & 0 & cos\,(Kl) & sin\,(Kl)\,/K & 0 & 0 \\ 0 & 0 & -Ksin\,(Kl) & cos\,(Kl) & 0 & 0 \\ 0 & 0 & 0 & 0 & 1 & L/\gamma^2 \\ 0 & 0 & 0 & 0 & 0 & 1 \end{pmatrix} \tag{2.45}$$

here $K = eB/2\rho$ is the focusing strength of the solenoid of length l and Kl is the angle of rotation.

2.4. Collective effects in charged particle beams

The above mentioned theory does not include the interaction between the individual particles. In reality, the charged particles within a beam interacts via their electromagnetic fields. This interaction is called space charge (SC) effect. The charges in a beam produces mutually repulsive electric fields that reduces the effects of external focusing forces, and also magnetic fields that give rise to attractive forces. SC can effect in both transverse planes and the longitudinal plane of the phase space.

In a cylindrically symmetric charge distribution $q\rho(r)$ with q being the charge of an electron, moving with constant velocity $v = \beta c$, the radial electric and magnetic field acting on the electron is given by [1]

$$\begin{aligned} E_r &= \frac{q}{\epsilon_o r}\int_0^r r\rho(r)dr \\ B_\theta &= \frac{q\nu\mu_o}{r}\int_0^r r\rho(r)dr \end{aligned} \tag{2.46}$$

where ϵ_o is the permittivity in free space and μ_o is the vacuum permeability. The force experienced by an electron is given by the Lorentz Force in equation 2.36. Using $c^2 = 1/(\epsilon_o\mu_o)$ and $(1-\beta^2) = \gamma^2$ in equation 2.36, the radial force on an electron at a radius r by the rest of the bunch charge is given by:

$$F_r = q\,(E_r - vB_\theta) = q\frac{E_r}{\gamma^2} \tag{2.47}$$

This equation tells us that with increasing beam energy the SC force decreases. This can be explained by the fact that at higher energies, the self induced magnetic field becomes more significant mitigating the effects of the electric fields. It can also be seen that the SC effects is proportional to the charge density of the beam. A thorough derivation of the SC terms by solving the paraxial beam envelope

equation can be found in many texts [23, 32, 33]. SC forces are given by the composition of linear and non linear functions of the displacement from the beam centroid. The SC forces increase the divergence by $\Delta x' = Ax^n$, therefor trace space emittance equation 2.7 becomes

$$\epsilon_{tr} = \sqrt{\langle x^2\rangle\langle x'^2\rangle - \langle xx'\rangle^2 + A^2\left(\langle x^2\rangle\langle x^{2n}\rangle\right) - \langle x^{1+n}\rangle^2} \tag{2.48}$$

where A and n are constants. From equation 2.48, it is evident that for linear SC force (n=1), only defocusing of the the beam occurs but emittance is conserved (as the last two terms in equation 2.48 cancels each other). However, the non linear SC force components increase the emittance by distorting the phase space distribution [33]. The linear term may also leads to projected emittance growth as linear forces can lead to misalignment of longitudinal slices in transverse phase space if the beam is not perfectly matched to the focusing channel and therefore the envelope is not constant. These envelope oscillations allow for the alignment of slices at low energies for example in photoinjectors, leading to emittance compensation using a solenoid [32, 34].

Another effect that can happen in a charged particle beam is the emission of synchrotron radiation. The radiation can be very useful as many accelerators, used as light sources, are built for the purpose of producing synchrotron radiations. However, this can also lead to perturbations in phase space when synchrotron radiation is not desired for example in injectors. Coherent Synchrotron Radiation (CSR) is emitted when short bunches radiates at wavelengths much longer than the bunch length. The CSR can lead to correlated energy spread as well as loss in bunch energy because of emitted radiation. This energy redistribution is coupled to the transverse dimensions in a dispersive section of the beamline. As a result, the transverse distribution of the bunch can spread out leading to transverse emittance growth. The analytical models for CSR take into account the 1D and 3D case. For the 1D model, the radial spot size of the beam σ_r should be smaller compared to the bunch length σ_z. The CSR effects can be studied in some simulation codes for example in Elegant [35] and Impact-T[36] although 3D models are computationally expensive and most simulation codes adopts only 1D models e.g. in Elegant.

2.5. Simulation codes for particle tracking

Simulation tools are of tremendous importance to develop the understanding of the dynamics of charged particle beams. They provide information and feedback to design and successfully operate the particle accelerators by simulating physical phenomena close enough to reality based on analytical theory before actual experiments could take place. Complete particle distributions can be extracted from simulations so beam dynamics can be studied in detail. Move over one can toggle the collective effects, such as space charge forces, Coherent Synchrotron Radiation (CSR), higher order optics and wake fields etc, so the individual impacts can be studied in detail. Different parameters of beam and beamline elements can be scanned and adjusted to ascertain the effects on beam properties, leading to optimization of the results. However, results can differ from reality as certain assumptions are made based on analytical models.

Some of these collective effects and the optimization of the beam line design can be computationally expensive. Hence a compromise between accuracy of the results and computational cost, in terms of computing power and time, is to be taken into account.

For the work done in this thesis, two beam dynamics codes have been extensively used: Elegant and ASTRA. Both codes have different approaches and are suitable for diverse scenarios.

2.5.1. Elegant

Elegant [35] (ELEctron Generation ANd Tracking) is capable of doing 6-D tracking using matrices upto third order, canonical integration and numerical integration. This code could be employed for circular and linear accelerators and beamlines. It is a powerful code with minimum computational cost which supports all standard beamline elements, as well as RF elements, kickers, apertures, wakefields and many other accelerator components. The effects of 1D CSR is also included. Elegant has the option to do accelerator optimization based on Courant Snyder parameters but could also be done using tracking of full beam distribution. The latter ofcourse is computationally more expensive than the former approach. Longitudinal space charge forces can also be included. However, the code is limited to work with higher energies as transverse space charge forces are not taken into account. Is is therefor not suitable for tracking beams in RF guns and photoinjectors. The code may also be used for intermediate energy range, i-e few hundreds of MeV's and to study the significance of space charge effects in combination with other particle tracking codes that takes SC into account.

2.5.2. ASTRA

ASTRA [37] (A Space Charge TRacking Algorithm) is a tracking code and can be used on various platforms. ASTRA has built-in external fields for standard beamline elements and also allows users to track particles by importing external field maps. The built-in fields can be scaled according to user defined input parameters. Tracking is based on non-adaptive Runge-Kutta integration of fourth order. As the name indicates, the SC forces are included in ASTRA. Users can choose to calculate SC forces by either using a cylindrically symmetric or a full 3D grid. This implies the use of cubic spline or a linear interpolation respectively. 3-D space charge calculation has a larger number of grid cells and hence require a large number of macro particles, which can lead to increased computation time.

Throughout the thesis, ASTRA was majorly used as the simulation tool in chapters 4 and 6. Elegant was used in chapter 6 for optimization purposes in combination with more detailed ASTRA simulations. Also at certain points in chapter 6, optimization routine from linacOpt [38] was used. In this routine, the optimization algorithm, such as the particle swarm or genetic optimizer is used to find the local and global minima of given objective functions. The linacOpt was applied to find the minimum beta function at the focal point i-e the entrance of the plasma cell. However, this optimization procedure was limited to a single objective function. In our case, there were several specific constraints leading to extremely long

optimization time and making it impossible to optimize several objective functions. Hence more rigorous elegant optimization with detailed ASTRA simulations were employed.

3

The ARES Linac at SINBAD

3.1. Introduction

The ARES linac in the SINBAD facility at DESY is introduced in this chapter. Components of ARES and commissioning stages are described.

3.2. The SINBAD facility

SINBAD is an accelerator R&D facility currently under construction in the former DORIS tunnel at DESY, Hamburg site [14]. SINBAD is dedicated for research in the field of production of ultrashort electron bunches and will host multiple independent experiments as test bench for laser driven advanced high gradient acceleration techniques such as Dielectric Laser Acceleration (DLA) [15], Laser Wake field Acceleration (LWFA) [16] and THz-driven acceleration in the AXSIS project [17]. The setup is quite comprehensive comprising of laser laboratories and planned accelerators. The first step in this project will be the installation and commissioning of ARES [19, 20]. Overview of the SINBAD facility is shown in figure 3.1.

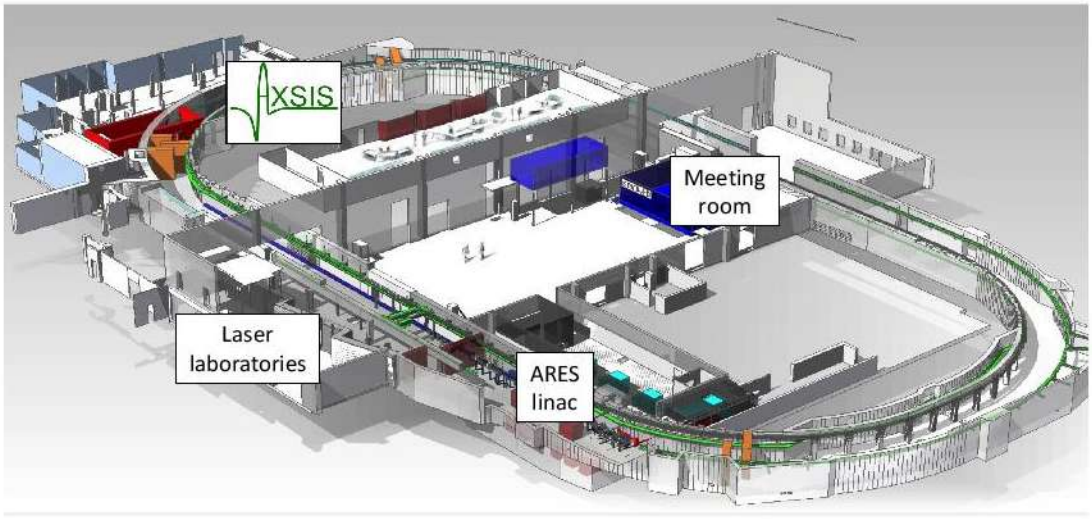

Figure 3.1.: Overview of the SINBAD facility at DESY. The two accelerators namely, ARES and AXSIS lies in different section of the tunnel along with laser laboratories and auxilary infrastructure. Picture taken from [14].

3.3. The ARES Linac

ARES has a targeted maximum energy of 230 MeV utilizing S-band acceleration technology. It comprises of an S-band RF Gun along with S-band Travelling Wave Structures (TWS), which are designed for a maximum energy capacity of 230 MeV. However, for bunch compression such an amount of energy is not normally required, therefore the estimated final energy at the normal operation is around 150 MeV. The bunches will be compressed to femtosecond-scale lengths to compliant them for use in the novel acceleration experimental concepts. These TWS will be proceeded by a matching section followed by a chicane, through which the beam is initially matched and then compressed. Conversely, the compression could also be achieved via velocity bunching in the TWS [39, 40]. ARES is designed to provide ultra-short (FWHM, length sub fs-few fs) high brightness electron beams for injection into novel accelerators. This approach has several advantages. The ARES linac on one hand will allow the R&D on the production of high brightness ultrashort electron bunches. On the other hand short bunches fit into compact novel accelerators, with short accelerating field wavelengths. Hence, such bunches constitute excellent probes to measure the energy gain and the quality of the acceleration. The characterization of such short bunches is a research field in itself and ARES will also serve as test bench for novel diagnostic devices in the low to medium charge upto 30 pC, sub-fs to few fs bunch length range [41, 42].

3.3.1. Commissioning stages of ARES

ARES will be commissioned in stages. The conceptual layout of the stages is shown in figure 3.4. The baseline layout, shown on top of figure 3.4, is constituted by an S-band photo-injector composed by an RF-gun and two accelerating structures. The electron bunch is produced via photo-emission and

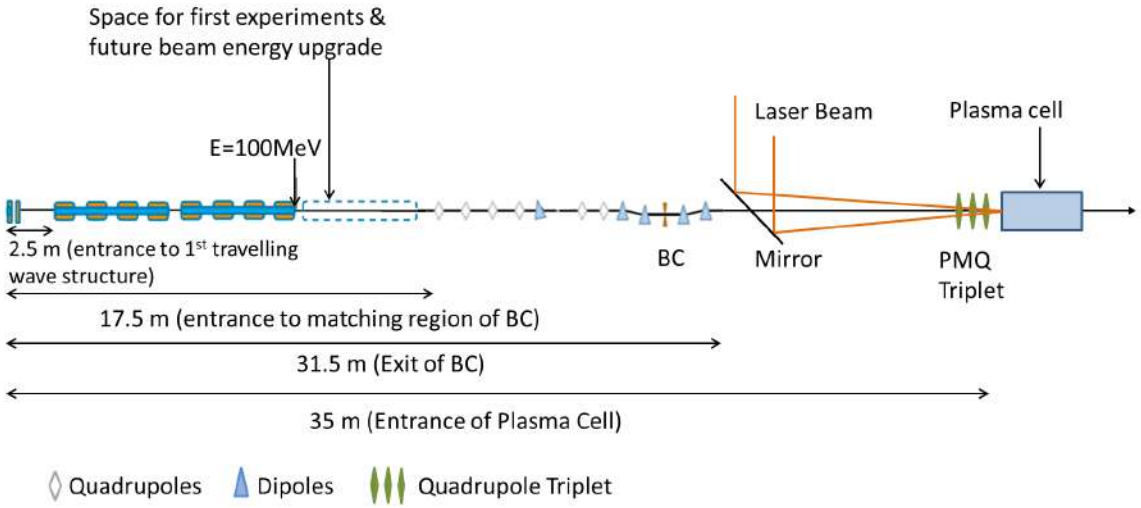

Figure 3.2.: Schematic of the ARES beamline including BC and the experimental area (not to scale).

then accelerated and compressed simultaneously in a linac surrounded by solenoids using the well-known velocity bunching technique [39]. The first experimental area (EA1) and the diagnostic beam line will be located at the end of the linac.

A substantial upgrade of the accelerator has been foreseen within the ATHENAe Project [8] depicted in the middle and bottom pictures in figure 3.4. The upgrade will allow the installation of a third accelerating cavity for energy upgrade of the linac, a bunch compressor including a collimator between the second and third dipole and a high energy diagnostic beamline including the novel PolariX TDS [43]. Finally, the second experimental area (EA2) could possibly host Laser WakeField plasma Acceleration (LWFA) experiments combining the electron bunch from ARES and the high power laser KALDERA [44].

The beam parameters corresponding to the baseline and upgraded version of ARES are summarized in Table 3.1. Presently, the linac and matching section has been installed and commissioned with installation of BC in progress as shown in the top and middle layout in figure 3.4. The sequent sections, shown in the bottom pictures of figure 3.4, will be installed in the next years. The panaromic view of the ARES linac is shown in figure 3.4.

Table 3.1.: Beam parameters from ARES.

Parameter	ARES baseline	ARES upgrade
RF Frequency (GHz)	2.998	2.998
Rep rate (Hz)	10-50	10-50
Beam Energy (MeV)	100 (155 on crest)	150 (230 on crest)
Bunch Charge (pC)	0.5-30	0.5-30
Bunch Length (fs)	sub to few fs	sub to few fs
Minimum Arrival Time Jitter (fs)	few tens	10

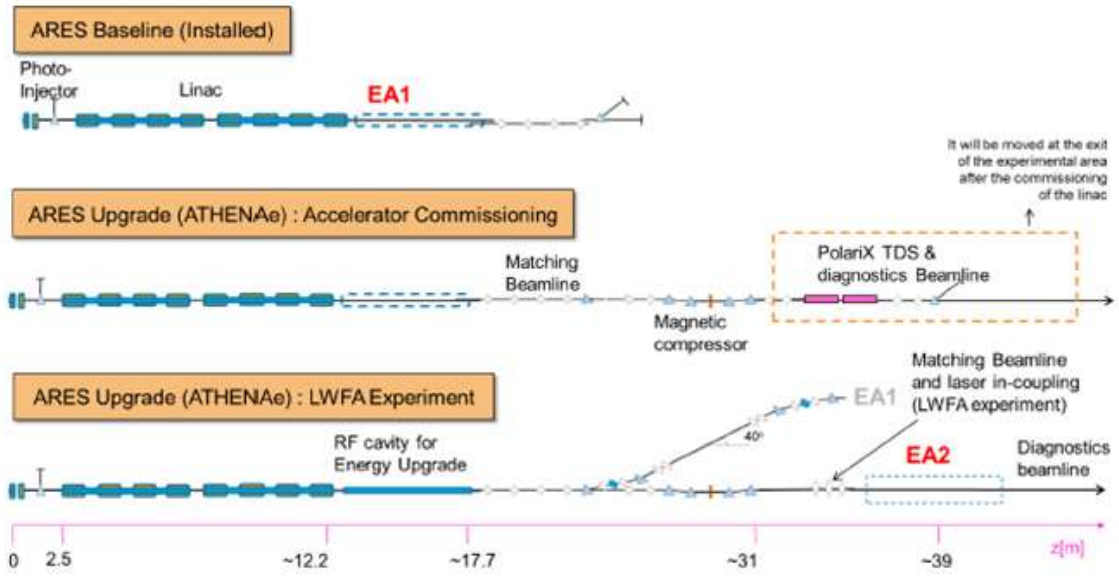

Figure 3.3.: Evolution of ARES layout in different stages.

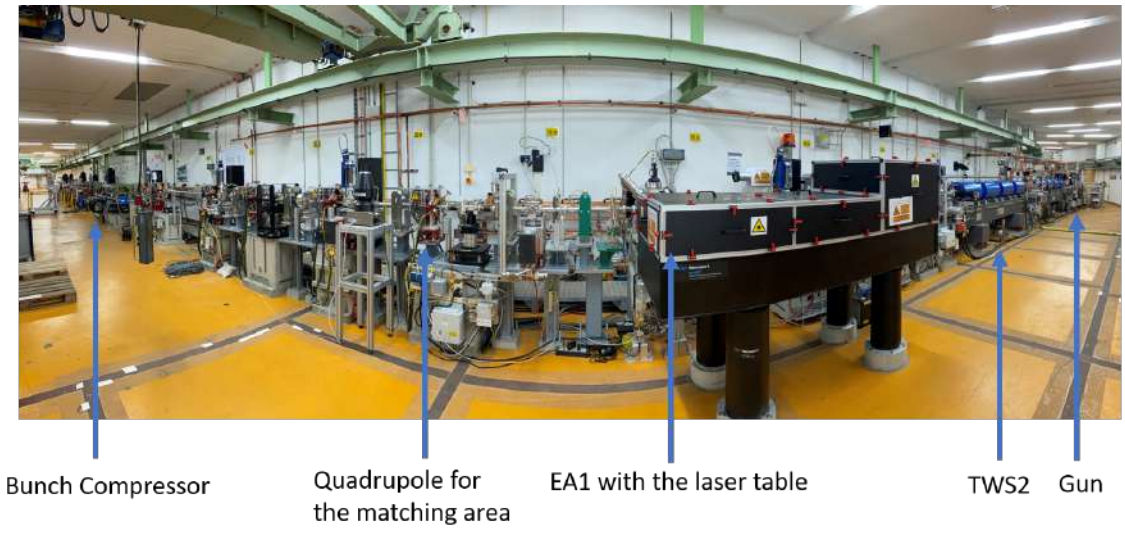

Figure 3.4.: Picture of ARES linac taken in July 2021. Actual linac and the beamline is straight. The panorama view taken to show the full completed beamline of ARES. The RF gun, two travelling wave structures (TWS), the first experimental area (EA1) for DLA experiments followed by matching quadrupoles and the Bunch compressor is visible in the picture. Picture courtesy F. Mayet.

3.3.2. Photoinjector

It is the first component of the accelerator designed to generate an electron beam by shining UV laser light on a metallic cathode. The electron beam is then accelerated and focused using 5 MeV RF gun and a solenoid. The resultant beam is characterized and injected in the TWS of the linac. The schematic of the gun is shown in figure 3.5 and the picture of installed gun in the tunnel is shown in figure 3.6.

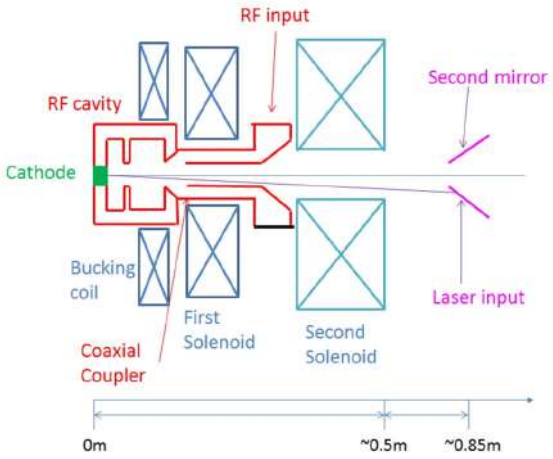

Figure 3.5.: Schematic of RF gun of ARES. This schematic is not to scale.

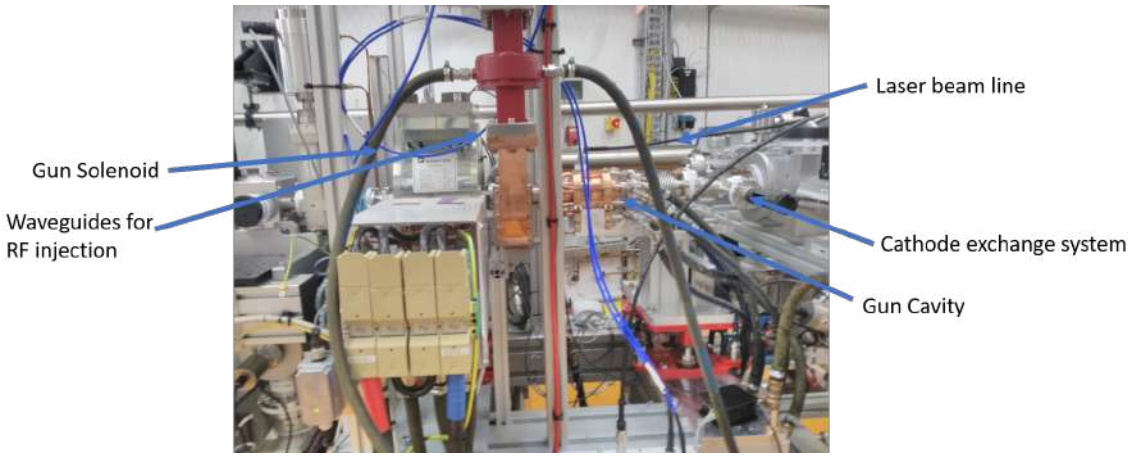

Figure 3.6.: View of Gun installed in the linac.

The RF gun comprises of a photocathode and an invacuum cathode exchange system together with RF resonators. The cathodes may be metallic or semi conductors. The metallic cathodes can be of Copper or Molybdenum. The metallic cathodes, owing to its extremely short emission time, limits the size of the bunches to < 1 ps. The charge emission for a given laser power is low due to low Quantum Efficiency (QE). On the other hand, semiconductor cathodes like Cs_2Te have a comparatively high QE. However, they have longer emission time which makes them suitable for production of tens of pC or higher charged bunches of longer lengths.

3.3.2.1. Gun cavity

The gun comprises of a 1.5-cell cavity operating at 2.998 GHz. It is REGAE gun design with longer antenna connecting the RF coupler [45]. A focusing solenoid named "Second Solenoid" located at 40.6 cm from the cathode as shown in figure 3.5 is used for transverse focusing of electron bunches. The solenoid named "First Solenoid" in figure 3.5 and its bucking coil will be installed in near future to allow an improvement of the quality of electron beam.

3.3.2.2. Photocathode laser

A commercially available system, PHAROS-SP-200 model, is used as photocathode laser at ARES. It is a 1 mJ Yb-doped laser with a fundamental wavelength of 1030 nm. The photoelectric emission, with metallic and semiconductor cathodes, will be obtained using the integrated fourth harmonic at 257nm. This curtails the non linearity of the longitudinal phase space and the beam transverse emittance [16]. The laser is coupled to the beamline from downstream the gun cavity and shines at the photocathode with a small incidence angle from the cathode normal plane. In order to allow for the direct visualization of the laser spot on the cathode, a second mirror is placed at the same longitudinal position as the incoupling mirror. This allows to directly visualize the laser spot size on the cathode. The pulse length of the laser is tunable between 80 fs to 4.2 ps rms. The transverse-spot-size diameter on the cathode can be trimmed down to 54 μm.

3.3.3. Gun diagnostic area

Beam diagnostic components are the sensory organs of any accelerator facility. They are of critical importance to measure the properties of particle beams. Various diagnostic elements have been installed in the beamline to measure charge, beam transverse position and profile, momentum and momentum spread, transverse emittance and arrival time. Between the gun and the first travelling wave structure (TWS1), ~ 2 m of space has been dedicated for various diagnostic devices to fully characterize the beam. A schematic view of the gun diagnostic area is shown in figure 3.7 and the installed components can be viewed in figure 3.8. The beamline elements in the gun diagnostic area along with their purpose are discussed in detail in the following sections.

3.3.3.1. Charge measurement

A Faraday cup is the most simple and widely used device for the charge measurement. It is a metallic cavity designed in the form of a cup to effectively capture and contain the electron beam. This device can be used to measure a wide range of bunch charges. However it has to be moved in the beam line for the measurement and hence is a destructive device. At ARES, two Farday cups are installed in the lower energy gun diagnostic area. One can be moved along the main section and the other along the dipole spectrometer bending arm. An alternating non-destructive cavity based charge measurement device,

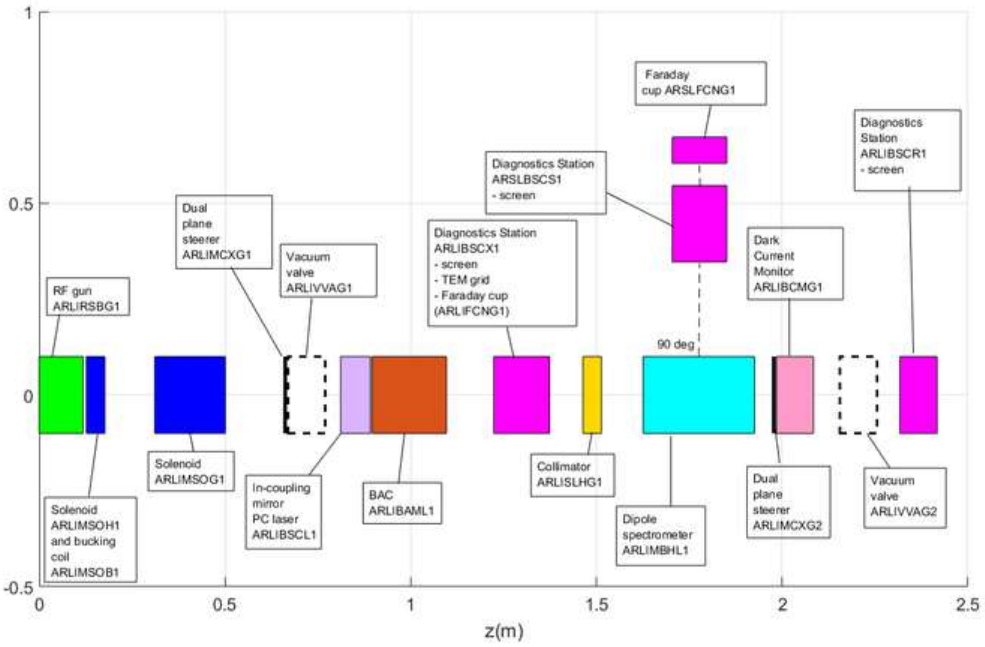

Figure 3.7.: Schematic of diagnostic section after the RF gun. Courtesy of B. Marchetti.

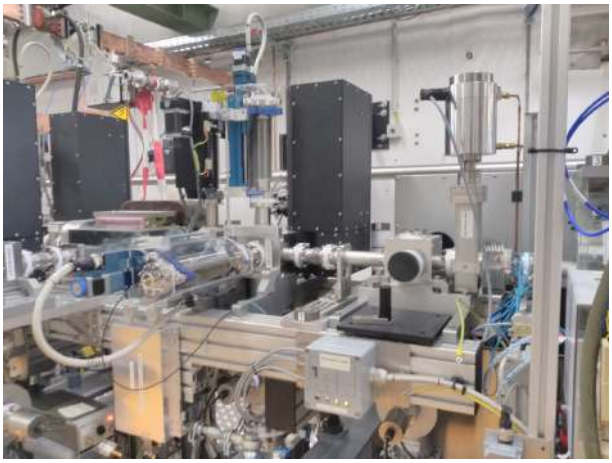

Figure 3.8.: View of diagnostic section after the RF gun in the beamline.

called "DaMon", is also available at ARES [46]. The DaMon, a dark current monitor, is installed just after the dipole spectrometer in the main beamline as shown in figure 3.7.

3.3.3.2. Beam profiling via screens

Scintillation screen stations are used at ARES to image the electron beam profile. Scintillation is the process of emission of light by a material when struck by a charged particle. This excites valence electrons of the molecules in the material that inturn emit radiations as light in the visible spectrum. The light goes out of the beam pipe through a window and is imaged onto a camera. Screens made of Cerium doped Gadolinium Aluminium Gallium Garnet crystals (GaG:Ce) are used at ARES. The emission peak of this crystal in is the range of 520-530 nm and a light yield of 46000 photons/MeV [47]. These properties made such crystals favorable over other scintillator materials.

The design of the ARES screen stations is similar to stations used at European XFEL. However, at European XFEL, LYSC:Ce crystals are used as screen material rather that GaG:Ce. The screens are inserted perpendicular to the beam axis. The resolution of screen and imaging system combined is 10 μm. The size of the screen is 30.5 mm by 24 mm. The field of view is typically much smaller than these dimensions. For the screens at the gun diagnostic area, the field of view is approximately 8.5 mm in horizontal and 5 mm in vertical. This varies within few 100 μm, depending on the pixel to size calibration, for each screen. The beam profiling via scintillation screen is a destructive measurement, as the screens has to be moved in the beamline using movers.

3.3.3.3. Beam-position monitors

In contrast to screen stations, beam-position monitors commonly known as BPMs are non destructive measurement devices. However, they can only provide a measurement of the relative bunch charge and the mean beam position. Two standard types of BPMs used are broadband pickups and resonant cavity monitors [31]. In the broadband pickups type BPM, the charged beam induces signal in each of the four electrodes placed symmetrically around the beam pipe. The strength of the each signal then allows the beam position to be determined. On the other hand, resonant cavity monitors are based on the excitation of a dipole mode in a cylindrical cavity by an off axis beam. Cavity BPMs will be installed at ARES because of a higher spatial resolution. The BPM was designed with the goal of achieving a single-shot precision of 25 μm and an average precision of 5 μm over 50 points for a bunch with 0.5 pC charge.

3.3.3.4. Emittance measurement

Numerous standard techniques are employed to measure the emittance of electron beam. The so called "pepper pot" or a metal grid in combination with a screen can be used to measure emittance at low energies. Alternatively, the technique called Quad-scan can be applied to measure emittance by measuring the beam size on a screen as a function of solenoid or quadrupole strength.

At the gun diagnostic area, a scan can be performed using the gun solenoid to measure the emittance. Moreover, metal grids are also available for measuring the emittance of low charge beams [48].

3.3.3.5. Horizontal and vertical steerers

Two sets of dual-plane steerers are installed in the gun diagnostic section to correct the trajectory in both horizontal and vertical planes as shown in figure 3.7.

3.3.3.6. Energy measurement

Dipole magnets are usually installed in an accelerator facility for the energy measurement. Energy is determined by deflecting the beam with a known homogeneous dipole field and measuring the beam profile on a screen downstream. Since the beam position on the screen is a function of energy, therefore the energy distribution can be measured from the screen image.

A dipole magnet, installed downstream the gun with a maximum magnetic field of 0.155 T and a bending angle of 90^0 at 5 MeV is used for energy measurement. The installed dipole along with the screen station is shown in figure 3.9.

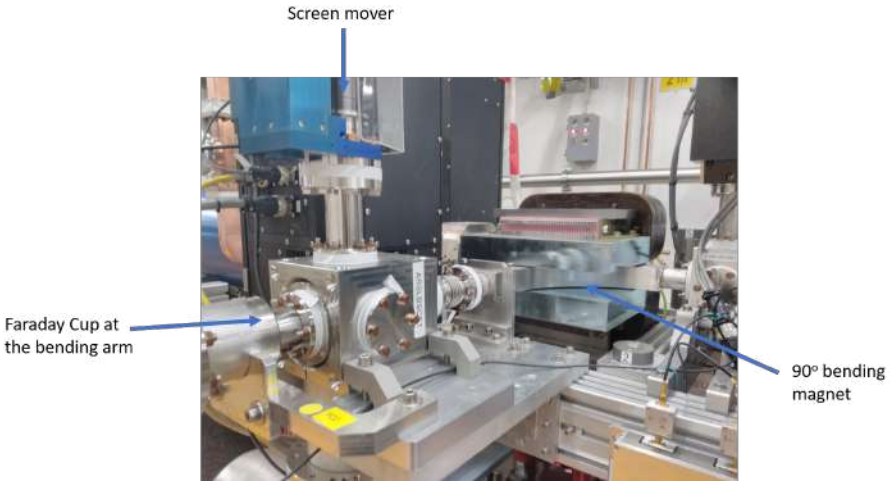

Figure 3.9.: Low energy dipole spectrometer view installed in the beam line along with ARES screen station and Faraday cup. The picture is taken from the bending arm side view.

3.3.4. Travelling wave structures

Two travelling wave structures are installed downstream the gun diagnostic area, with a third due to be installed in 2022 for a possible energy upgrade of ARES. Each TWS is 4.2 m long operating at 2.998 GHz. Each TWS is powered individually by 45 MW RF station, with 4.5 μs long pulses. Each structure comprises of 120 regular cells and two coupling cells, with phase advance of $2\pi/3$ per cell. The maximum energy gain for on-crest injection per cavity is 75 MeV, and for off-crest acceleration will be limited to 50 MeV, which also allows the compression of bunches. The installed TWS can be viewed in figure 3.10. Each TWS is surrounded by four solenoids to compensate the defocusing effects in the beam. Each

solenoids can be individually powered and alignment can also be adjusted individually. The peak design fields for these solenoids is 0.1 T. The solenoids around the accelerating cavities are visible in blue casing in figure 3.10.

Figure 3.10.: Travelling wave structure after the gun. Solenoids around TWS are enclosed in blue casing.

3.3.5. Diagnostics for linac and matching area

Many diagnostic elements are installed along the beam line at ARES to fully characterize the beam, both during commissioning and while in operation. An overview of the linac with beamline elements is shown in figure 3.11.

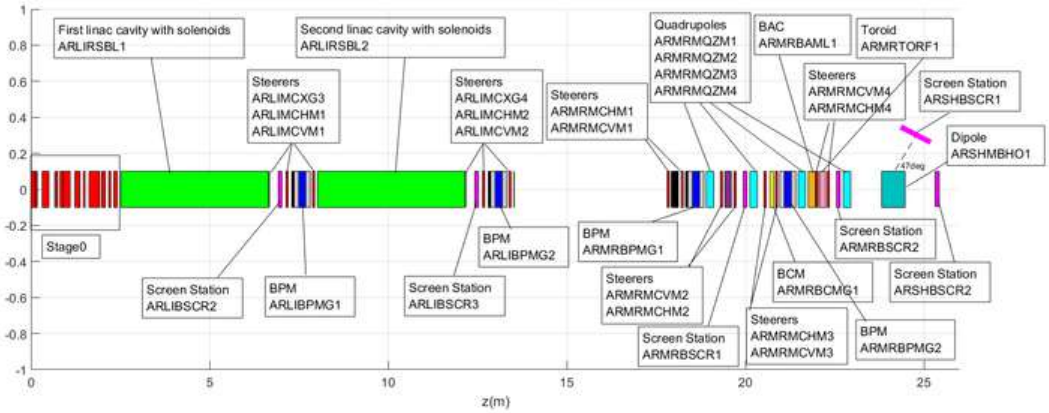

Figure 3.11.: Schematic of beam line after the travelling wave structures showing various diagnostic elements. Courtesy of B. Marchetti.

Figure 3.12.: Quadrupoles installed downstream the TWS for focusing and matching into the experimental area.

3.4. Magnetic bunch compressor

The travelling wave structures are followed by a matching area comprising of six quadrupoles. Downstream these quadrupoles, a magnetic bunch compressor(BC) consisting of four dipoles and a slit will be installed. The schematic of the BC is shown in figure 3.13. The BC can compress the bunches to sub-fs bunch duration by imprinting an energy chirp with off crest acceleration in the TWSs. As the path through the dipole magnets of the chicane is energy dependent, a chirp is imprinted in the TWS such that the path of the head of the bunch is lengthened compared to its tail, hence compressing the bunch to achieve sub fs scale bunches. The longitudinal collimation of the bunch can be obtained through introduction of slit between second and the third dipoles. This reduces not only the bunch length but also the energy spread thereby decreasing the jitter in both of these quantities as well [49].

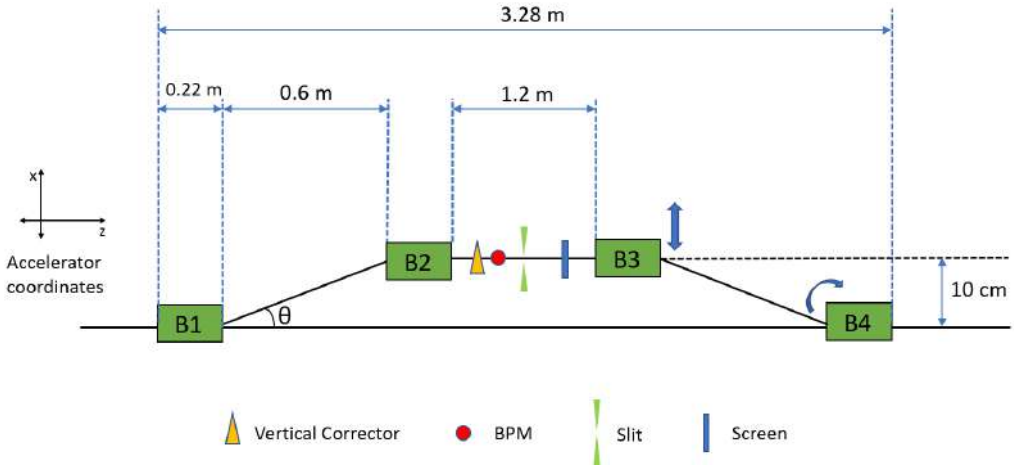

Figure 3.13.: Schematic of magnetic chicane, showing slit, BPM and screen for beam positioning and profiling. The schematic is not to scale.

3.5. Experimental areas at ARES

ARES is designed to have two experimental areas namely experimental area 1 (EA1) and experimental area 2 (EA2) as shown in figure 3.2. The EA1 is dedicated to experiments for dielectric laser acceleration and charged particle beam diagnostics. This is followed by a matching section into the BC. At the exit of the BC the electron bunches can have a duration of a few fs or below [49]. The BC is followed by a drift space that provides space for the high power laser incoupling. Further downstream, a high energy diagnostic beamline followed by the matching optics for the EA2 is foreseen. This area could host LWFA experiments and could combine the electron beam from ARES with pulses from the high repetition high power laser KALDERA currently under construction at DESY [44]. The second experimental area will also host the novel transverse deflecting structure called PolariX-TDS with variable polarization produced in collaboration with DESY, PSI and CERN [41]. It operates at X-band frequencies of around 12 GHz, providing a higher longitudinal resolution than commonly used lower frequency S-band structures.

Access to SINBAD facility at DESY to external researchers is also possible not only in the context of collaborations but also via the ARIES transnational access program [50]. This EU funded integrating activity project aims to open research facilities and integrated infrastructures to external users. Therefore, a fraction of beam time of ARES and hence the two experimental areas will also be made available to external users to conduct experiments.

3.6. Novel acceleration concepts

ARES is dedicated for research in the field of production of ultrashort electron bunches and will host multiple independent experiments as test bench for laser driven advanced high gradient acceleration techniques such as Dielectric Laser Acceleration (DLA) and Laser Wake field Acceleration (LWFA). The structures used in novel accelerators, like plasma cells and microstructured dielectric materials have very small accelerating periods and hence require ultrashort bunches. Short bunches fits into small accelerating wavelengths and act as excellent probes to measure the energy gain and the quality of the acceleration. In this section, the high gradient acceleration concepts planned at ARES are briefly introduced.

3.6.1. Dielectric laser acceleration

In DLA, an electron beam is injected inside a hollow dielectric grating structure. The dielectric structures are illuminated with a laser beam. The near fields of these structures can be used to accelerate particles. This concept benefits from high damage threshold of dielectric materials in the near infra-red to optical regimes to take advantage of high fields achievable by the laser sources. The achievable gradients are of the order of single digit GV/m. The international ACHIP collaboration program [51], funded by the Gordon and Betty Moore Foundation, aims to demonstrate a prototype compact dielectric electron accelerator. Maximum peak gradient of 1.8 GV/m has been experimentally demonstrated at UCLA [52].

Within the ACHIP collaboration, DLA experiments have been designed at ARES with EA1 dedicated to this purpose [15]. The stage I experiment at ARES aims to show net acceleration of electrons in a grating-type dielectric structure with as short as possible single bunches. As stage II, experiments on phase space manipulation using dielectric gratings to achieve stable acceleration of a micro-bunch train are also planned.

3.6.2. Laser wake-field acceleration

LWFA can provide an accelerating gradient in the range of ∼100 GV/m, which is several orders of magnitude higher than what can be achieved with conventional RF technology. This reduces the size of the acceleration channel from meters to millimeters and hence offers the possibility of compact and cost-effective accelerators. In LWFA, strong laser pulses propagating in a plasma generate charge separation through the excitation of wakefields, inducing strong electric fields. Since the LWFA concept was first introduced [6], it has been a subject of extensive studies with significant progress in recent years [9, 10, 53]. However, despite the demonstration of important milestones such as achieving GeV energies in only cm-scales, these devices typically suffer from lower beam stability than available from established RF accelerators. The external injection LWFA experiment studied for ARES investigated a possible step towards usable LWFA from a combination of reproducible conventional RF-based accelerator technology with the high gradient fields from plasma wakefields [13]. The RF-based technology allows for a precise manipulation of the phase space of the electron bunches before entering the plasma, hence providing independent control and quality adjustment as well as optimization of the plasma experiment [16]. The beam quality in novel accelerators depends on the detailed parameters and quality of the injected beam e.g. bunch shape, bunch length, emittance, arrival time stability and beam energy. ARES provides the option of widely tunable working points (WP) and bunch shapes for external injection LWFA accelerator R&D.

Simulation studies have been performed to study the LWFA at ARES [54, 55, 56]. The goal of the simulation studies is to accelerate electrons to 1 GeV with relative energy spread at few percent levels. The simulation studies are done using plasma densities of 10^{16} cm^{-3} to 10^{18} cm^{-3}, corresponding to an accelerating period of 1 ps to 0.1 ps. Within this period, only a fraction of phase range will have both transverse focusing fields and longitudinally accelerating forces which are necessary for acceleration in a plasma cell. In addition, a longer bunch will result in greater induced energy spread because of the gradient in the accelerating field. Hence, ultrashort bunches with minimum arrival-time stability are desirable for injection into the plasma to limit energy spread and jitter. To create the plasma and wake fields to accelerate electrons, the electron bunches could be combined with high power laser KALDERA (kilowatt lasers at DESY for revolutionary accelerators) [44]. It is a Ti-Sapphire based laser which is under development at DESY. In the first stage, the laser will have a pulse length of approximately 30 fs FWHM, peak power of 100 TW, 3 J energy and repetition rate of 1 Hz. At the second stage, the

repetition rate will be increased to kHz range. The drive laser will be collinearly coupled to the main beamline. Simulation studies for the beam line and design of the final focus system to efficiently match the electron beam to the plasma cell forms an important part of this work and is discussed in detail in chapter 6.

4

Development of a Beam Based Alignment Algorithm

4.1. Introduction

An algorithm developed for the beam-based alignment of the solenoids of the ARES linac is discussed in this chapter. The procedure is described and the developed algorithm is validated against numerical simulations using particle tracking code ASTRA. Possible sources of errors and their impact on determining the misalignment in the solenoids are discussed. The developed procedure was implemented in a MATLAB script with a user interface. At ARES, a focusing solenoid is installed at the RF gun. Also, there are four focusing solenoids around each travelling wave structure. The developed script will be routinely used for the alignment of all afore-mentioned solenoids during the commissioning of ARES. The results from this chapter of the thesis have been published in [57, 58, 59].

One of the key points of high brightness beams is low emittance. Generating low emittance from a photoinjector and preserving it during beam transport in accelerating cavities is greatly affected by the alignment of the beamline elements due to deflection forces by the accelerating electric fields . Moreover, an off-axis beam in a magnetic focusing field experiences an additional kick and can dilute the emittance [60, 61]. Solenoids are an effective device for focusing electron beam at low energies. They focus the beam in both transverse planes simultaneously. The misaligned solenoid introduces a kick in the beam with the resultant beam travelling off-axis. To preserve the low emittance of the beam during the beam transport from the gun till the experimental area, it is extremely important to have good alignment of the beam trajectory with the axis of the focusing solenoid. Off axis particles travelling in a solenoidal field have quadratic dependence which makes it difficult to determine the solenoid axis as opposed to in a quadrupole. Also offset of the angle of the incoming beam with respect to the magnetic axis of the solenoid provoke a kick in the beam trajectory. Therefore, beam-based alignment of focusing solenoids is an important part of commissioning.

Many procedures have been developed to align the beam trajectory through the solenoid axis to preserve

emittance. As described in [62], dedicated programs have been developed to fit the measured results to determine the beam orbit. Numerical simulations in an iterative process are used for fitting the measured data by measuring beam position as a function of solenoid current. This procedure has been applied at PITZ and photoinjector of VUV-FEL at DESY. On a few occasions, transfer matrices have been used for alignment of beam trajectory. For example in [63], the transfer matrices are calculated by a special script [64] to fit the measured results for determining the beam orbit. However, the procedure for determining the parameters of the beam orbit in [63] is not described. In [65] the kick from the solenoid is minimized by measuring the beam position as a function of solenoid current and adjusting the gun position in an iterative process. Recently, the use of transfer matrices for the correction of beam trajectory through a solenoid has been reported [66]. In this chapter, the use of linear transfer matrices to determine the beam position and angles with respect to the solenoid axis is described. An equal and opposite misalignment of the solenoid w.r.t the beam axis is corrected to obtain an on-axis beam trajectory for ARES. A Matlab script with a user interface was developed to determine the misalignment. The developed method is validated against detailed numerical simulations using ASTRA, an aspect which is mostly missing in the above mentioned references. The algorithm used is simple, efficient, gives reliable and reproducible results within the accuracy of the micromover system for use at ARES.

4.2. Solenoid focusing at the RF Gun

The 5 MeV RF gun of ARES was introduced in section 3.3.2 and the schematic of the gun is shown in figure 3.5. A focusing solenoid named "Second Solenoid" in figure 3.5 located at 40.6 cm from the cathode is used for transverse focusing of electron bunches. The effect of misalignment of this solenoid on beam parameters, emittance and beam sizes have already been studied [10]. The solenoid named "First Solenoid" in figure 3.5 and its bucking coil will be installed later on in 2021 to allow an improvement of the quality of the electron beam. This section describes the design aspects and measured magnetic field of the gun solenoid namely the "Second Solenoid" in figure 3.5 . The installed solenoid at ARES is shown in figure 4.1.

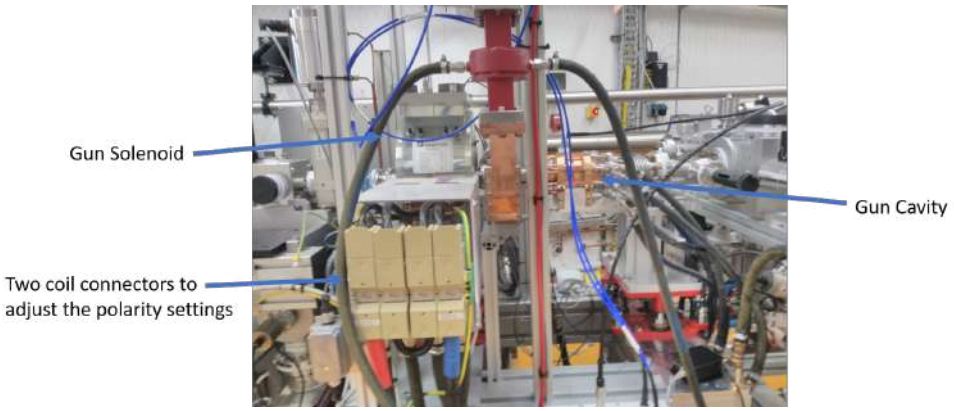

Figure 4.1.: Picture of the gun solenoid installed at ARES. Also visible is the gun cavity.

4.2.1. Design of gun solenoid

The gun solenoid consists of two coils of equal length. Each coil can be adjusted to different polarities which allows for better control of the beam [10]. The solenoid is housed on a manual micro mover system which has resolution of 100 μm in transverse direction and angular accuracy of approximately 0.5 mrad. Misalignment error can be in both transverse and angular planes. The 3-D view of the magnet is shown in figure 4.2 and the picture of solenoid mover system is shown in figure 4.3.

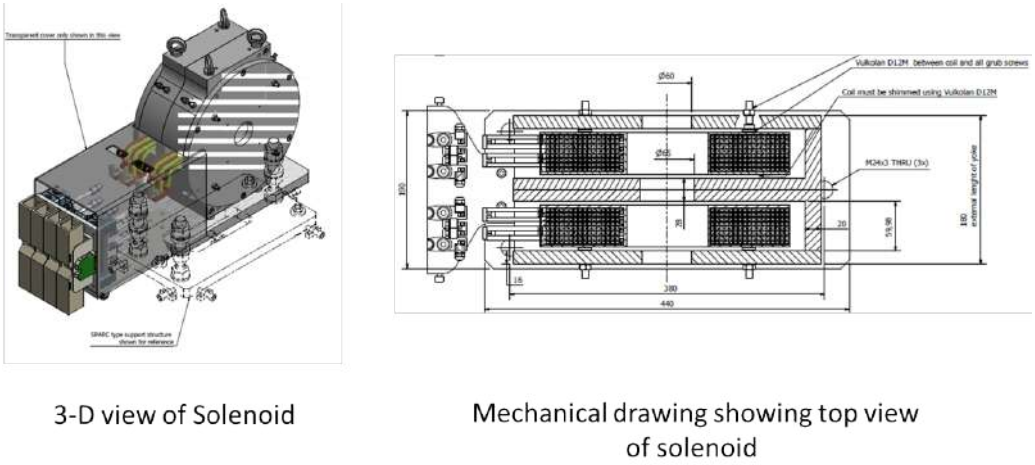

Figure 4.2.: Mechanical drawings of the gun solenoid. The right picture gives the 3-D view and the left picture shows the top view of the solenoid.

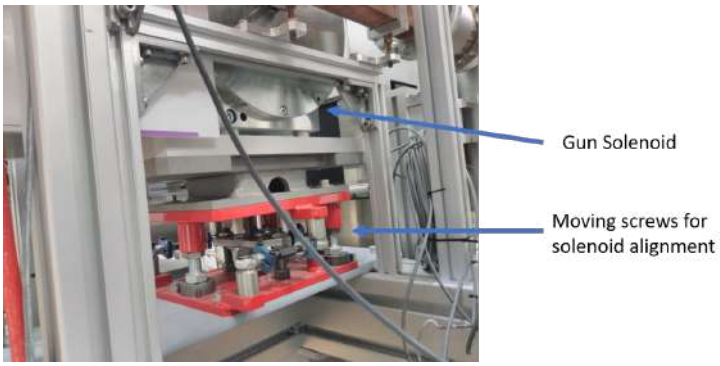

Figure 4.3.: Alignment screws for the gun solenoid

4.2.2. Magnetic measurement for gun solenoid

The gun solenoid magnet was manufactured and measured by the company Danfysik [67] and remeasured by magnet group at DESY using a Hall probe. Figure 4.4 shows the solenoid magnet mounted on the measurement stand.

The measured magnetic field profiles for the minus-plus (MP) and plus-plus (PP) polarity settings are shown in figure 4.6. These measurements were performed by the magnet group at DESY. The two coils have field profiles that overlap with each other, hence slightly decreasing the field at the center for

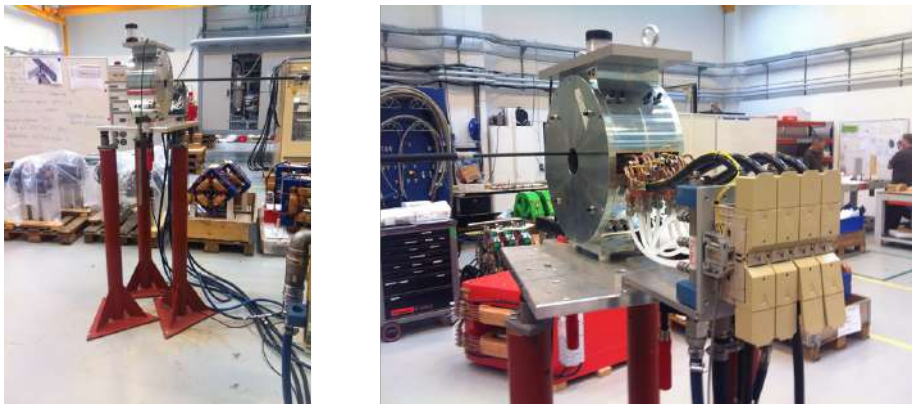

Figure 4.4.: Solenoid magnet at the manufacturing site while doing magnetic measurements. Picture courtesy Danfysik [67].

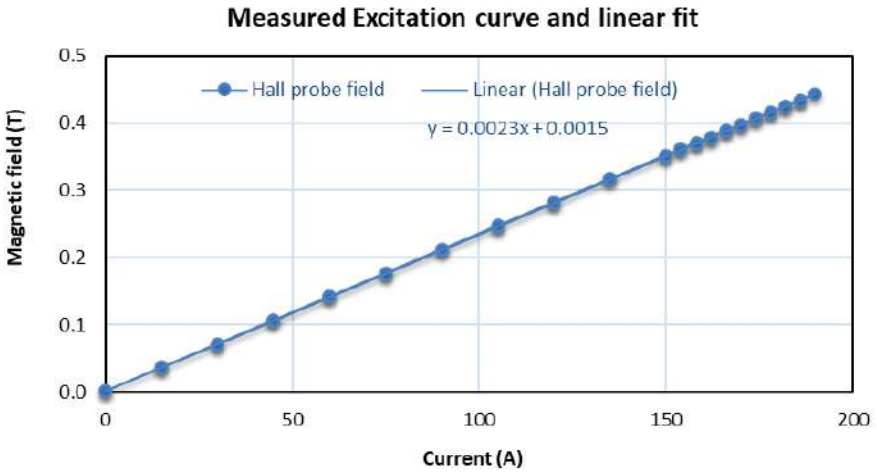

Figure 4.5.: Measured excitation curve of the gun solenoid compared with a linear fit. The magnetic field in Tesla is shown as the function of current in Amperes.

minus-plus polarity. However, operating the solenoid in minus-plus polarity has the advantage since any angular displacement introduced by first coil is compensated by the second coil because of equal and opposite polarity.

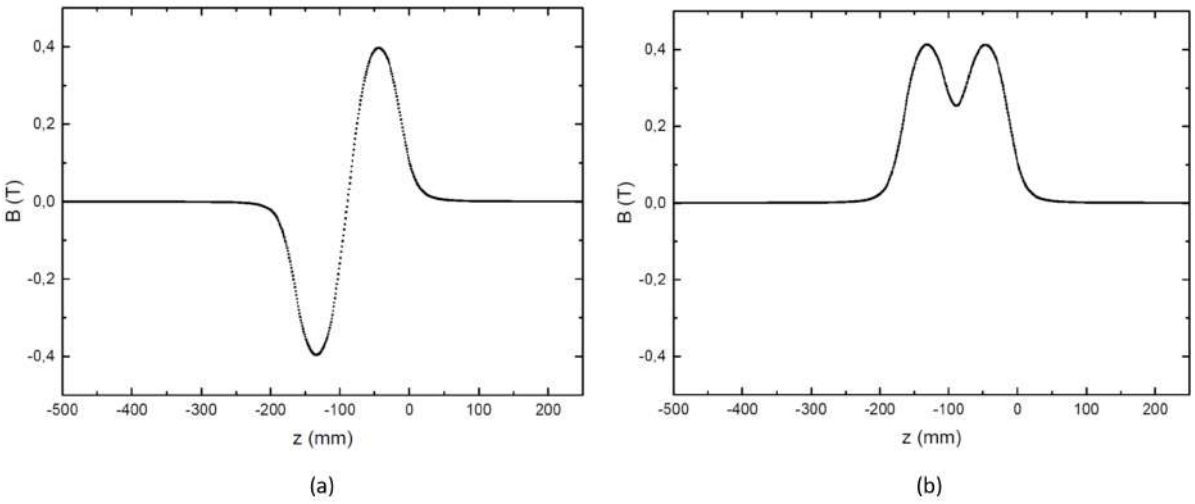

Figure 4.6.: Measured field profile of gun solenoid. The measurement was performed by DESY magnet group. The magnetic field in Tesla is shown along the longitudinal axis of the solenoid. The left figure gives the magnetic field profile for MP polarity settings and right figure gives the field profile for PP polarity settings.

4.2.3. Magnetic field to current calibration

Based on the measured excitation curve, the magnetic field to current calibration curve was derived and implemented in the so called magnet middle layer server for the calibration of magnetic field during ARES operation. In figure 4.7 both the excitation curve for the PP polarity and the single values for current and peak field on axis from the field maps of polarity PP and MP are plotted.

The values for PP polarity indicated by red circles in figure 4.7 lay perfectly on the excitation curve measured for the PP case. On the other hand, the blue circles corresponding to the minus-plus polarity are slightly off implying a lower peak field. This is expected because when the coils are used with opposite polarities, the tail of first coil and second coil overlaps and hence the resultant field is reduced in the center of the solenoid.

With this data, for the calibration of PP polarity of gun solenoid, which becomes minus-minus (MM) for negative currents, a straight line with slope 0.00233 T/A and intercept 0.00085 T was implemented. These values are taken from the measured data of the company as they sit perfectly on the excitation curve shown in figure 4.7. This calibration curve gives the peak value of the magnetic field, which is not in the center of the solenoid.

For plus-minus (PM) polarity, which becomes minus-plus (MP) for negative currents, straight line with slope 0.00225 T/A and intercept at 0 T is considered. These values are calculated by fitting the blue circles and imposing that the field is 0 T when no current is applied to the solenoid as shown in figure 4.8.

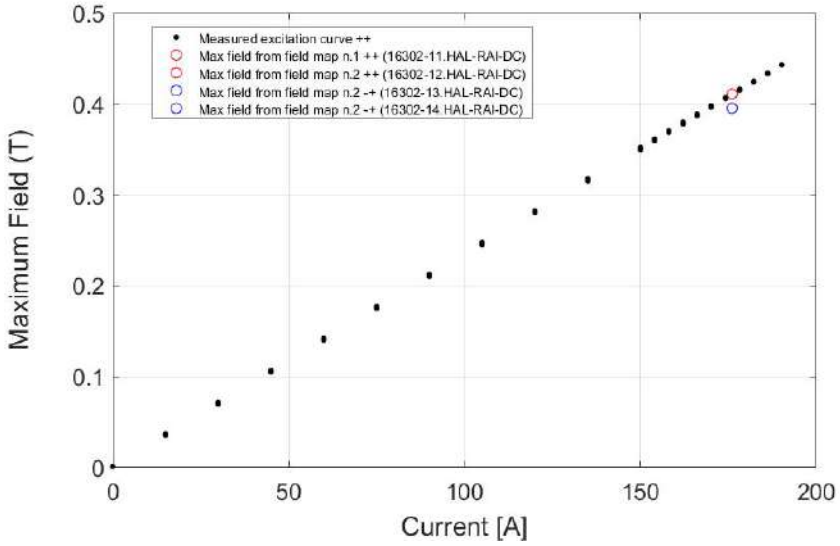

Figure 4.7.: Measured excitation curve of the gun solenoid compared with peak fields for PP and MP polarities. The magnetic field in Tesla is shown as the function of current in Amperes. Peak field is measured twice (indicated by n1 and n2 in labels) for each polarity settings to certify the reproducible measurement results.

This calibration curve also gives the peak value of the magnetic field which is again not in the center of the solenoid. The equation for magnetic field to excitation current calibration curve for the two polarities, PP and MP, are respectively given by equation 4.1.

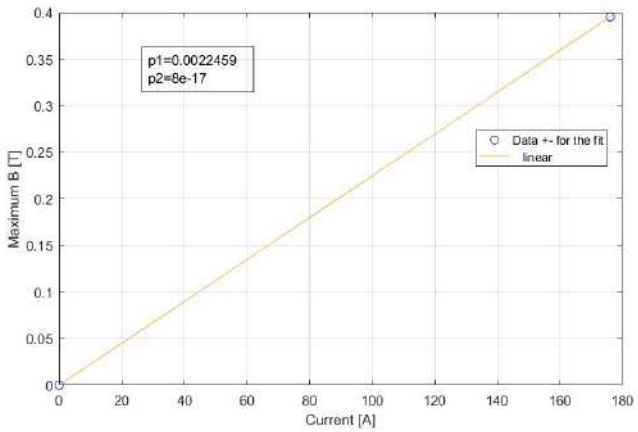

Figure 4.8.: Calibration curve for measured data points for minus-plus polarity settings. The measured data points are plotted with a linear fit to determine the equation for magnetic field in Tesla as a function of applied current in Amperes.

$$B_{PP}\ (T) = 0.00233\ \left(\frac{T}{A}\right) * I\ \ (A) + 0.00085\ \ (T)$$
$$B_{PM}\ (T) = 0.00225\ \left(\frac{T}{A}\right) * I\ \ (A) \tag{4.1}$$

4.3. Beam dynamics of a misaligned solenoid

The section is based on the [59] by the author.

A working point of ARES linac was simulated and optimized in ASTRA [37] to study the effects of misaligned solenoid on the beam dynamics. Evolution of beam parameters along the linac with velocity bunching is shown in figure 4.9.

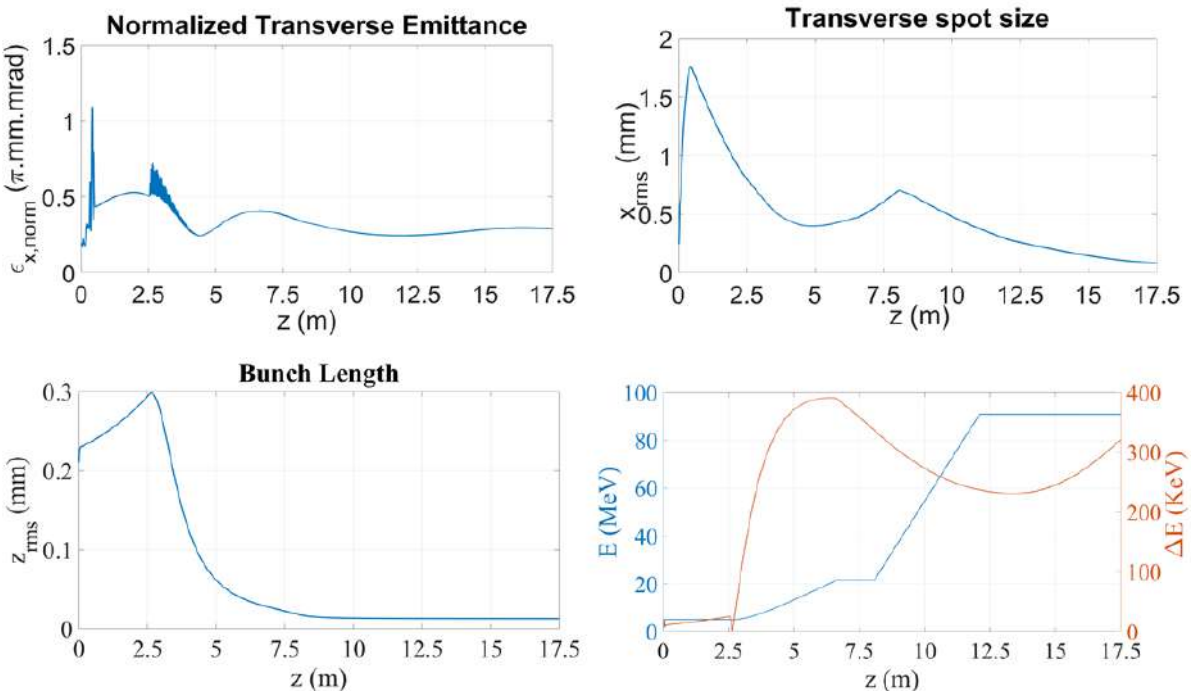

Figure 4.9.: Evolution of normalized transverse emittance $\epsilon_{x,norm}$, transverse spot size x_{rms}, bunch length z_{rms}, energy gain E and energy spread ΔE along the linac.

Using this WP, ASTRA was used to study the effect of solenoid misalignment on the beam size and emittance for a space charge dominated beam. In the ideal case, if the beam is perfectly aligned with the solenoid magnetic axis, it experiences only rotationally symmetric transverse focusing field. In reality, the beam experiences a kick due to misalignment and can experience emittance growth. Apart from the transverse offsets, we will also have parasitic tilts of the solenoid's angles in both x-z and y-z planes. An ASTRA scan was performed to account for the particle lost as a function of solenoid offset in x and y direction as well as rotational offsets in x-z and y-z plane. It was noticed that most of the particles were lost for a misalignment bigger than 1 mm. The expected achievable precision for the alignment of our solenoid is within 100 μm while the magnetic length of the solenoid is 0.19 m. So the angular precision of the position adjustment system of the solenoid is ~0.526 mrad. The coils in these simulations have opposite polarities and were assumed to be perfectly aligned with each other. Figure 4.10 and 4.11 give the beam position in x and y planes as a function of solenoid misalignment in the horizontal and vertical direction respectively. In all figures, for one value of offset in solenoid position, solid line is for beam property in x and dashed line is for y. Same colors for solid and dashed line correspond to equal offset

value. x_{avr} and y_{avr} stands for beam centroids.

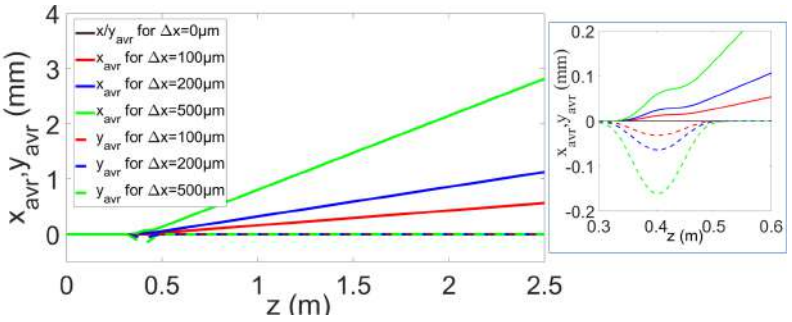

Figure 4.10.: Beam position for misalignment between solenoid and incoming beam in horizontal direction Δx. The colored curves indicates beam path along the longitudinal axis as a function of misalignment of the gun solenoid in the horizontal direction. Right image has change of scale to zoom in on beam positions. Solid line is for beam position in x and dashed line for beam position in y direction.

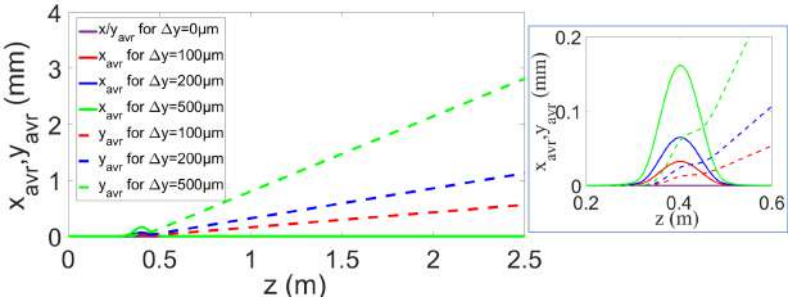

Figure 4.11.: Beam position for misalignment in the vertical direction Δy. Right image has change of scale to zoom in on beam positions. The colored curves indicates beam path along the longitudinal axis as a function of misalignment of the gun solenoid in the vertical direction.

Effect of angular tilts on beam position and emittance were also studied. Also in this case, tilt around $x - axis$ i.e. in the $y - z$ plane, nullifies the effect in case of opposite polarities in x-direction. This cancellation effects only happens in one direction i.e. transverse to direction of misalignment as expected. The effect of different coil polarities on beam position is shown in figure 4.12. Figure 4.13 and 4.14 shows beam sizes. All angular misalignment introduced in the solenoid are in radians. The smallest one corresponds to tolerance of 100 μm which is the accuracy of mover system.

Figure 4.15 and 4.16 gives the difference in emittance for offset in solenoid position with respect to a perfectly aligned solenoid. Emittance for bunch charge of 25 pC at the entrance of travelling wave structure i-e at 2.5 m is 1.2 π.mm.mrad. Maximum Emittance growth calculated for 500 μm in just one transverse direction is around 7% of the original value. It is noticed that just at the entrance of travelling wave structure, there is significance emittance growth which will eventually have much more stronger impact along the beam line and the experimental area (at 17.5 m and beyond). Figure 4.17 gives the emittance growth as a function of misalignment in x-z plane. The two peaks correspond to two coils of the solenoid.

Since the tilts are associated with the offsets in transverse direction, figure 11 gives the emittance

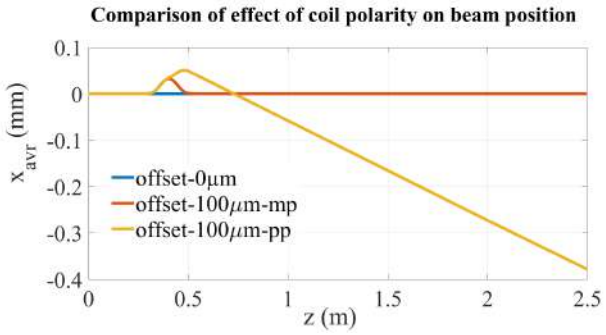

Figure 4.12.: Beam position for PP and MP coil polarities for misalignment in vertical direction.

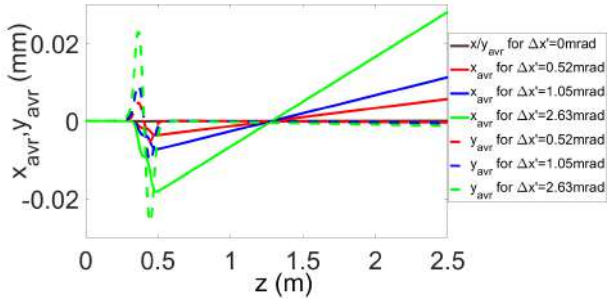

Figure 4.13.: Effect of angular offsets in the x-z plane between the solenoid and the beam in the beam trajectory in the gun region. The different colored curved shows varying degree of angular misalignment.

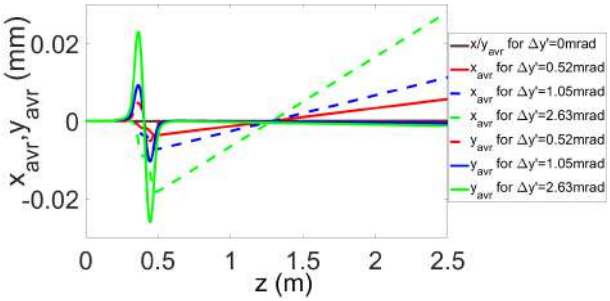

Figure 4.14.: The plot of beam trajectory along the longitudinal axis as a function of angular misalignment of the gun solenoid in the y-z direction. The different colored curved shows varying degree of angular misalignment.

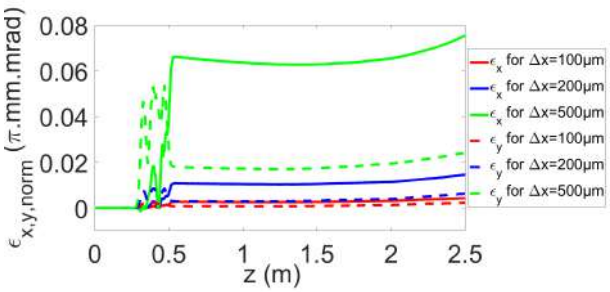

Figure 4.15.: Evolution of horizontal and vertical emittance $\epsilon_{x,y,norm}$ along the longitudinal axis in case of horizontal misalignment Δx of the gun solenoid. Colored curves indicates difference in emittance, $\epsilon_{aligned} - \epsilon_{misaligned}$ for various degree of misalignment. The more the solenoid is misaligned, the more emittance increases.

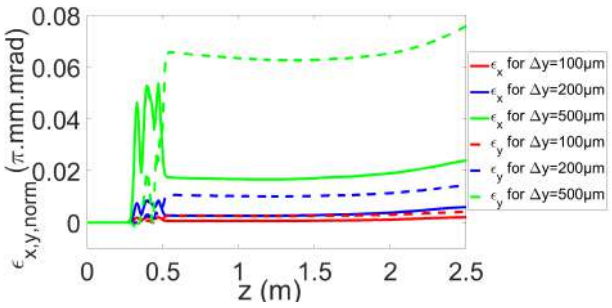

Figure 4.16.: Evolution of horizontal and vertical emittance $\epsilon_{x,y,norm}$ along the longitudinal axis in case of vertical misalignment Δy of the gun solenoid. Colored curves indicates difference in emittance, $\epsilon_{aligned} - \epsilon_{misaligned}$ for various degree of misalignment. The more the solenoid is misaligned, the more emittance increases.

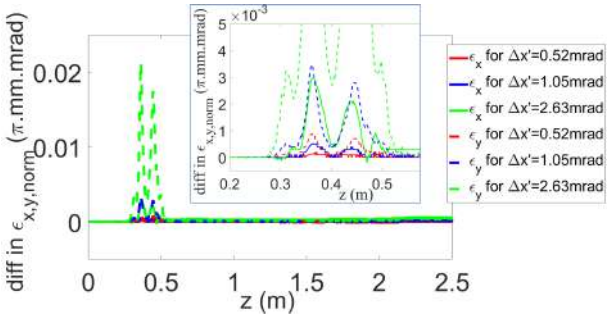

Figure 4.17.: Emittance growth as a function of solenoid misalignment in x-z plane. Inset has change of scale to zoom in on emittance growth.

growth for combination of misalignment for all four cases, namely two transverse direction and tilts angles of x-z and y-z planes.

This exercise of introducing the misalignment in solenoid and studying its effects on beam positions and emittance gives a useful insight about the dynamics of misaligned solenoid. A misaligned solenoid can considerably affect the beam trajectory and can result in emittance growth. Hence it must be aligned to the limit of the micro mover system to transport beam into the linac and the experimental areas to achieve desired beam parameters.

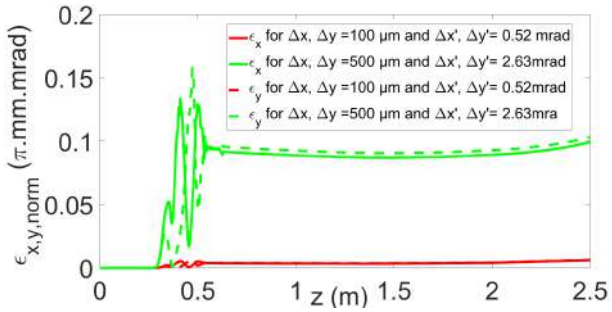

Figure 4.18.: Plot of difference in emittance for a misaligned solenoid w.r.t aligned case ($\epsilon_{misaligned} - \epsilon_{aligned}$). Red line is for misalignment of 100 μm for both transverse direction and angular offset of 0.52 mrad. Green line is for 500 μm misalignment and 2.63 mrad angular offset.

4.4. Algorithm for beam based alignment scheme

The alignment model is based on the transfer matrices to describe the transverse beam displacement at the observation point downstream the solenoid. This approach is valid since there is no overlap of the magnetic field "B" of the solenoids with the electric field "E" of the RF gun. If this is not the case, more complex numerical methods need to be adopted such as in [64]. Recently, a similar scheme has been implemented at BNL [66].

The generalized transfer matrix is calculated by using the beam momentum and magnetic measurement data. For a coil with strength K and magnetic length l, the transfer matrix for positive and negative polarity is given by equations 4.2 and 4.3 respectively [31]. The beam dynamics inside a solenoid magnet is explained in section 2.3.3. The transfer matrix for the solenoid is derived in appendix A and is given by equation 4.4. Two screens are located downstream the solenoid for beam profile measurement.

$$M_{sol+} = \begin{pmatrix} cos^2(Kl) & \frac{sin(Kl)cos(Kl)}{K} & sin(Kl)cos(Kl) & \frac{sin^2(Kl)}{K} \\ -Ksin(Kl)cos(Kl) & cos^2(Kl) & -Ksin^2(Kl) & sin(Kl)cos(Kl) \\ -sin(Kl)cos(Kl) & \frac{-sin^2(Kl)}{K} & cos^2(Kl) & \frac{sin(Kl)cos(Kl)}{K} \\ Ksin^2(Kl) & -sin(Kl)cos(Kl) & -Ksin(Kl)cos(Kl) & cos^2(Kl) \end{pmatrix} \tag{4.2}$$

$$M_{sol-} = \begin{pmatrix} cos^2(Kl) & \frac{sin(Kl)cos(Kl)}{K} & -sin(Kl)cos(Kl) & \frac{-sin^2(Kl)}{K} \\ -Ksin(Kl)cos(Kl) & cos^2(Kl) & Ksin^2(Kl) & -sin(Kl)cos(Kl) \\ sin(Kl)cos(Kl) & \frac{sin^2(Kl)}{K} & cos^2(Kl) & \frac{sin(Kl)cos(Kl)}{K} \\ -Ksin^2(Kl) & sin(Kl)cos(Kl) & -Ksin(Kl)cos(Kl) & cos^2(Kl) \end{pmatrix} \tag{4.3}$$

$$M_{drift} = \begin{pmatrix} 1 & d & 0 & 1 \\ 0 & 1 & 0 & 0 \\ 0 & 0 & 1 & d \\ 0 & 0 & 0 & 1 \end{pmatrix} \tag{4.4}$$

The total transfer matrix acting on the beam is combination of M_{sol+}, M_{sol-} and M_{drift}, depending on the choice of polarity settings. The two possible combinations for PP and MP polarity settings are given by Equations 4.5 and 4.6 respectively.

$$PP = M_{drift} \cdot M_{sol+} \cdot M_{sol+} \tag{4.5}$$

$$PM = M_{drift} \cdot M_{sol-} \cdot M_{sol+} \tag{4.6}$$

The final coordinates of the electron beam are determined from its initial position using the total transfer matrix M of the lattice.

$$\overline{F} = M \cdot \left(\overline{X} + \overline{\Delta X}\right) \tag{4.7}$$

Where $\overline{F}$ is final beam position vector, $\overline{X}$ is initial beam position vector, $\overline{\Delta X}$ represents the offset in initial beam positions between the electron beam and the magnetic axis of the solenoid and M is the transfer matrix of the lattice.

Assuming that the reference system has origin on the solenoid axis and that the beam has an offset with respect to this system, the initial position vector $\overline{X}$ will become zero and the equation will be reduced to

Electron beam via laser alignment is on axis and the solenoid has a misalignment. However, the transport through the solenoid is calculated by imposing a virtual electron beam offset $\overline{\Delta X}$ which is equal to the misalignment of the solenoid but in opposite direction, while the solenoid is virtually on axis. This reduces the equation 4.7 to

$$\overline{F} = M \cdot \overline{\Delta X} \tag{4.8}$$

or in matrix notation

$$\begin{pmatrix} x_f \\ x'_f \\ y_f \\ y'_f \end{pmatrix} = \begin{pmatrix} M_{11} & M_{12} & M_{13} & M_{14} \\ M_{21} & M_{22} & M_{23} & M_{24} \\ M_{31} & M_{32} & M_{33} & M_{34} \\ M_{41} & M_{42} & M_{43} & M_{44} \end{pmatrix} \cdot \begin{pmatrix} \Delta x_i \\ \Delta x'_i \\ \Delta y_i \\ \Delta y'_i \end{pmatrix} \tag{4.9}$$

During beam based alignment (BBA), we will need to adjust the position of the solenoid, by adjusting the four degrees of freedom of its mover on the reference trajectory, on which the electron beam will be pre-aligned having set initially the solenoid off. Therefore a correction equal to $-\overline{\Delta X}$ will have to be applied to the solenoid in order to align it with the reference beam trajectory. Inside vector $\overline{F}$, only x_f and y_f can be measured during alignment procedure which we read from the screen. Hence, only two out of four equations in equation 4.9 are usable. However, for a fixed solenoid position, the final positions of the electron beam on a measurement screen downstream the solenoid will be different for any value of solenoid strength or polarity settings, but the initial misalignment will be the same. Exploiting this fact gives us the freedom to construct a redundant system of equations according to our choice of solenoid strength and polarity settings. The new matrix is formed by piling up the elements of the transfer matrix in equation 4.9 corresponding to a specific solenoid current as shown below.

$$\begin{pmatrix} x_{f1} \\ y_{f1} \\ x_{f2} \\ y_{f2} \\ \dots \\ \dots \\ x_{fN} \\ y_{fN} \end{pmatrix} = \begin{pmatrix} M_{11,1} & M_{12,1} & M_{13,1} & M_{14,1} \\ M_{31,1} & M_{32,1} & M_{33,1} & M_{34,1} \\ M_{11,2} & M_{12,2} & M_{13,2} & M_{14,2} \\ M_{31,2} & M_{32,2} & M_{33,2} & M_{34,2} \\ \dots & \dots & \dots & \dots \\ \dots & \dots & \dots & \dots \\ M_{11,N} & M_{12,N} & M_{13,N} & M_{14,N} \\ M_{31,N} & M_{32,N} & M_{33,N} & M_{34,N} \end{pmatrix} \cdot \begin{pmatrix} \Delta x_i \\ \Delta x'_i \\ \Delta y_i \\ \Delta y'_i \end{pmatrix} \tag{4.10}$$

In Equation 4.10 the third index of transfer matrix elements identify the specific current value. Solution of equation 4.10 to determine $\overline{\Delta X}$, gives the misalignment of the solenoid which is equal to quantities in $\overline{\Delta X}$ but in opposite direction.

In order to analyze the measured data, a MATLAB tool has been written. The routine provides a graphical user interface to select the polarity settings. The panel solves the system of linear equations using least square methods by minimizing the $|\overline{F} - M \cdot \overline{\Delta X}|$. The user panel also displays the confidence interval for the regression fit by calculating margin of error [68]. The confidence interval describes the uncertainity of the measured data and margin of error defines an interval estimate that describes the precision of the solution. The convergence of the method and sensitivity to the measurement errors depends on the calculated transfer matrix $M^T M$. To calculate the confidence interval (CI), first the standard error of the measured data and then the critical value for linear regression using t-score distribution is calculated. This gives us the margin of error, ϵ where $\epsilon = criticalvalue * standarderror$. The confidence interval is $CI = calculatedvalue \pm \epsilon$. The displayed confidence interval shows 98% certainty that the misalignment lies within the given interval.

According to the measured misalignment, the solenoid position is corrected using the manual micro mover system. To check if the solenoid is aligned, the beam almost does not move on the screen as a function of solenoid current. In other words, the solenoid focusing can be varied without effecting the beam trajectory. If this is not the case, the measurement is repeated for another iteration of the correction of the alignment.

4.5. Benchmarking the alignment algorithm with ASTRA simulations

A measurement was simulated to benchmark the developed routine using the ASTRA particle code [51]. A misalignment of the solenoid is introduced with respect to the beam trajectory in the input lattice-file in ASTRA. Positions of the beam at the measurement screen were recorded and used as input to test the routine for the data analysis.

Before looking at the results, it is important to note the differences between the analytical model used by the MATLAB routine and the particle tracking algorithm used to simulate the beam dynamics in ASTRA. ASTRA directly applies the force generated by the magnetic field of the solenoid to each particle. The transverse magnetic field components are calculated from the derivatives of the on-axis field profile, which is provided in the input files for the simulation. The MATLAB routine uses instead the linear transfer matrix formalism. The specific transfer matrix used in the MATLAB-tool is derived for a "flat-top" longitudinal magnetic field component B_z, that is significantly different from the field profile of our solenoid under study also shown in figure 4.6. This method has the advantage of being extremely simple, quick and easy to implement within the accuracy level of the micromover systems of solenoid magnets at ARES. The algorithm was rigorously tested with different cases of initial misalignment in ASTRA varying both the magnitude and the direction of the misalignment.

In ASTRA, a measurement is simulated by introducing a misalignment Δ in solenoid and collecting the beam positions for the scanned current. The beam positions are then fed into the alignment tool

to calculate back the initial misalignment. The error E is defined as the percentage difference between introduced offsets in ASTRA and what we get back from the alignment algorithm. The error function E is calculated according to equation 4.11.

$$\%E = abs\left(\frac{(\Delta_{ASTRA} - \Delta_{tool})}{\Delta_{ASTRA}}\right) * 100 \tag{4.11}$$

The benchmark of the analysis method with simulations has been performed for different cases:

1. Considering purely solenoid position offsets , $\Delta x,\ \Delta y$
2. Considering purely solenoid angular offsets , $\Delta x',\ \Delta y'$
3. Both offsets in solenoid position and angle, $\Delta x,\ \Delta y,\ \Delta x'$ *and* $\Delta y'$

Range of offsets introduced in solenoid in ASTRA simulations:

- $\Delta x,\ \Delta y$ = -3 to +3 mm
- $\Delta x',\ \Delta y'$ = -3 to +3 mrad

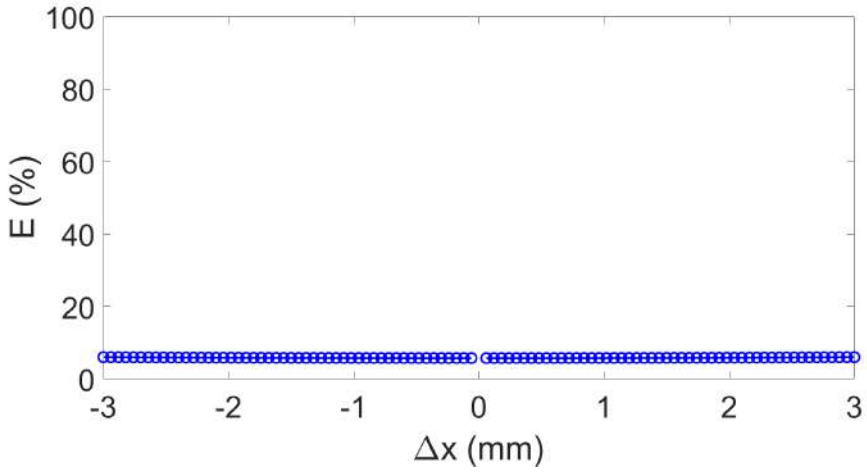

Figure 4.19.: Comparison of at the measurement screen. The error is defined according to equation 4.11. The misalignment is introduced in x-direction in the solenoid. From ASTRA simulation, beam positions at the measurement screen are recorded and input in the MATLAB routine. The percentage error is plotted as a function of introduced misalignment according to equation.

The comparison results have been published in [58]. The gun solenoid under discussion is a double coil solenoid which will be operated in minus-plus polarity settings as explained in section 4.2.1, the kick introduced because of angular offsets in the beam trajectory is compensated. This shortcoming of the algorithm based on linear transfer matrix becomes negligible in our case. To prove this point, a measurement was simulated in ASTRA, in which misalignment of 1 mm in x was introduced and the beam trajectory was plotted on screen by varying the solenoid current. Same measurement was simulated again by introducing the misalignment of 1 mrad only in the x-z plane. Figure 4.20 shows the plot of

beam trajectory. It can be easily observed that for 1 mm misalignment, the beam shifts by 7.36 mm on the screen and for angular misalignment of 1 mrad, the beam shifts by 0.003 mm, which is less than the screen resolution as given in section 3.3.3.2. Therefore for the solenoid of ARES gun, the developed algorithm could be safely adopted and works well within the accuracy range of the micromover system.

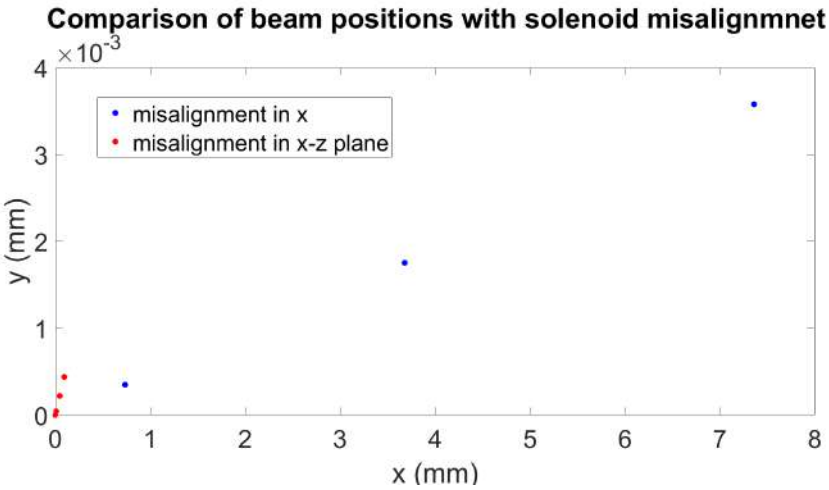

Figure 4.20.: Plot of beam trajectory on screen for misaligned solenoid in minus-plus polarity settings. Beam shifting on screen by 7.36 mm in x for misalignment of 1 mm in x direction. Beam shifting by 0.003 mm on screen for misalignment of 1 mrad in angular plane.

Effects of misalignment in longitudinal position

If the solenoid is misaligned in z-direction, it will result in the variation of drift matrix. Solenoid position moved from ± 5 mm w.r.t central value, and the effect of the beam on the screen is observed for a fixed misalignment of solenoid in x equal to 200 μm. Figure 4.21 shows the simulated effects beam experiences in ASTRA as a result of misalignment of solenoid in z- direction. Even for an overestimated misalignment of ± 5 mm, the response is within few % compared to the reference longitudinal position.

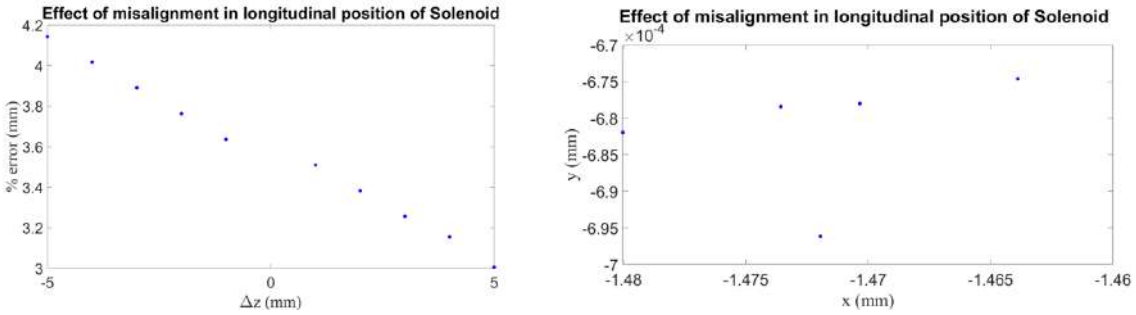

Figure 4.21.: Same as in figure 4.19. The left hand side plot gives variation in error calculated from routine as a result of misalignment in z for a fixed misalignment in x of 200 μm. The variation is 1% for $\Delta z = \pm 5$ mm. The right hand side plot shows the beam position on screen as a result of misalignment in z-position of solenoid. The beam experiences a maximum kick of 0.2 mm.

4.6. Error analysis

Systematic study is performed to determine the error on the alignment algorithm. There can be multiple sources of error in the system to determine the misalignment in the solenoid. The gun solenoid system along with the possible sources of misalignment, that can deviate beam trajectory from the design orbit and can cause emittance growth [60, 61], according to ARES accelerator coordinates is shown in figure 4.23. For a misaligned system of figure 4.23, beam position at the screen x_{scr} is determined by the

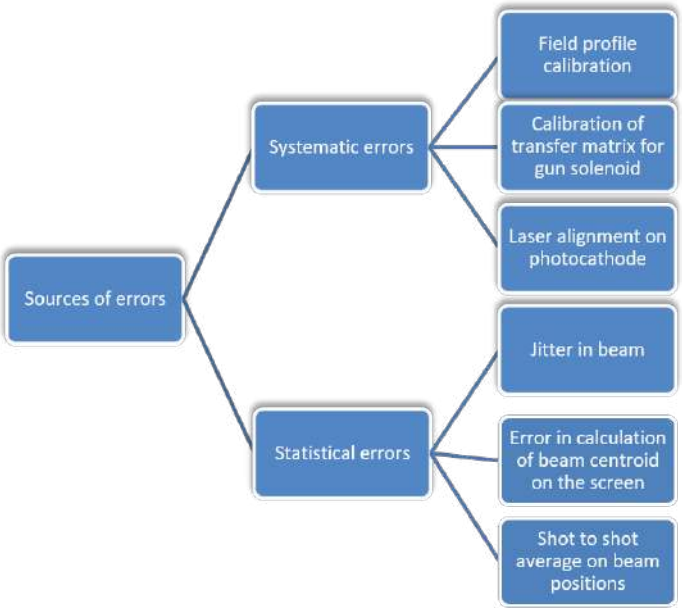

Figure 4.22.: Source of errors in the system to determine the misalignment in the solenoid at ARES gun.

relation

$$\begin{aligned} x = {} & f_1\left(\Delta x_{sol}\right) + f_2\left(\Delta x'_{sol} \cdot z_{scr} - z_{sol}\right) + f_3\left(\Delta x_{las}\right) + f_4\left(\Delta x'_{las} \cdot z_{scr}\right) \\ & + f_5\left(\Delta x_{cat}\right) + f_6\left(\Delta x'_{cat} \cdot \left(z_{scr}\right)\right) + f_7\left(\Delta x_{cav}\right) + f_8\left(\Delta x'_{cav} \cdot \left(z_{scr} - z_{cav}\right)\right) \end{aligned} \tag{4.12}$$

$$x' = h_1\left(\Delta x'_{sol}\right) + h_2\left(\Delta x'_{las}\right) + h_3\left(\Delta x_{cat}\right) + h_4\left(\Delta x_{cav}\right) \tag{4.13}$$

where x and x' are the electron beam position and angle relative to solenoid axis. $z_{...}$ represents the longitudinal position of the respective beam line element. Each of the error term in equation 4.12 and 4.13 contributes to the beam trajectory. The impact of the each error terms and how it is minimized is discussed below.

- Δx_{sol} and $\Delta x'_{sol}$ are the transverse and angular offsets introduced in the beam trajectory due to misalignment in the solenoid.
- Δx_{las} and $\Delta x'_{las}$ are the transverse and angular offsets introduced in the beam trajectory due to misalignment of the laser on the cathode. If the laser is misaligned on the cathode, beam is not

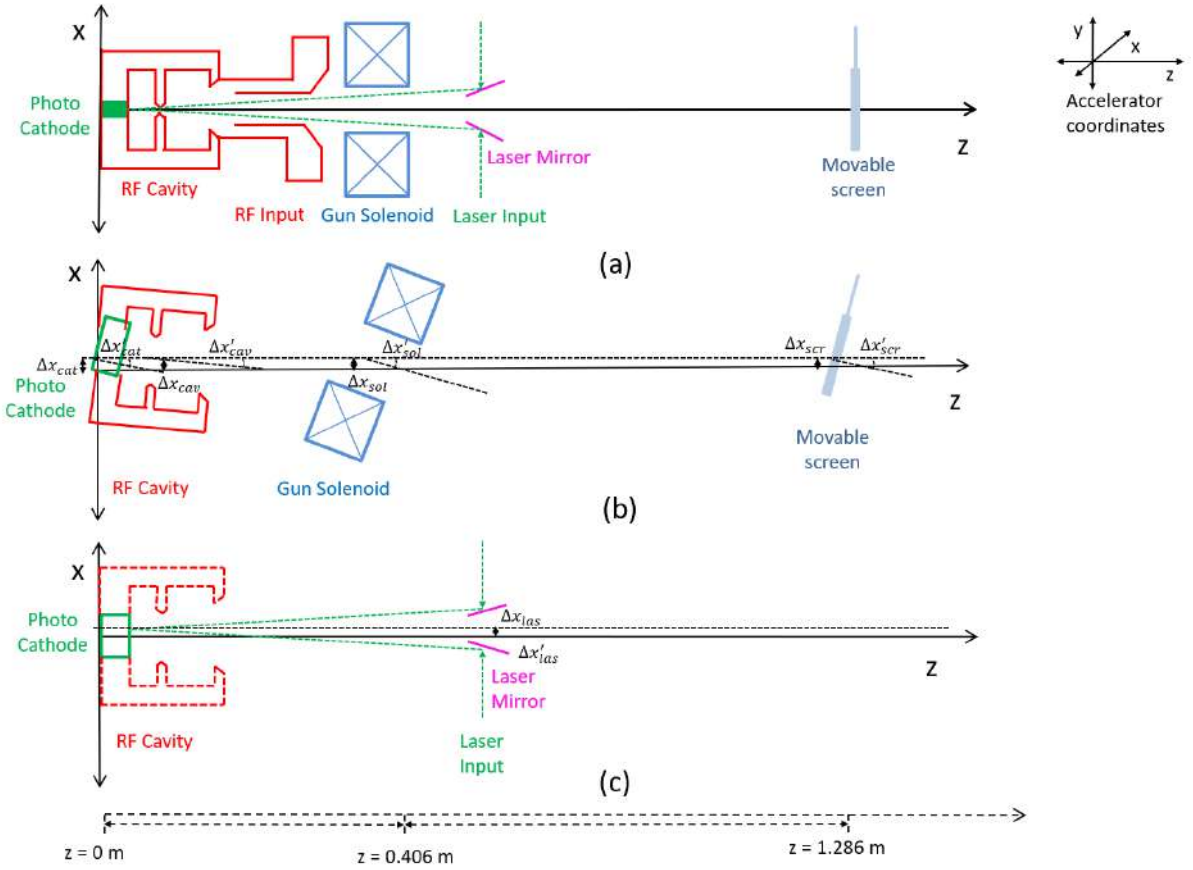

Figure 4.23.: Schematic of the ARES gun beam line together with screen used for solenoid alignment in the accelerator coordinate system. (a) shows all elements in beam line perfectly aligned with respect to accelerator coordinate system. (b)shows the misaligned elements with the offsets in transverse and angular positions. (c) for simplicity, laser coupling is shown separately in this figure. The transverse dimensions of beam line elements is not to the scale.

emitted at the center of the gun cavity and beam experiences additional kick due to focusing RF field.

- Δx_{cat} and $\Delta x'_{cat}$ are the transverse and angular offsets introduced in the beam trajectory in case the cathode is misaligned with respect to the gun cavity axis. If cathode is not centered or is tilted with respect to the gun cavity, the beam will not be centered in the cavity. The focusing fields generated in the cavity would give a kick to the beam and hence it can be impacted.

- Δx_{cav} and $\Delta x'_{cav}$ are the transverse and angular offsets introduced in the beam trajectory in case gun cavity is not aligned. If the gun cavity is misaligned, the accelerating field of the cavity imparts transverse kick on the electron beam [60].

During the installation of ARES, both cathode and gun cavity are well aligned with the pre-defined accelerator coordinates. Hence the contribution from these terms is ignored. Laser alignment is performed prior to solenoid alignment to eliminate the contribution of laser misalignment on beam trajectory. Therefore the equation 4.12 and 4.13 reduces to

$$x = f_1\left(\Delta x_{sol}\right) + f_2\left(\Delta x'_{sol} \cdot z_{scr} - z_{sol}\right) \tag{4.14}$$

$$x' = h_1\left(\Delta x'_{sol}\right) \tag{4.15}$$

In the real system, in addition there will be remnant errors from both alignments since both alignment procedures, for the laser and the solenoid, can be done only within a given precision. In the case of gun solenoid this is 100μm owing to the movement accuracy of the solenoid positioning system. The alignment procedure for the laser beam and its sensitivity is explained in section 5.2.

To determine the response of the error terms in equation 4.14 and 4.15, measurements were simulated in ASTRA to scan each misalignment parameter namely Δx_{sol} and $\Delta x'_{sol}$ as a function of beam position on screen. The scan data then is fitted to determine the response function. As is shown in figure 4.24 and 4.25, equivalence relation between transverse and angular offset can be estimated as approx 3 orders of magnitude higher for transverse offset compared to angular offsets.

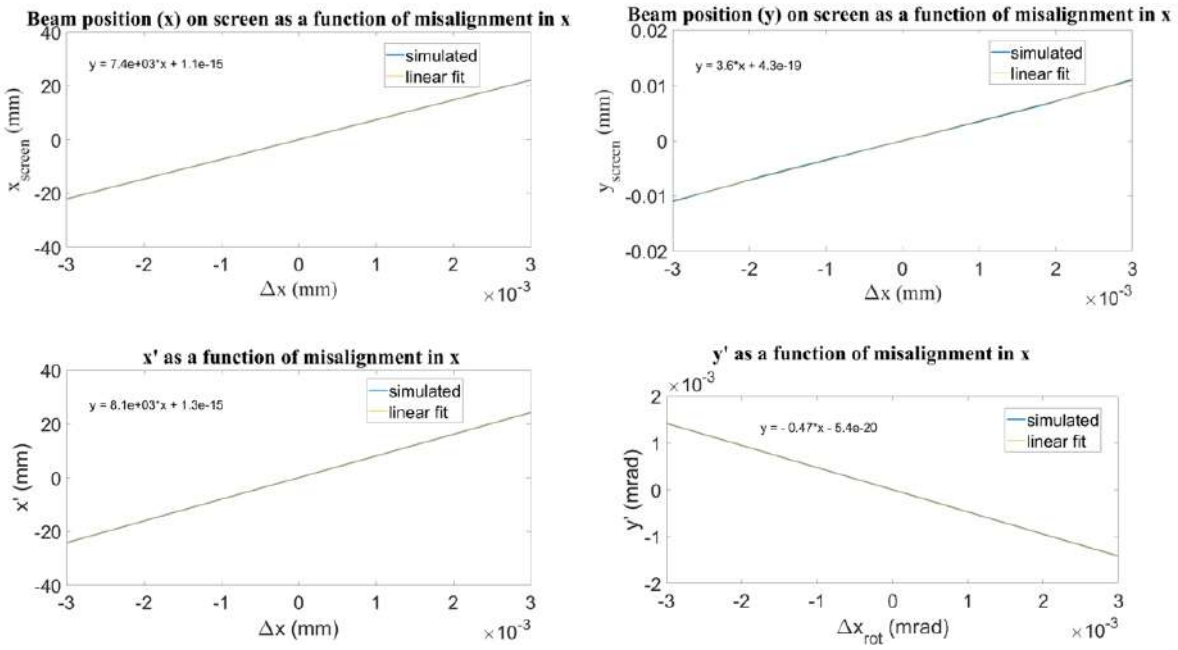

Figure 4.24.: Plot of beam trajectory on screen as a function of transverse misalignment Δx_{sol} in solenoid. The lower plots shows the angular displacement. The misalignment in solenoid has a linear response function on the beam trajectory.

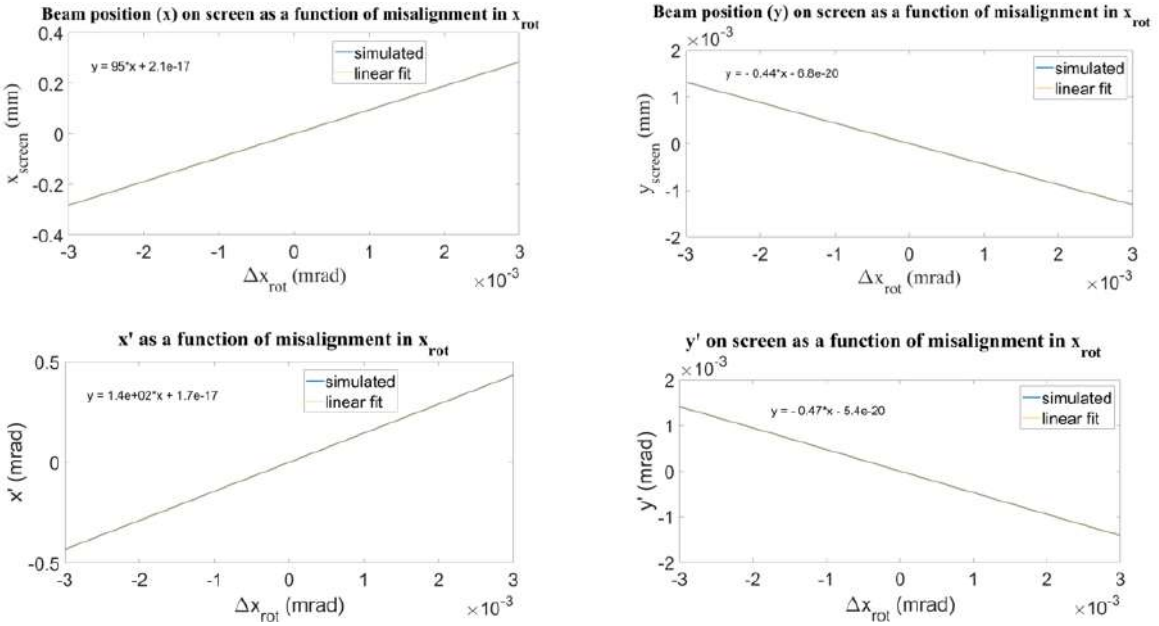

Figure 4.25.: Plot of beam trajectory on screen as a function of angular misalignment $\Delta x'_{sol}$ of solenoid in the x-z plane. The misalignment in solenoid has a linear response function on the beam trajectory.

4.7. Alignment of solenoids around travelling wave structures

There are four solenoids around each travelling wave structure at ARES, as visible in figure 3.10. The solenoids were manufactured and measured by Scanditronix [69]. The excitation curve for one of the solenoids along TWS1 is shown in figure 4.26. The solenoid current I to field calibration B is given by equation 4.16. The measured magnetic field profile along the beam axis from the solenoid center is shown in figure 4.27.

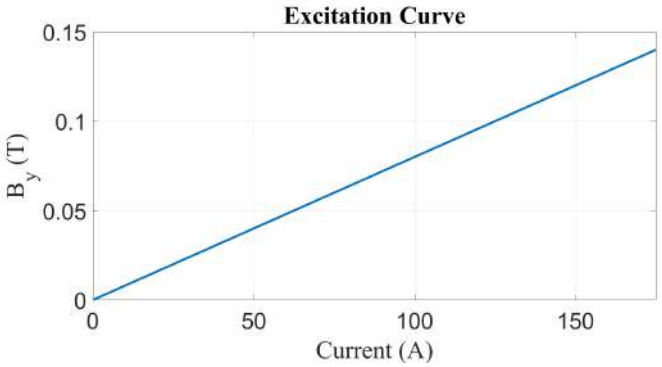

Figure 4.26.: Excitation curve for the solenoid around TWS1. On axis magnetic field is plotted as a function of solenoid current. Magnetic measurements performed at [69].

$$B\ (T) = 0.001 * I\ (Amp) \tag{4.16}$$

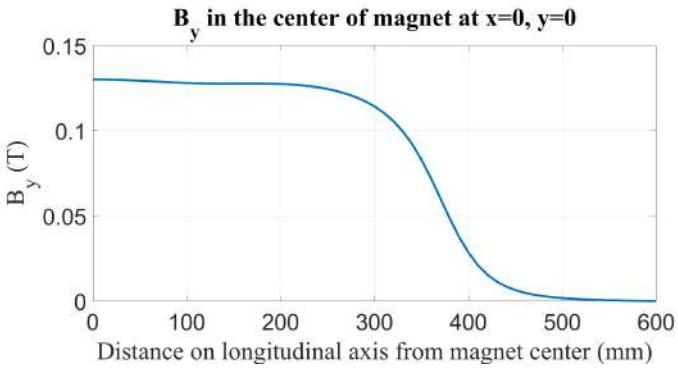

Figure 4.27.: Measured magnetic field profile the solenoid around TWS1. Magnetic field in Tesla is plotted along the beam axis. Magnetic measurements performed at [69].

The same algorithm was used for the beam based alignment of solenoids around travelling wave structures as well. The Matlab tool was extended to include the calculations for all 8 solenoids of TWS. The screen shot of the tool is shown in figure 4.28.

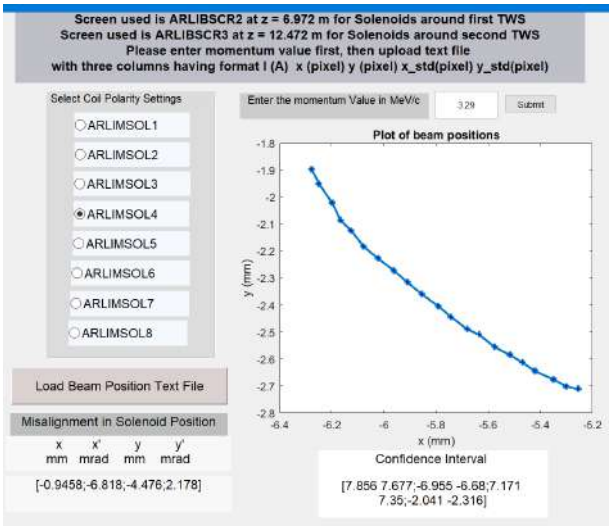

Figure 4.28.: Image of Matlab tool panel for calculating misalignment of solenoids around TWS.

4.8. Conclusion

Alignment of focusing elements of RF gun and linac is a very important setup in achieving the good quality beam. For the ARES commissioning, an algorithm was developed to determine the misalignment in solenoids installed at the RF gun and around travelling wave structures. The alignment algorithm, based on the linear transfer matrices, has been developed and verified with ASTRA simulations. The possible sources of errors in the ARES beam line and their impacts in determining the misalignment were discussed. The developed algorithm is generic and could be adopted for any accelerator facility for the alignment of the focusing solenoids.This helps in achieving the on-axis field trajectory resulting in a good quality beam with design parameters.

5

Experimental Results for Beam Based Alignment of Focusing Solenoids at ARES

5.1. Introduction

In this chapter, the experimental results for the alignment of the focusing solenoid for ARES RF gun and the solenoids around the TWS are presented and discussed. The 5 MeV RF gun of ARES was commissioned in the end of 2019. The gun was conditioned up to a maximum power of 4 MW corresponding to a gun gradient of 70 MV/m using 6 μs long laser pulses for optimized operation. The image of the unoptimized first beam obtained from the ARES RF gun after commissioning is shown in figure 5.1. The results from this chapter of the thesis have been partially published in [70] and the rest are under process, yet to be published as a research article.

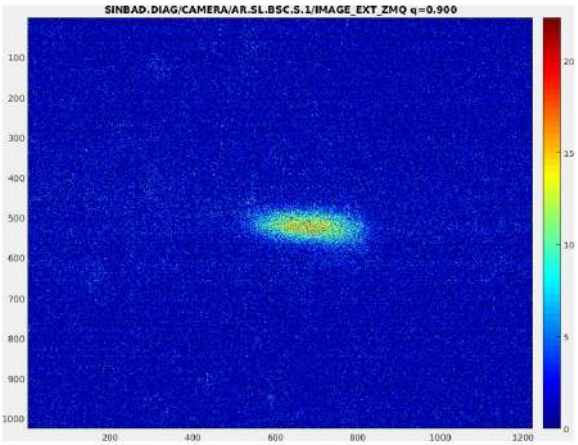

Figure 5.1.: The unoptimized first beam from the ARES gun.

After successful conditioning of the RF gun, the next step is to optimize the beam parameters. It is very important to perform beam based alignment (BBA) of the solenoids on the ARES linac to develop an on-axis beam trajectory for optimized beam emittance. In chapter 4, an algorithm has been developed for this purpose. The results of the BBA of the solenoid magnets during ARES commissioning are presented in this chapter. Table 5.1 summarizes the beam line elements used for the experimental data in this chapter.

Table 5.1.: Summary of the beamline elements used for taking the experimental data. The longitudinal z position corresponds to the center of the element.

Element name	**Purpose**	z**(m)**
SOG1	Focusing solenoid for the RF gun	0.406
CHG1	Horizontal steerer after the gun	0.661
CVG1	Vertical steerer after the gun	0.661
X1	Screen after the gun	1.298
R1	Screen before the TWS1	2.366
SOL1	First solenoid around TWS1	3.088
SOL2	Second solenoid around TWS1	4.087
SOL3	Third solenoid around TWS1	5.087
SOL4	Fourth solenoid around TWS1	6.060
R2	Screen between the two TWSs	6.972
R3	Screen after the TWS2	12.472

5.2. Alignment procedure

In this section, procedures adopted for the alignment of the laser on the photocathode and the focusing solenoids at ARES are described.

5.2.1. Laser alignment on the cathode

The photocathode laser should be aligned on the cathode as a prerequisite of BBA of the gun solenoid. If this is not the case, the electron beam will be travelling off axis in the gun cavity, and hence can experience an additional kick due to the focusing effects of the RF fields from the gun cavity. The laser was aligned using the auto alignment tool developed for the Pharos laser at DESY. The tool adjusts the laser mirror positions remotely by using the stepper motors to focus the laser beam on the predefined optimal point setting. Multiple iterations were performed to align the laser. To test for the laser alignment, the beam positions on screen X1 were recorded as a functions of the gun phase. If the laser is aligned on the cathode and the earth magnetic field is fully compensated, implying the electron beam is travelling on-axis in the gun cavity, then beam should not be moving on the screen with the changing gun phase.

Multiple iterations were performed to align the photocathode laser on the cathode. The following strategy was adopted for this measurement.

- The gun solenoid should be kept switched off for all iterations.

- The measurement was started off by adjusting the horizontal and vertical steerer before the screen X1, so that the beam is in the field of view of the camera optics.
- The beam position at screen X1 was measured by scanning the gun phase. This determined the direction in which the laser should be moved to center it on the photocathode.
- Using the Pharos-laser auto alignment tool, the laser position was moved. Ideally, the horizontal and vertical steering magnets should be kept off. However without steering at the start, the beam was out of the field of view of the camera optics and not visible on the screen. Therefore, for the first iteration the beam was kept in the field of view of the screen using the steerers. The laser position was overshot in the opposite direction and adjusted to the required position by gradually reducing the strength of the steerer magnets.
- The last two steps were repeated multiple times in both x and y directions, until the horizontal and vertical steerer were switched off and the beam was in the field of view of screen X1.
- The measurement was stopped when the beam offsets as a function of the gun phase, in both x and y direction, were reduced to a minimum.

5.2.2. Alignment of solenoids

The following procedure is adopted for measuring the BBA of solenoids at ARES.

- Fix the first setup for the polarity of the coils (e.g. minus-plus).
- Record images for determining the position x and y on the measurement screen by scanning the solenoid current.
- Record background images for subtraction from the beam images to remove any incidence of dark current.
- The saved images are then processed to calculate the center of mass of the beam to determine the beam positions in both transverse planes x and y for each current value.
- At the end of the measurements, we enter the beam positions data together with the corresponding current value in the Matlab tool which will display the offsets in the solenoid misalignment.
- According to the calculated offsets, the alignment group corrects the solenoid position in the tunnel using the micro mover system. The correction needs to be applied manually, as moving the solenoids remotely is not possible at ARES. The alignment was corrected stepwise. Of the misalignment in the x and y planes the larger one is corrected first. Then the measurement is repeated for the correction of misalignment in the other direction.

- After the solenoid has been aligned, the measurement is repeated to recalculate the misalignment numbers.

- Check if the solenoid is aligned: For an aligned solenoid, when changing the solenoid current, the beam almost does not move on the screen anymore since the beam moves on axis and hence does not experience kicks in the transverse planes.

- If this is not the case, we need to repeat the procedure and do another iteration of the correction of the alignment.

- Since it is an iterative process, multiple iterations may be needed to reduce the error.

Ideally, the laser on the photocathode is aligned first followed by consecutive iterations for the alignment of the gun solenoid. However, since ARES was newly commissioned and many tools and diagnostics, both on laser and electron beam side, were developed in parallel. The order of measurements was different from the ideal case. Also, there were significant developments on the ARES beam line between the two iterations which prevented the correlation of the misalignment numbers before and after aligning the solenoid. Experimental results and associated conditions for each measurement are discussed in the following sections.

5.2.3. Screen calibration

The saved beam and background images are processed to extract the beam centroid data. Multiple images at each current set point are recorded for both background and beam. The images are then averaged out. The averaged background image is subtracted from averaged beam image. The pixel corresponding to the peak intensity in the region of interest around the beam is taken as the centroids data in both x and y planes. The pixel-mm screen calibration for the screens used during BBA measurement is shown below.

Calibration for screen X1:

$$\begin{aligned} x &= 3.728 \times 10^3 \; mm/pixel \\ y &= 2.712 \times 10^3 \; mm/pixel \end{aligned} \tag{5.1}$$

Calibration for screen R2:

$$\begin{aligned} x &= 3.558 \times 10^3 \; mm/pixel \\ y &= 2.557 \times 10^3 \; mm/pixel \end{aligned} \tag{5.2}$$

Calibration for screen R3:

$$x = 3.717 \times 10^3 \; mm/pixel$$
$$y = 2.579 \times 10^3 \; mm/pixel \tag{5.3}$$

5.3. BBA of solenoid for ARES gun I

The gun conditioning of ARES was followed by the BBA of the gun solenoid of ARES. Before taking the data for the gun solenoid alignment, the alignment of the photocathode laser was measured. Since the tool for the alignment of the photocathode laser, as explained in section 5.2.1, was under development at this point in time, the laser alignment could only be estimated and could not be improved.

For recording the beam positions as a function of the gun phase, a scan was taken with the following conditions. The gun probe was set at ∼2.6 MW, as shown in figure 5.2. The RF gradient was set at moderate values to avoid the dark current background as shown in figure 5.3. Beyond this value, the dark current was very high in the nC range which could pose a risk to the diagnostic devices. In comparison, the beam charge spectrum as a function of the gun solenoid measured by the Faraday cup is shown in figure 5.4. The laser attenuation was set at the maximum value 8000 corresponding to 17.6 pC. The horizontal and vertical steerer were switched off and the low energy spectrometer dipole was cycled to zero field values to prevent effects of any remnant field from the dipole. For all the data points, ten images for both the beam and the background were averaged and then processed. The background was subtracted from the beam images and centroids were calculated using a Matlab routine to read the values of the center of the Gaussian fit on the camera panel.

Figure 5.5 shows a scan of the gun RF phase and the corresponding beam positions. The excursion of the centroids in x seems to be well below 100 μm which is sufficiently good, while the excursion in y is about 250 μm which is a bit on the higher side. The large error bars in x seem to depend on some spurious few points in the set which give a totally different value than the expected centroid position. This might be due to fluctuations of the camera. However, it should be noted that the solenoid current was fixed at a constant value of 60 A during this measurement. This will introduce an additional kick on the beam since the energy changes with the gun phase. For such a measurement, the solenoid field should be kept off in principle. However, the gun solenoid had to be switched on to get a very first measurement, because without solenoid field, the beam was out of the field of view of the screen. This measurement was repeated after the gun was exchanged as discussed in detail later in section 5.4. The laser beam was better aligned using the laser optics. As a result, the beam positions as a function of the gun phase without solenoid field and horizontal and vertical steerers could be measured. At this point in operation, we could not further do the alignment of the photocathode laser simply because of the unavailability of the laser optics control system. However, we can cautiously conclude that

- the alignment of the laser beam on the cathode in x seems to be fairly good: $\sim 100 \mu m$ excursion

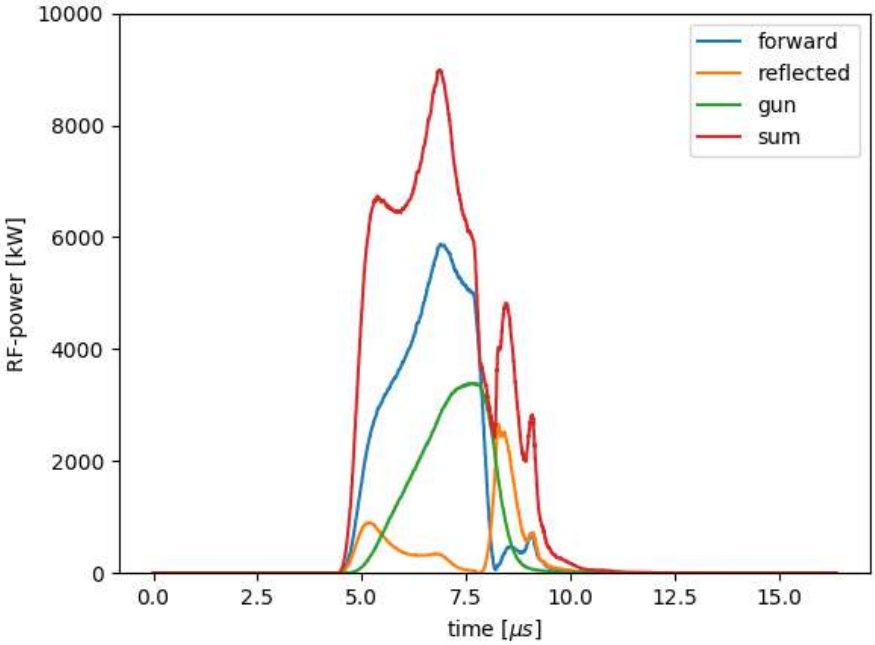

Figure 5.2.: Plot of RF spectra in the gun.

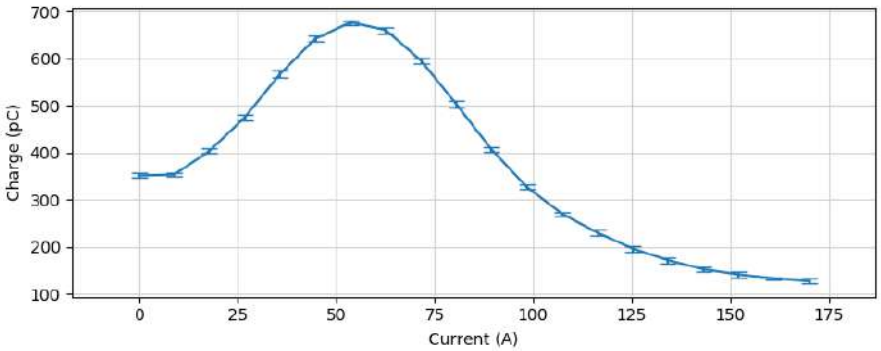

Figure 5.3.: Dark current spectrum at 3.4 MW.

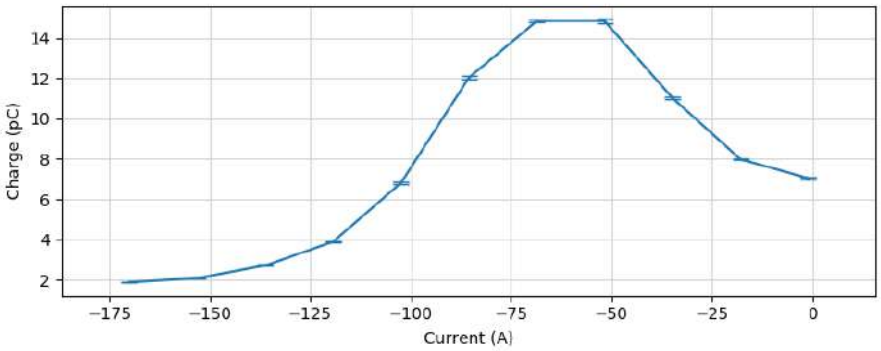

Figure 5.4.: Beam charge at the Faraday cup as a function of the gun solenoid at 3.4 MW.

of the beam centroids on X1 during the phase scan.

- the alignment in y is at the limit of the acceptance of $\sim 250\mu m$ excursion of the beam centroid on X1 during the gun phase scan.

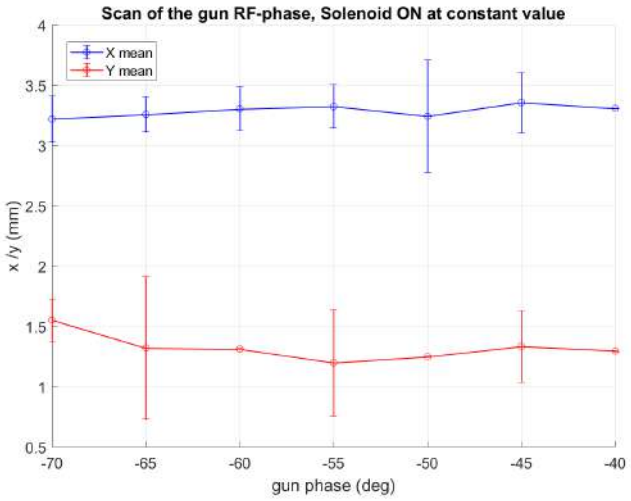

Figure 5.5.: Beam position on screen X1 plotted as a function of the gun phase. This measurement gives the alignment of the laser on the photocathode.

1st Measurement

Data for the BBA of the gun solenoid was taken as an iteration of the beam position measurement as a function of the main solenoid current. For the first iteration, the gun solenoid was operated at the minus-minus polarity setting. The data was taken at two power levels, 3.6 MW and 2.6 MW, corresponding to a beam momentum of 4.56 MeV/c and 3.9 MeV/c respectively. The earth magnetic field corrector coils were switched on at operating values of -8 A in both horizontal and vertical plane. To determine the operating phase, a Schottky scan was performed by measuring the beam charge as a function of the gun phase as shown in figure 5.6.

Figure 5.7 gives the beam positions as a function of the solenoid current and figure 5.8 shows the plot of the beam trajectory on the screen for 2.6 MW.

The centroid data was then used as an input for the alignment routine and the misalignment of the solenoid was calculated. The misalignments calculated from the Matlab tool are shown in table 5.2.

Table 5.2.: Misalignment calculated from the BBA tool for ARES gun1 first iteration. Data taken on 22.01.2020.

Misalignment Direction\Power	**3.6 MW**	**2.6 MW**	**Average**
Δx (mm)	-0.97	-0.87	-0.92
Δy (mm)	0.41	0.44	0.43

The results for both measurements were in a good agreement with each other except for x' where there is a variation of 0.3 mrad. This was followed by a correction of the largest misalignment. The gun solenoid was moved -0.8 mm in x direction according to the accelerator coordinate system as shown in

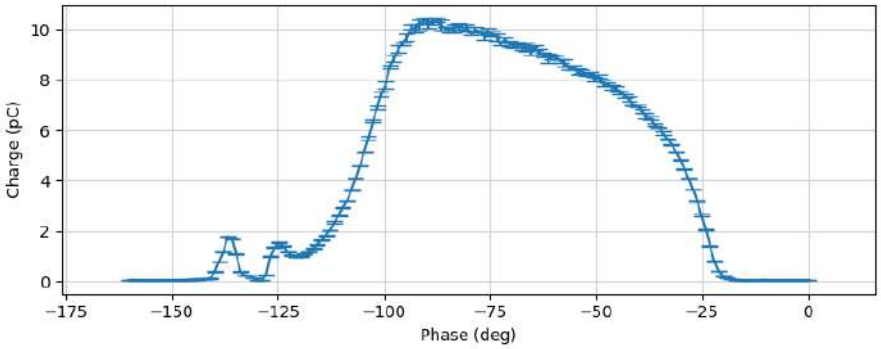

Figure 5.6.: Schottky scan for the first ARES gun.

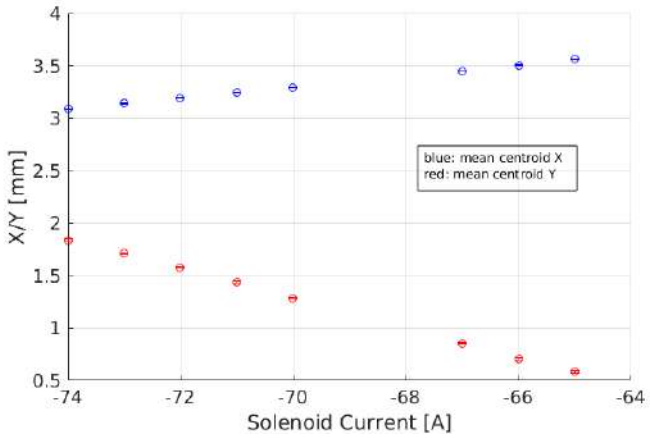

Figure 5.7.: Beam position on screen X1 as a function of the Gun solenoid current.

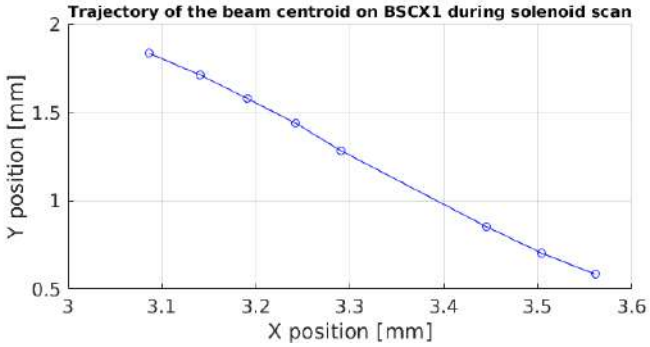

Figure 5.8.: Beam trajectory on screen X1 as a function of the Gun solenoid current.

figure 4.23. Apart from moving the gun solenoid, it was also configured to minus-plus polarity settings. The minus-plus polarity will be the operating polarity as in this configurations, the kick introduced by an angular misalignment of the solenoid is compensated by the opposite polarity of the two coils. Therefore the effects of the angular misalignment become negligible as discussed in detail in section 4.3.

2nd Measurement

The measurement was repeated at both power levels by recording the beam and background images for each set point of the solenoid current. The misalignment values obtained after the 1st iteration are shown in table 5.3.

Table 5.3.: Misalignment calculated from the BBA tool for ARES gun1 second iteration. Data taken on 04.02.2020.

Misalignment Direction\Power	3.6 MW	2.6 MW	Average
Δx (mm)	-0.27	-0.25	-0.26
Δy (mm)	0.11	0.10	0.10

The alignment in x was much improved after the first iteration. However, it was also observed that the solenoid position was also changed in y. This can be explained by the fact that the mover housing the solenoid is not fully decoupled in its horizontal and vertical movement. Also, the angular misalignment is unconstrained which could add a contribution to the transverse offset as well. This was clearly visible on the screen, as the beam was much more centered both in horizontal and vertical direction as shown in figure 5.9. The beam on screen R1, downstream the gun, just before the entrance of TWS1 is shown in figure 5.10. The comparison of the beam on X1 and R1 also confirms that the beam has an angled trajectory and is experiencing a slight kick, most probably owing to the small amount of misalignment in the horizontal direction.

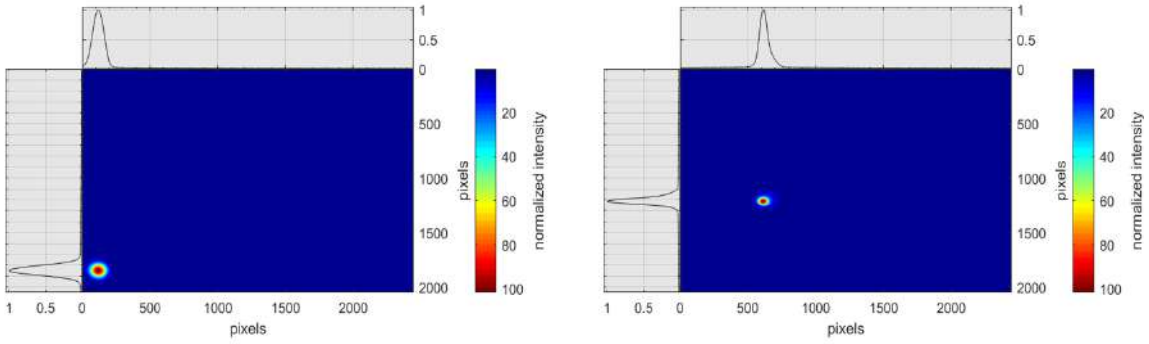

Figure 5.9.: Beam focused on screen X1 before and after the first iteration for BBA of gun solenoid for ARES gun 1.

If the solenoid is well aligned on the screen, the beam should not move or appear not to move as a result of a change in the solenoid current. However, the beam centroids still had a small variation in x and thus a second iteration could be performed. The first iteration was followed by a shutdown of ARES for the

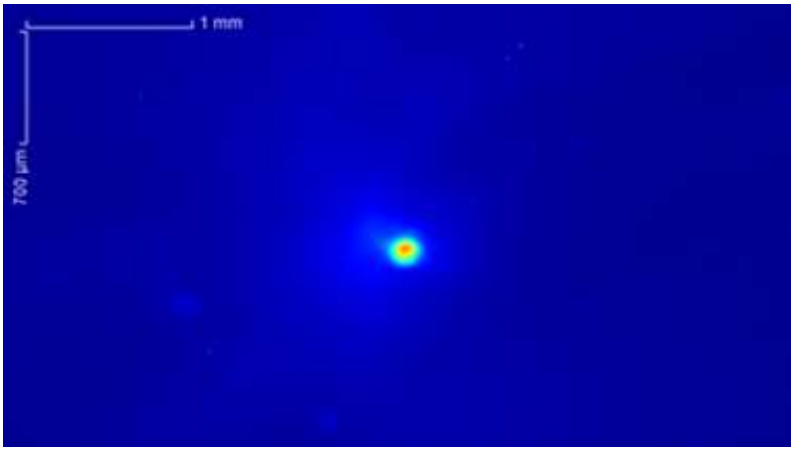

Figure 5.10.: Beam focused on screen R1 after the first iteration of BBA of the gun solenoid for ARES gun 1.

gun upgrade. Further iterations were done after the shutdown. The first iteration shows that the BBA of the gun solenoid based on the linear transfer matrix is a successful tool. It is a generic method which can be applied and routinely used for the alignment of a focusing solenoid. It should however be noted that the rotation angle of the solenoid is not constrained. There is a large uncertainity because of many degrees of freedom coming from a tilted base plate of solenoid, some parasitic coupling between x and y in the positioning system, the angle between the solenoid reference position and the screen reference. Moreover in case of the double coil solenoid operating in minus-plus polarity, the kick due to the rotation angle is compensated. The misalignment in the angular plane is therefore not corrected.

5.4. Alignment of photocathode laser

The laser on the virtual cathode before the alignment is shown in figure 5.11. The image of the auto alignment tool also shows multiple hotspots in the temporal laser profile, which makes it harder to align the laser. It should however be noted that a molybdenum (Mo) cathode was installed in the Gun at this point in operation. The charge from the Mo was too low to allow the use of the collimator to shape the temporal profile of the laser. After availability a Cs_2Te cathode was installed in the later iterations to improve the laser alignment, discussed later in this section. Since the laser was not very well aligned, it was not possible to see the beam on screen X1 without the use of magnets as shown in figure 5.12, where only the edge of a dispersed beam is visible on the screen.

The plot of the beam positions as a function of gun phase is shown in figure 5.13 for an intermediate iteration. For this iteration, the gun solenoid and horizontal steerer were off but the vertical steerer was switched to +3.7 A. There is clearly quite some movement of the beam, specially in the x direction, indicating significant misalignment of the laser in x direction.

The results of the final iterations are shown in figure 5.14 and the laser on the virtual cathode is shown in figure 5.15. In between the multiple iterations for this measurement, the Mo cathode was replaced by the Cs_2Te cathode. The laser group significantly improved the laser beam profile. The colleagues

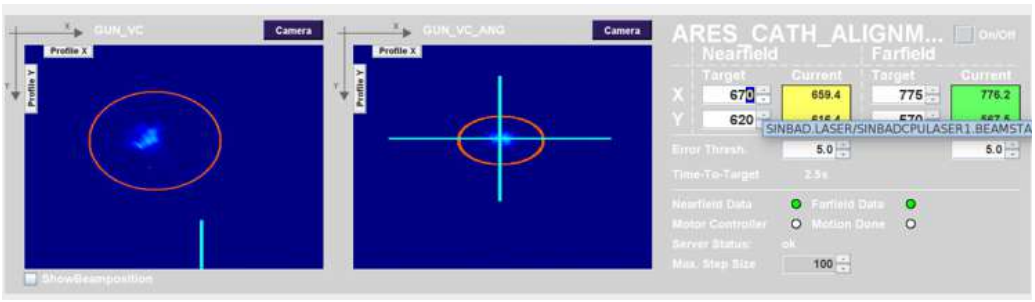

Figure 5.11.: Laser beam on the virtual cathode. Image of the laser auto alignment tool captured before starting the alignment of the photocathode laser.

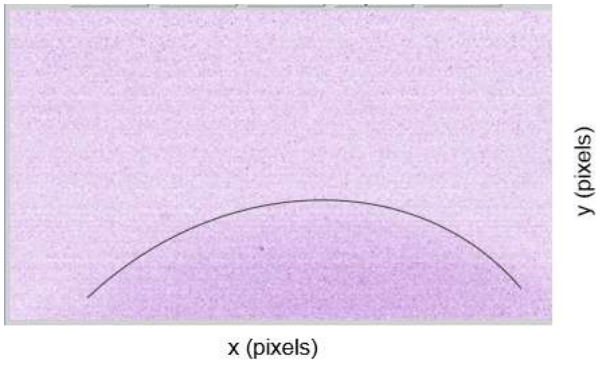

Figure 5.12.: The electron beam lies on the lower side of the field of view of the screen X1 without the use of horizontal and vertical steerer and the gun solenoid before the laser is aligned.

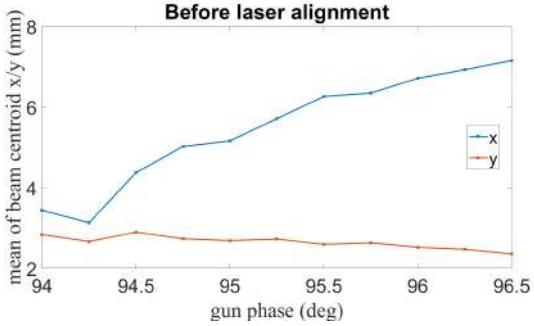

Figure 5.13.: Beam position on the screen X1 as a function of the gun phase. A variation of 4 mm for the beam centroids in x and 0.47 mm in y direction, indicated by the blue and the orange curve respectively, is observed corresponding to a gun phase variation of 2 deg. The gun phase scan range corresponds to the values for which the beam is visible on the screen. The horizontal steerer is off. The vertical steerer is at 3.7 A.

from the low level RF group also worked on the calibration of the low level RF system. As a result, the operating phase of the gun was shifted. The Schottky scan at 3.75 MeV/c using the Faraday cup is shown in figure 5.16. Therefore, the scan range of the phases is different in the two measurements shown in 5.13 and figure 5.14.

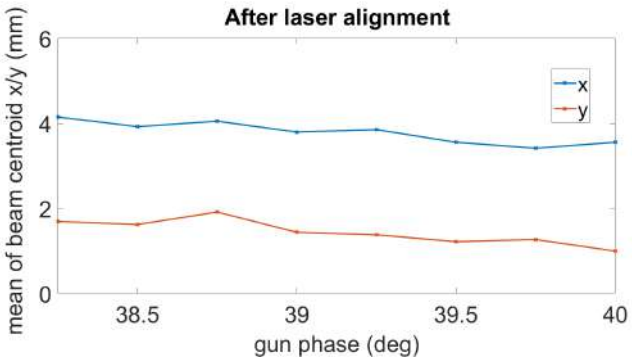

Figure 5.14.: Beam position on the screen X1 as a function of the gun phase. A variation of 0.73 mm for the beam centroids in x and 0.69 mm in y direction, indicated by the blue and the orange curve respectively, is observed corresponding to gun phase variation of 2.5 deg. The gun phase scan range corresponds to the values for which beam is visible on the screen. Both the horizontal and the vertical steerer are switched off.

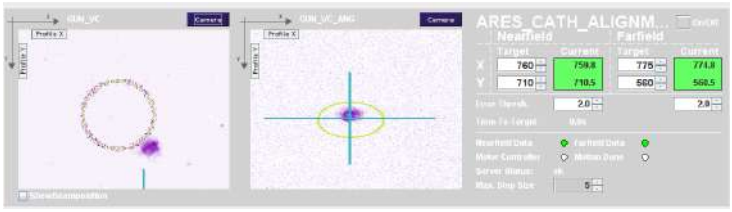

Figure 5.15.: Image of the auto alignment tool panel showing the laser beam centered on the virtual cathode.

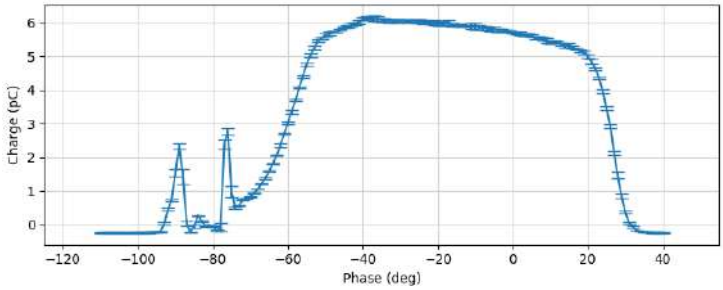

Figure 5.16.: Schottky scan with the Faraday cup after low level RF adjustments. The plot shows the charge as a function of the gun phase.

Conclusion of BBA of laser on the cathode

The laser is well aligned on the cathode, within the achievable accuracy of the stepper motors used to adjust the mirrors of the photocathode laser. A slight movement of the electron beam as a function of the gun phase is still observable on the screen X1 as shown in figure 5.17. One possible reason could be that the earth magnetic field is not fully compensated by the earth magnetic field compensation coils

(EMFC). If we observe the electron beam position on screen R1, which is downstream X1, the beam is quite stable with no significant movement of the electron beam centroids as a function of the gun phase. After the BBA of the photocathode laser, the electron beam and dark charge are fully concentric on R1 as shown in figure 5.17, which is also an indication that the laser beam is well aligned on the cathode.

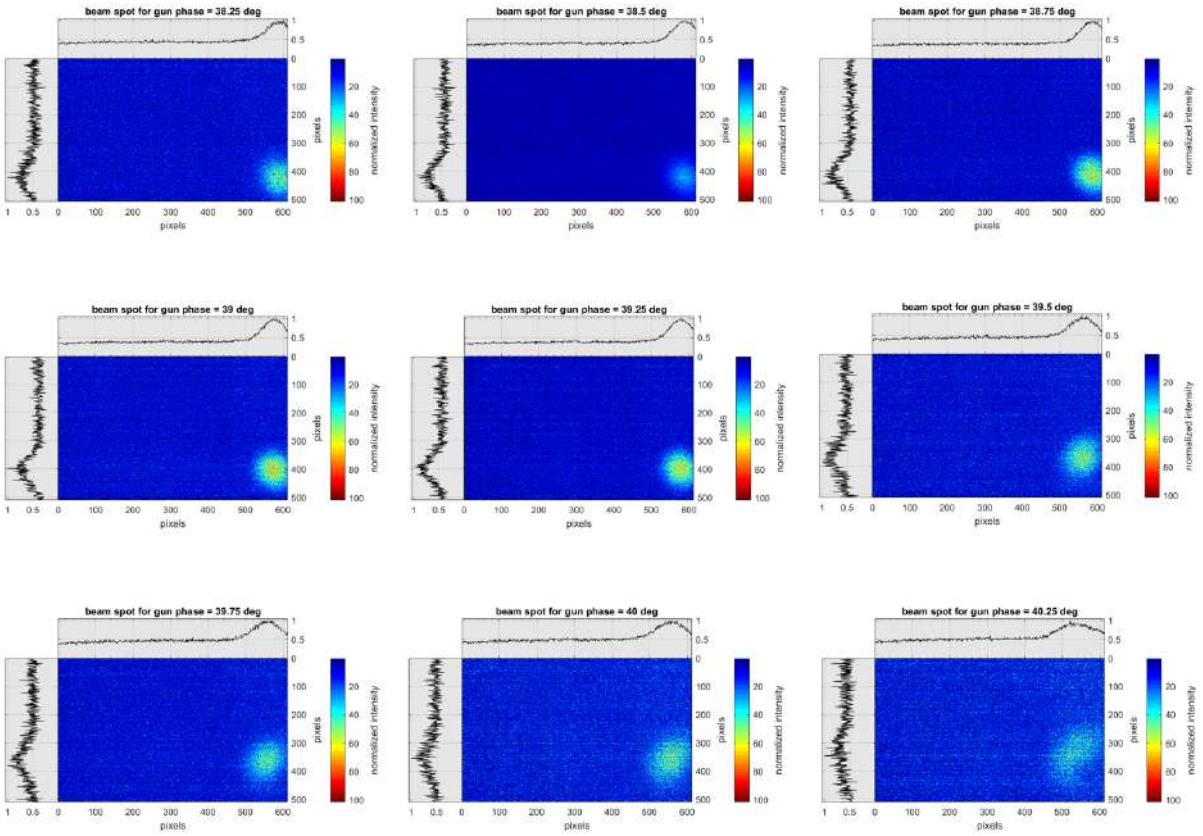

Figure 5.17.: Beam images on screen X1 as a function of the gun phase. The screen shows the beam images in the $x - y$ plane. The gun phase is varied from 38.25 deg to 40.25 deg.

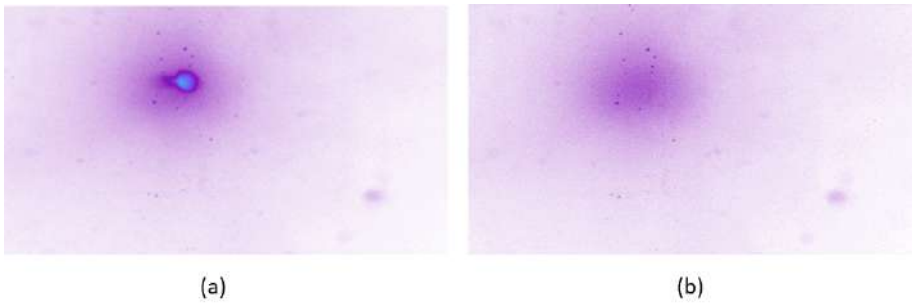

Figure 5.18.: Comparison of electron beam and dark charge on screen R1. (a) both electron beam and dark charge overlapping with each other (b) only dark charge while the laser beam is switched off.

5.5. BBA after the ARES gun upgrade

The ARES gun was exchanged with the new RF coupler design. During the installation process together with the insertion of a new cathode, the solenoid alignment was naturally disturbed. The gun was conditioned up to 5.1 MW with 5 μs long pulses as shown in figure 5.19. There is a significant amount of dark charge recorded with the new gun. The dark charge with the new gun on screen X1 is shown in figure 5.20 and in comparison, the beam on X1 is shown in figure 5.21.

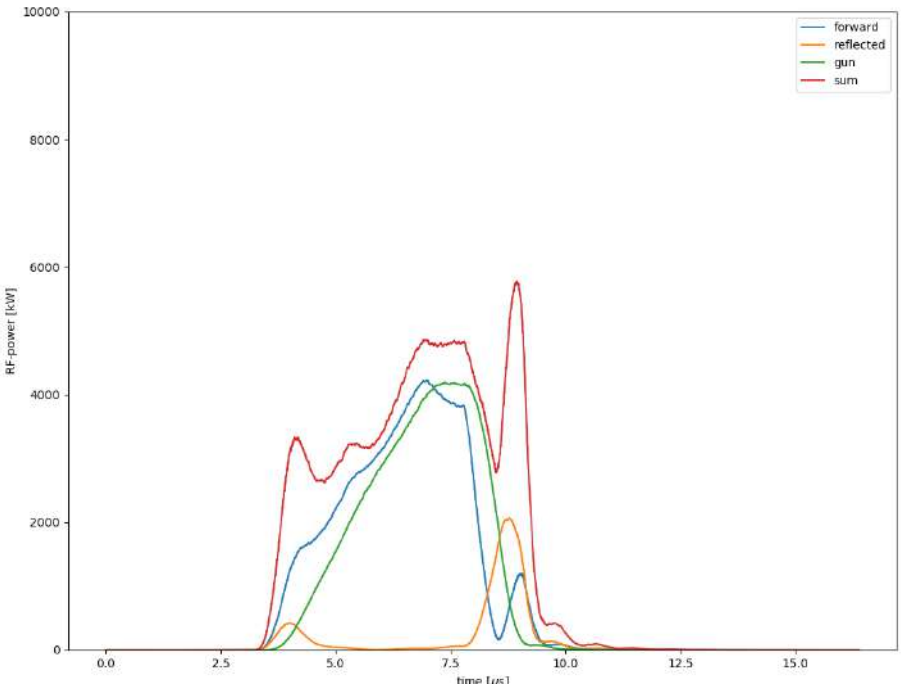

Figure 5.19.: Power spectrum in the ARES new gun.

Since the previous alignment for the gun solenoid was lost due to the gun exchange and associated work in the tunnel, the BBA of the gun solenoid was again started from the beginning. The measurements for the new gun are discussed in the following sections. The same procedure was adopted for the measurement as explained in section 5.3.

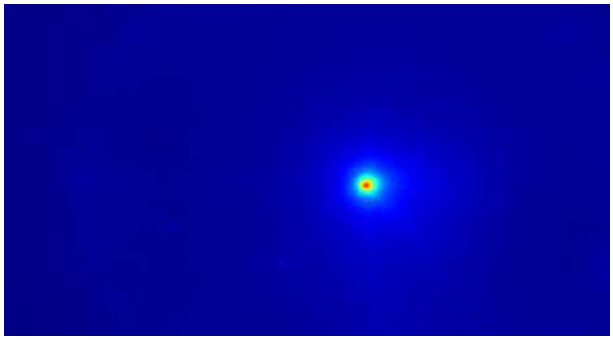

Figure 5.20.: Dark Charge on X1 with the ARES new gun.

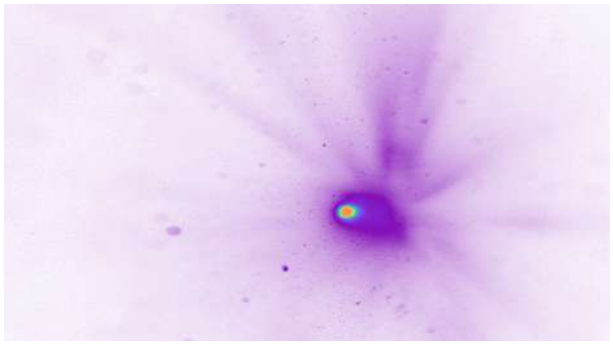

Figure 5.21.: Beam on X1 with the ARES new gun.

Multiple data sets were taken to ensure repeatability of the results. The beam positions were recorded for two power levels, i.e. 3.08 MW and 2.12 MW. For each power level, the momentum was measured using the spectrometer dipole as well as the vertical steerer since the scripts for momentum measurement too were under development. A minor disagreement of 4% was observed in the momentum values measured with the spectrometer dipole and the steerer. Since the calculated misalignment is momentum dependent, all data sets were analyzed using both momentum values to observe the effects of a small error in the momentum values. The analysis of the data taken for this iteration is shown in table 5.4. The error calculation on the measured data is explained in section 4.4. This was the very first momentum measurement from ARES with the newly developed tool. Since the momentum measurement tool for both steerer and dipole have been fully developed and debugged afterwards, this difference of 4% in momentum does not exist for further iterations. Nevertheless, the observed difference helps in determining the sensitivity of the BBA measurement to the momentum measurement.

Table 5.4.: Misalignment calculated from the BBA tool for the first iteration. Measurement data taken on 30.07.2020.

Power (MW)	Momentum (MeV/c)	Δx (mm)	Δy (mm)
3.075	3.534±0.059	2.014 ±0.166	-1.412±0.166
	3.648±0.008	2.192±0.179	-1.517±0.179
2.12	3.094±0.030	1.992±0.155	-1.161±0.155
	2.974±0.038	1.790±0.141	-1.063±0.141

It can be concluded that the determination of the misalignment of the gun solenoid is highly sensitive to the momentum measurement. A difference of 0.150 MeV/c (on average) can give a variation of $\sim 200\mu m$ (on average) in determining the misalignment of the solenoid. It should be noted that during this measurement, it was not possible to align the laser on the photocathode. The laser beam had multiple hotspots and since a Mo cathode was in use at this point implying 1-1.5 pC of charge being emitted from the cathode. This prevented to use the collimator for beam shaping which hinders the alignment of the photocathode laser. However, we proceeded with the first iteration to have a better aligned trajectory despite the photocathode laser still being misaligned.

For the first iteration with the new gun, the solenoid was moved by +1 mm in x direction instead of +2 mm. This decision was based on the fact that there is still a contribution from the laser being misaligned. This iteration was successful with the beam resulting towards the center of the screen without the use of the horizontal and vertical steerer. The comparison of the beam position on screen X1 before and after the first iteration is shown in figure 5.22. A clear improvement in the beam positioning can be observed. Optimization of the beam trajectory can also be seen on screen R1, at the entrance of TWS1. Figure 5.23 shows the focused beam on R1 before and after the first iteration. Before the alignment of the gun solenoid, the beam was visible on the screen only with the use of maximum horizontal steering. The magnet settings for this position were as follows. CHG1 = 5 A, CVG1 = -1.4 A, CHG2 = -5 A and CVG2 = -5 A. After the alignment of the gun solenoid, the beam was centered on the screen without the use of any steering magnets. This is another indication that the solenoid is much better aligned with respect to the beam axis compared to the beam position before the first iteration.

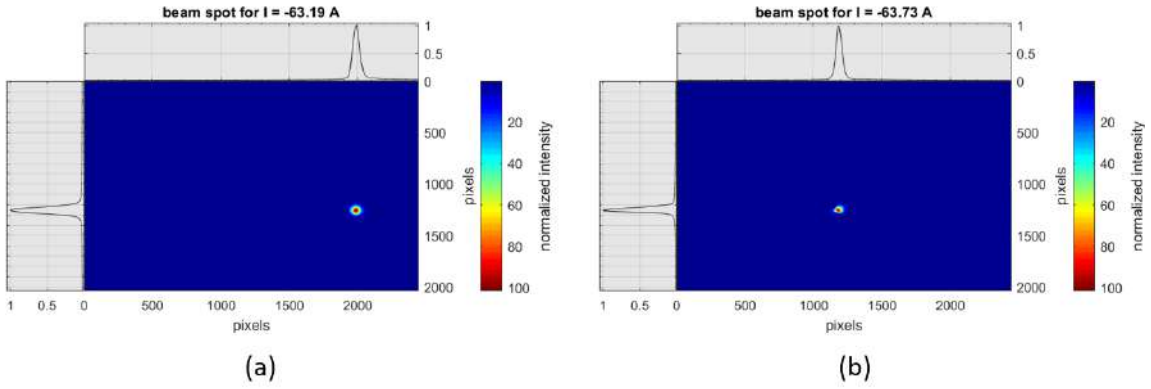

Figure 5.22.: Comparison of the beam on screen X1 (a) before and (b) after the 1st iteration of solenoid alignment.

A new Mo cathode was inserted after this iteration. Two attempts to align the laser were performed. However, the laser could not be aligned at this point in time because a precise movement of the laser optics to align the laser remotely was not possible. The tool for aligning the laser was still under development, to adjust the mirrors remotely, in order to align the photocathode laser within an acceptable range.

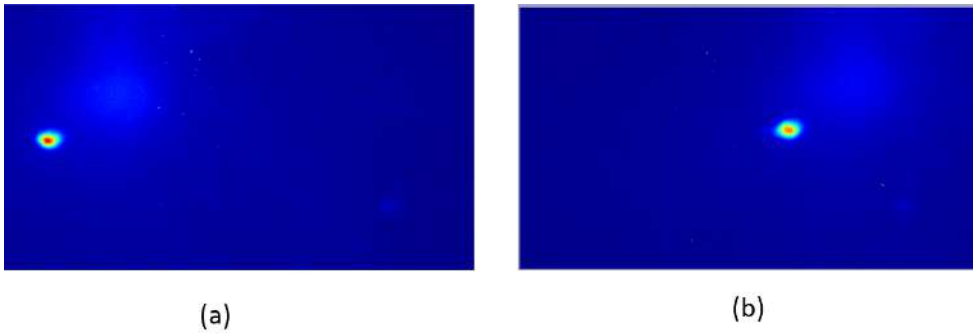

Figure 5.23.: Comparison of the beam on screen R1, at the entrance of the first TWS, before and after the 1st iteration. (a) Beam before the solenoid is aligned with horizontal steering. It was not possible to see the beam without steerer magnets. (b) Beam on R1 after alignment without the use of steerer magnets.

Meanwhile replacement of the screen X1 delayed the second iteration as it could not be utilized for acquiring the measurement data. Once the screen was replaced, the misalignment of the solenoid was measured again for a second iteration in the gun region. The results of the second iteration are shown in table 5.5. The measurement was done at 3 different bunch charges: 1, 3 and 5 pC to observe the influence of space charge. The solenoid current was scanned from -62 A to -59 A in steps of 0.1 A. It can be safely said that up to 10 pC, the bunch charge does not play a very significant role in determining the misalignment of the gun solenoid.

Table 5.5.: Misalignment calculated from the BBA tool for the second iteration. The data taken on 18.11.2020

Momentum (MeV/c)	Charge (pC)	Δx (mm)	Δy (mm)
3.452±0.046	1	-1.687±0.147	0.638±0.147
	5	-1.507±0.034	0.862±0.034
	10	-1.482±0.033	0.820±0.033

The misalignment values shown in table 5.5 were introduced in the gun solenoid in ASTRA to reconstruct the measured beam trajectory. The comparison of simulated beam trajectory with measured data shows a good agreement and validates the calculated misalignment numbers as shown in figure 5.24. The dashed rectangular area in figure 5.24 is the field of view on the screen X1: ±4.35 mm in x and ±2.57 mm in y. The ASTRA simulation data is plotted for the full current range of the gun solenoid (from minimum to maximum) and also for the measured range, i.e. from -62 A to -59 A. This comparison also helps in determining the coordinates of the screen X1 since from figure 5.24, it can be observed that the measured data lies on the ASTRA scan but does not overlap with the measured current range simulated in ASTRA implying that the center of the ASTRA simulation does not correspond to the center of the screen. The BBA measurement result and its comparison with the ASTRA simulations determines the screen coordinates and indicates that the camera optics needs to be adjusted for an aligned solenoid to observe the beam at the center of screen.

After the laser was aligned on the cathode, the measurement was repeated for the solenoid alignment.

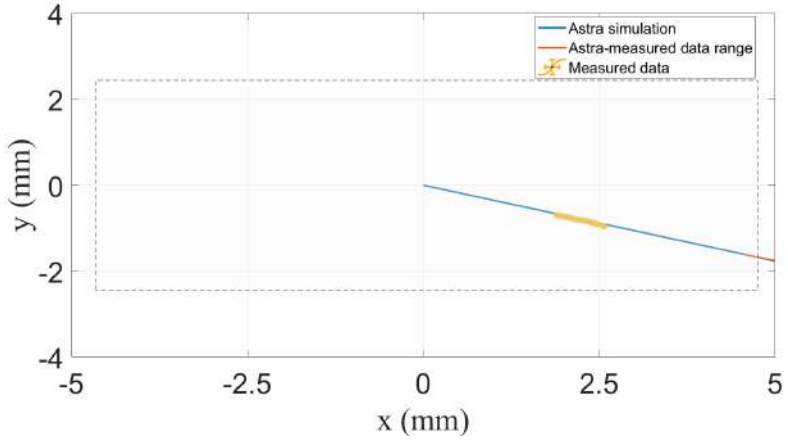

Figure 5.24.: Comparison of measured data with ASTRA simulations. The dashed rectangular area is the field of view on the screen. The blue line shows the ASTRA simulation result for the full current range of the gun solenoid. The red line corresponds to the ASTRA simulation result over the current range corresponding to the measured data, i.e. from -62 A to -59 A.

The solenoid current was scanned from -70 to -68 A in steps of 0.2 A for a momentum of 3.875 MeV/c. Two sets of data were taken to test the reproducibility of the results. Table 5.6 gives the calculated misalignment of the solenoid. The analysis of this measurement shows that the solenoid is almost aligned in y but misaligned in x by an amount of $\sim$-1.5 mm.

Table 5.6.: Misalignment calculated from the BBA tool for the second iteration taken again after the laser was aligned. Data taken on 26.11.2020.

Momentum (MeV/c)	Δx (mm)	Δy (mm)
3.875±0.000	-1.486±0.152	0.158±0.152
	-1.562±0.115	0.151±0.115

The comparison of the misalignment with the ASTRA simulations is shown in figure 5.26. The misalignment obtained from the measurement data in table 5.6 is introduced into the gun solenoid in ASTRA and the beam position on the screen is compared with the measurement data. The ASTRA simulation data is plotted for the full current range of the gun solenoid and also for the current range corresponding to the measured data, i.e. from -70 A to -68 A. The comparison of the simulated and the measured beam trajectory in figure 5.26 again indicates that the camera optics needs to be adjusted for an aligned solenoid to observe the beam at the center of the screen.

The second iteration was applied by moving the gun solenoid by -1 mm in x instead of moving by -1.5 mm. The reason was purely to avoid the beam moving out of the field of view of the screen as predicted by simulations in Astra. This was expected from ASTRA since the center in ASTRA does not correspond to the camera, which is not looking at the center of the screen. The beam ended up at the edge of the screen as shown in figure 5.27.

The field of view of the camera optics was adjusted to see the beam completely on the screen center. The measurement was repeated after the field of view adjustment and the calculated misalignment values

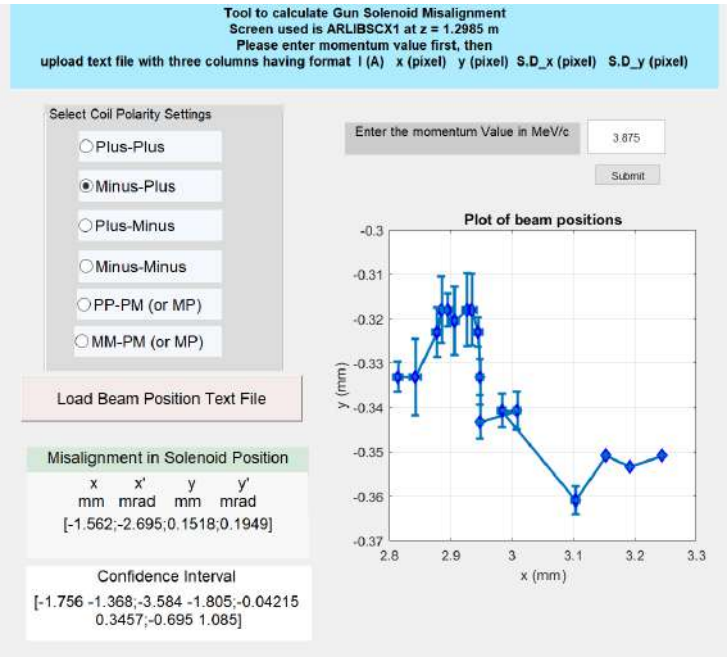

Figure 5.25.: Image of the analysis tool to determine the misalignment of the gun solenoid for the measurement data taken on 26.11.2020.

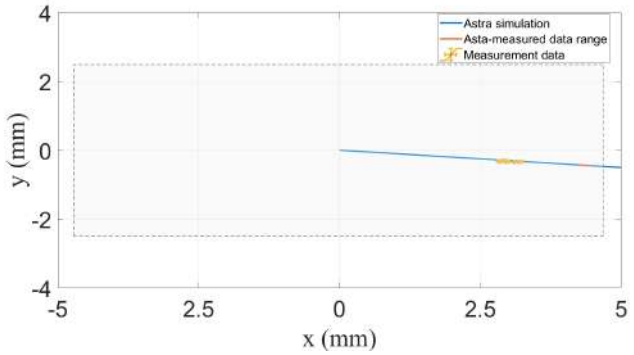

Figure 5.26.: The calculated misalignment from table 5.6 is applied to the gun solenoid in ASTRA and the simulated beam trajectory is compared with the measured data. The ASTRA simulation shows good agreement with the measurement data. The dashed rectangular area is the field of view on the screen X1: ± 4.35 mm in x and ± 2.57 mm in y.

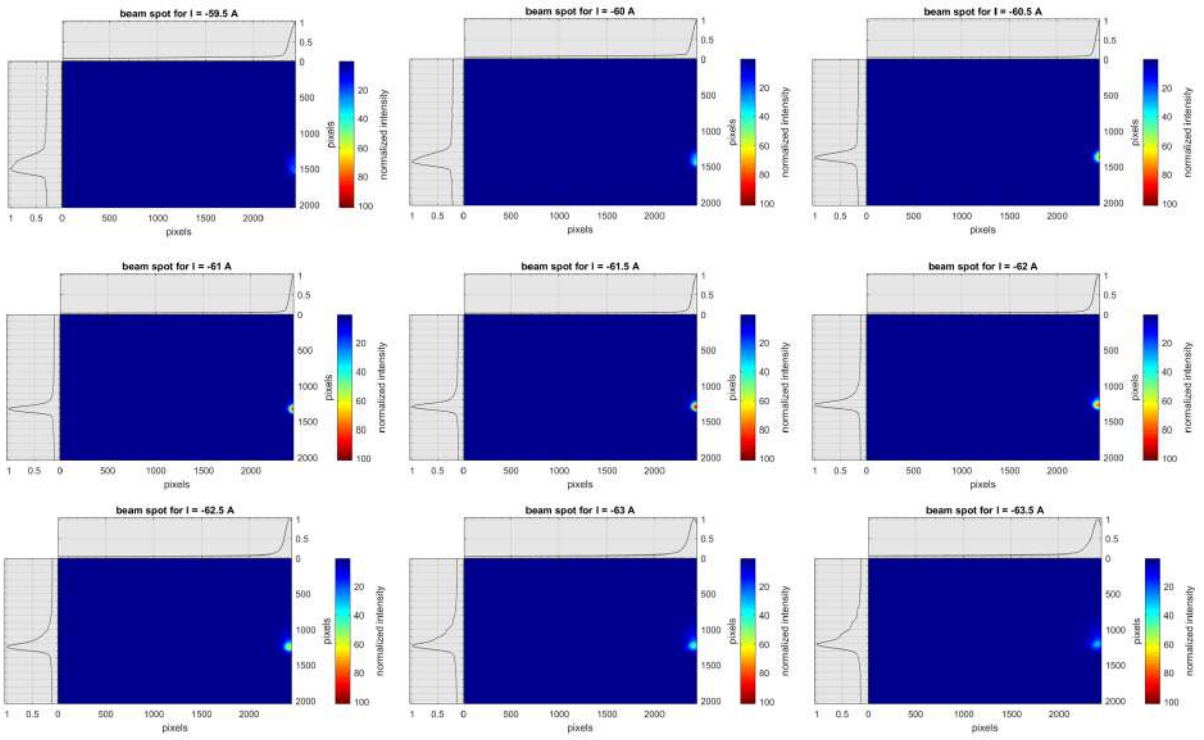

Figure 5.27.: Beam on screen X1 for a scan of the solenoid current from -59.5 A to -63.5 A after the second iteration. The beam lies on the edge of screen as predicted by ASTRA simulations shown in figure 5.26.

are shown in table 5.7. The measurements were done at a gun gradient of 70 MV/m. The solenoid current was scanned from -68 to -58 A. The beam position on screen X1 as a function of the solenoid current is shown in figure 5.28.

Table 5.7.: Misalignment calculated from the BBA tool for the third iteration of the gun solenoid. Data taken on 14.04.2021.

Momentum (MeV/c)	Δx (mm)	Δy (mm)
3.5642±0.0005	-0.582±0.022	-0.414±0.022

The solenoid is well aligned in x, with some margin of improvement, since a correction of -1 mm instead of -1.5 mm has been applied. The misalignment in y has slightly worsened. The calculated misalignment numbers were compared with ASTRA simulations and the beam position on the screen is compared with the measurement data as shown in figure 5.29. The misalignment values calculated in table 5.7 are applied to the gun solenoid in ASTRA and the simulated beam trajectory is compared with the measured data as a function of the gun solenoid current. The beam trajectory corresponding to the measured current range, i.e. -68 A to -58 A, shows that the camera optics is better aligned with the screen center but still requires some adjustments. The ASTRA simulations show fair agreement with the measurement data. Calculating the misalignment and its comparison with ASTRA simulations also helps in determining the screen coordinates as the measured data center and simulated screen center from ASTRA are much closer

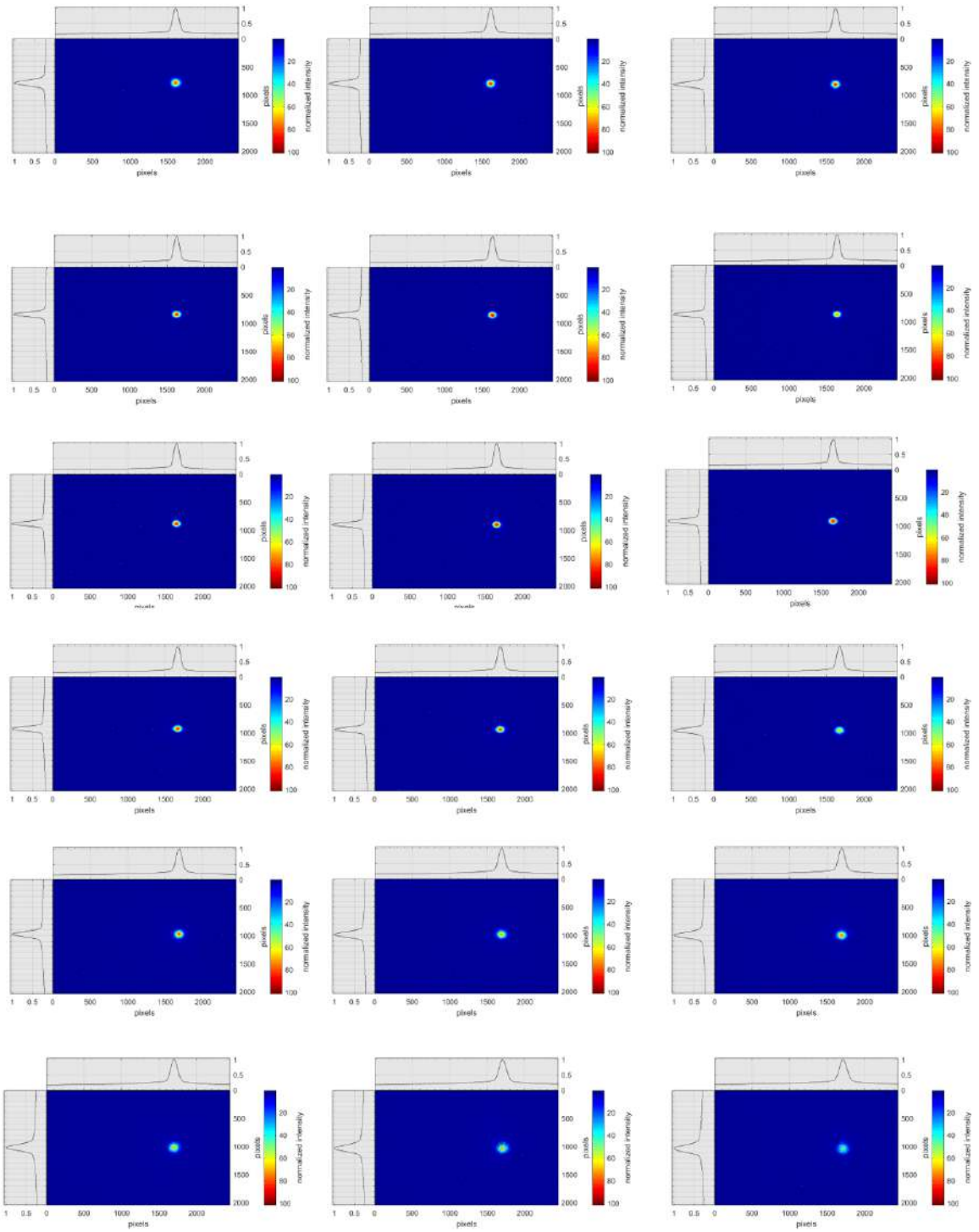

Figure 5.28.: Beam on screen X1 for a scan of the solenoid current from -68 A to -58 A after the second iteration.

to each other after changing the field of view of the screen.

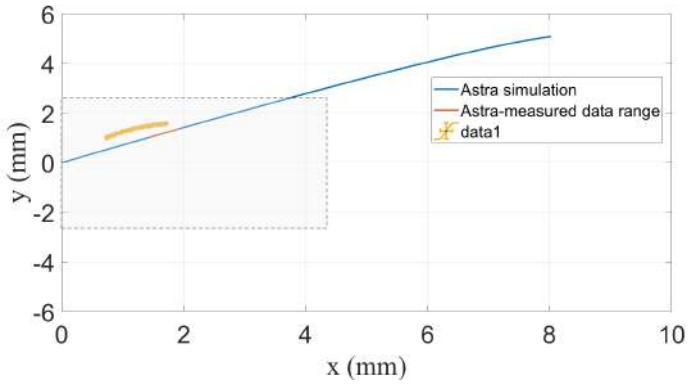

Figure 5.29.: The misalignment calculated in table 5.7 is applied to the gun solenoid in ASTRA and the simulated beam trajectory is compared with the measured data as a function of the gun solenoid current. Comparison of the measurement data with ASTRA simulations shows fair agreement. The dashed rectangular area is the field of view on the screen. Only half of the field of view on the screen is shown for zooming in on the measurement data.

This iteration of the gun solenoid alignment was followed by the shutdown of ARES for the bunch compressor (BC) installation. In addition the transverse deflecting structure polarix TDS will also be installed for the bunch length measurement and beam characterization studies at ARES [48]. After the long shutdown ARES will come up as a new machine with new diagnostics added, screen stations with a better aligned field of view and the installation of new components. Four BPMs will be installed at ARES. After the shutdown, a final iteration of the gun solenoid is planned to optimize the beam trajectory for the injection into the BC. With the present alignment, the beam has a reasonable straight trajectory till the end of the linac without an excessive use of horizontal and vertical steerers. The final solenoid alignment measurement after the shutdown is shown in table 5.8 which shows a well aligned solenoid with the best possible accuracy achievable with the manual system. Figure 5.30 gives the comparison of offsets in beam centroids as a function of solenoid current before and after the BBA. The BBA of the gun solenoid at ARES resulted in a well aligned stable beam as a function of solenoid current. The comparison of measurement results with ASTRA simulations validates the proposed algorithm based on a linear transfer matrix base formalism.

Table 5.8.: Misalignment calculated from the BBA tool for the final measurement of the gun solenoid. Data taken on 24.09.2021.

Momentum (MeV/c)	Δx (mm)	Δy (mm)
3.5642±0.0005	-0.287±0.041	-0.140±0.041

It was observed for every iteration that the movement of solenoid in x affected the misalignment in y. Ideally, this should not be the case as the mover system in x and y direction are independent of each other. The movement of the solenoid in other direction could be caused by many possible reasons, e.g parasitic coupling between x and y in the positioning system, a tilted base plate of the solenoid

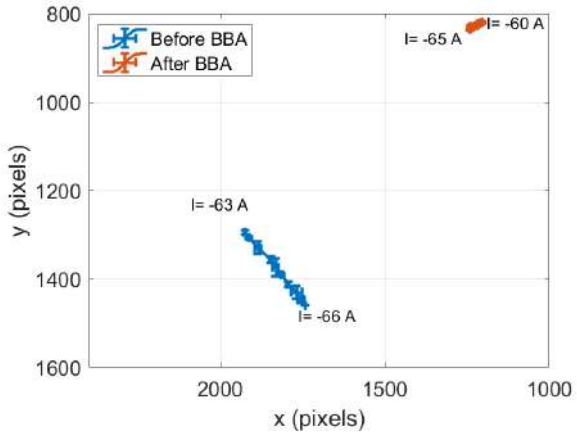

Figure 5.30.: Beam trajectory on screen X1 as a function of the gun solenoid current before and after the BBA. The beam is stable on screen X1 as a function of solenoid current, a signature of an aligned solenoid.

or an angle between the solenoid reference position and the screen reference. In figure 5.31, change in the misalignment direction is plotted as a function of the applied misalignment in x. -1.5 mm is the misalignment in x after the laser was aligned. This is assigned zero applied misalignment in figure 5.31. It is observed that the $\Delta x'$ and $\Delta y'$ are more drastically changing when a correction in the solenoid position is applied. This implies an angular tilt is inherent in the lattice and explains the change observed in Δy as evident from equation 4.14.

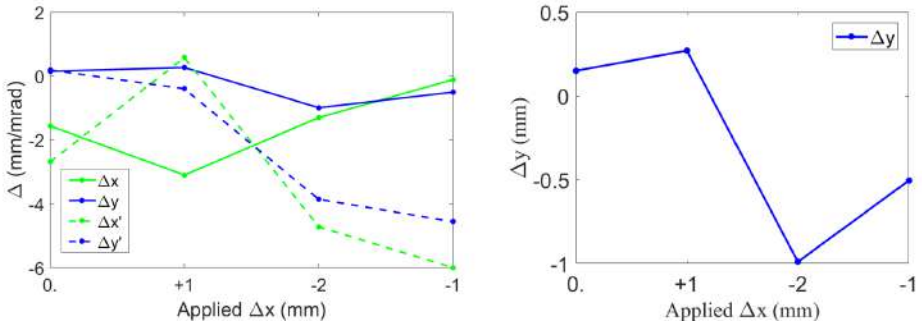

Figure 5.31.: Plot of calculated misalignment of gun solenoid after each iteration. For each iteration of misalignment of gun solenoid corrected in x, the misalignment in y is also changed. $\Delta x'$ and $\Delta y'$ are more drastically changing when a correction in the solenoid position is applied. This implies an angular tilt is inherent in the lattice and explains the change observed in Δy.

5.6. Effects of earth magnetic field compensation coil on beam trajectory

At ARES, an earth magnetic field compensation (EMFC) coil is installed to compensate for the impact of the earth magnetic field on the beam trajectory. The EMFC coil is installed upto the end of first TWS. The nominal operating current for the EMFC coil at ARES is -8 A for both the horizontal and the vertical

coil. The gun solenoid and laser alignment assumes that the earth magnetic field is fully compensated. However in reality, this may not be the case at every point along the beam line. Moreover, the gun solenoid alignment measurements were done at different beam momentum. The EMFC coil can affect the beam trajectory, since the beam might experience a kick because of a different beam momentum. Therefore to study the impact of the EMFC coil on the beam trajectory, a measurement was performed via a 2D scan. The horizontal and vertical EMFC coils were scanned over the operating current range of [-10,10] A. At each operating value of the EMFC coil, the gun solenoid was scanned and the beam position measured on screen X1. The measurement was performed at a gun gradient of 56.8 MV/m corresponding to a beam momentum of 3 MeV/c. The beam was focused at -53.5 A. The 2D plots of the measurement are shown in figure 5.32. In figures 5.33 and 5.34, for horizontal and vertical coil respectively, plots shows the beam deflection observed over the operating range of the EMFC coil at the solenoid and at the screen. Knowing the longitudinal positions of the solenoid and the screen, the beam position at the solenoid location was calculated by extrapolation using simple trigonometry.

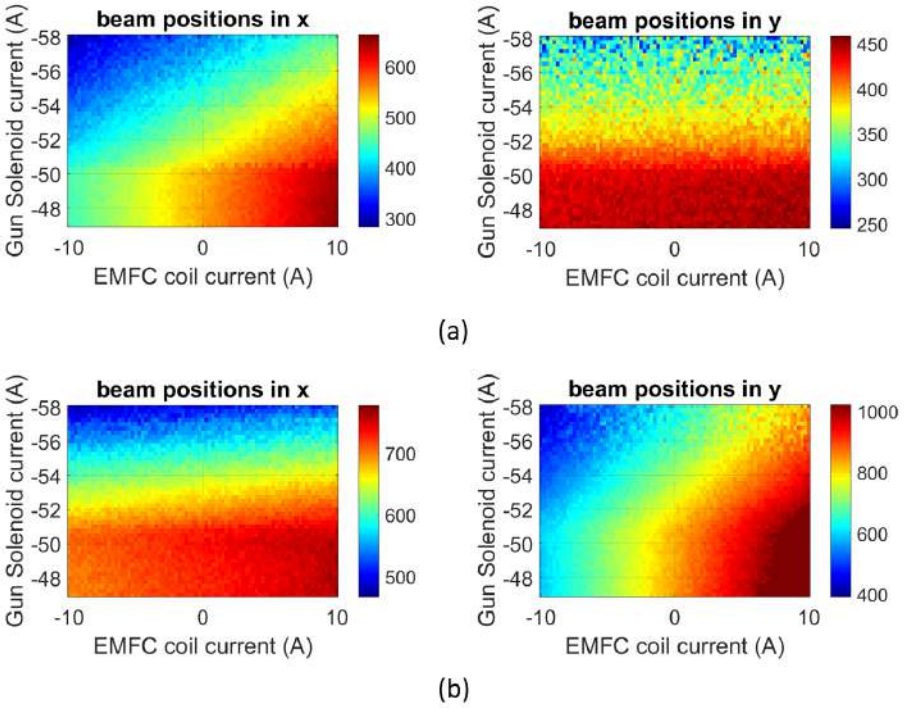

Figure 5.32.: Beam position on screen X1 for EMFC coil vs. gun solenoid current at 3 MeV/c (a) EMFC horizontal coil scanned. Vertical coil at design value of -8 A (b) EMFC vertical coil scanned. Horizontal coil at design value of -8 A.

The measurement shows that, for a fixed momentum, the EMFC coils cause a small deflection of the beam trajectory over the full current range. The measurement was repeated at gun gradient of 70 MV/m which is the nominal operating value corresponding to a momentum of 3.63 MeV/c. The beam was focused at -64.5 A. The corresponding results are shown in figures 5.35, 5.36 and 5.37 respectively.

To correlate the impact of the EMFC coils on the solenoid misalignment calculation, the beam centroids

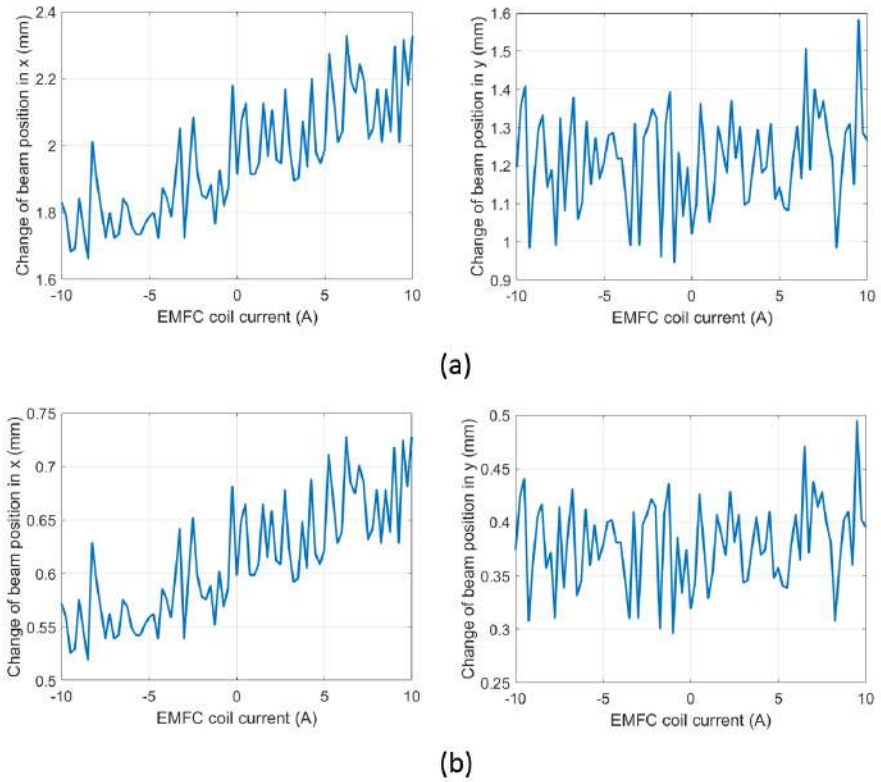

Figure 5.33.: Beam deflection as a function of the EMFC horizontal coil current. Vertical coil at design value of -8 A (a) at screen position (b) at solenoid position.

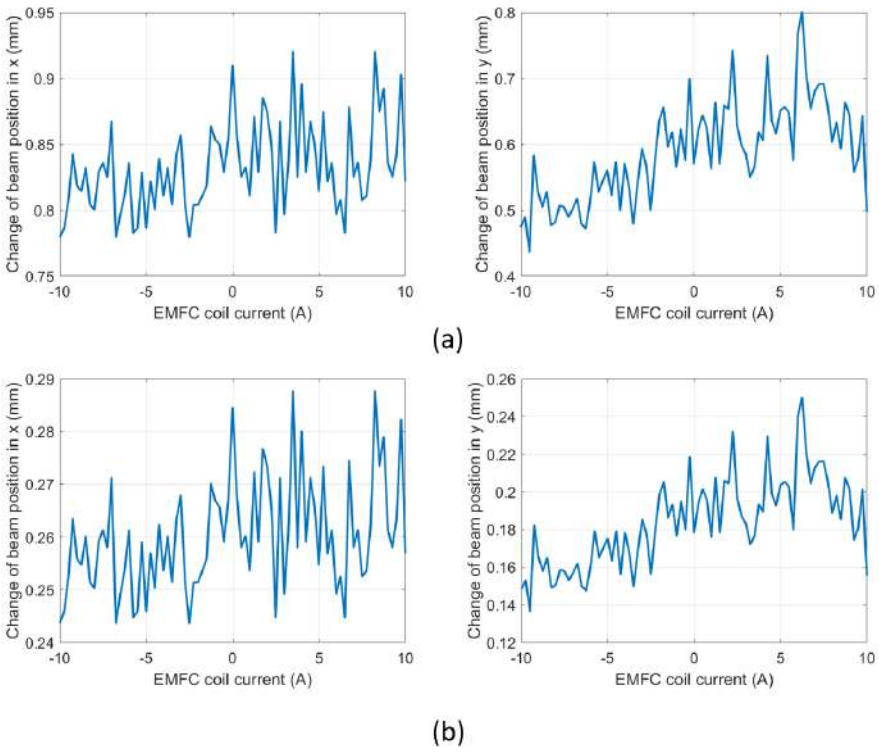

Figure 5.34.: Beam deflection as a function of the EMFC vertical coil current. Horizontal coil at design value of -8 A (a) at screen position (b) at solenoid position.

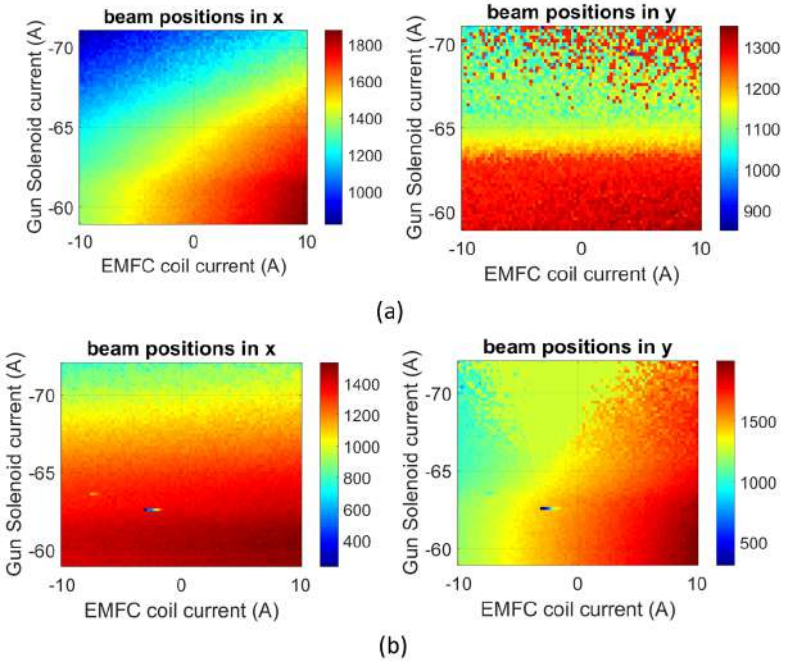

Figure 5.35.: Beam position on screen X1 for EMFC coil vs. gun solenoid current at 3.63 MeV/c (a) EMFC horizontal coil scanned. Vertical coil at design value of -8 A (b) EMFC vertical coil scanned. Horizontal coil at design value of -8 A. An event during the measurement occurred for (b) containing spurious data points corresponding to either vacuum activity causing RF in the gun to be shortly ramped down or the fluctuations of the camera servers for recording the beam data.

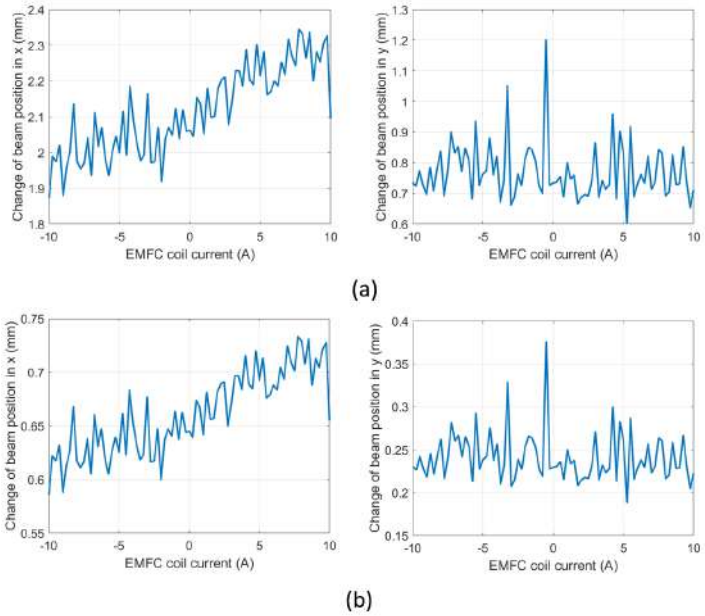

Figure 5.36.: Beam deflection as a function of the EMFC horizontal coil current. Vertical coil at design value of -8 A (a) at screen position (b) at solenoid position.

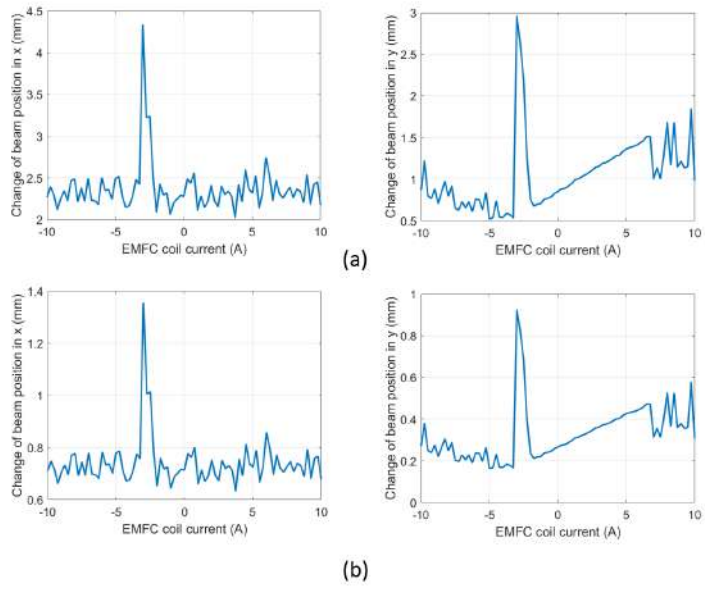

Figure 5.37.: Beam deflection as a function of the EMFC vertical coil current. Horizontal coil at design value of -8 A (a) at screen position (b) at solenoid position. The peaks correspond to the spurious data points as observed in figure 5.32 (b).

data from figures 5.32 and 5.35 was used to calculate the misalignment of the gun solenoid. This was done over the EMFC coil operating range of [-10, 10]A. Figure 5.38 shows the misalignment of the gun solenoid calculated at two different momentum values for varying EMFC currents. The blue line represents the misalignment at a gun gradient of 70 MV/m and the green line for 56.8 MV/m. The solid line shows the misalignment in x and the dashed line in y direction. From figure 5.38, it can be concluded that the misalignment for a particular momentum has a weak dependence on the EMFC coil current. This is within the $100\mu m$ accuracy range achievable with the mechanical mover system. However, the misalignment numbers do depend on the momentum value. The results for 3 MeV/c and for 3.63 MeV/c differ. Hence all iterations of BBA should be performed at the nominal operating gradient of 70 MV/m to have consistent results.

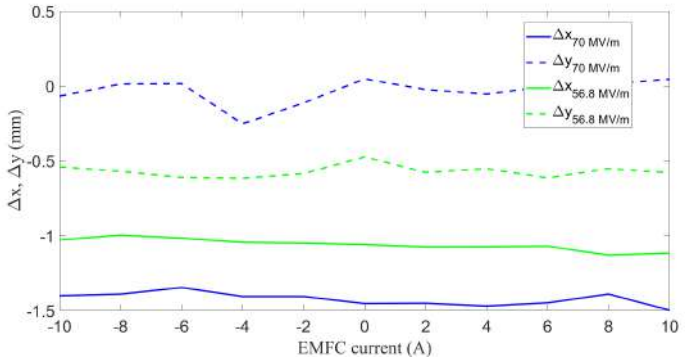

Figure 5.38.: Misalignment of the gun solenoid calculated at two different momentum values for varying EMFC current. The beam centroid data from figures 5.32 and 5.35 is used to calculate the misalignment. The blue line represents the misalignment at a gun gradient of 70 MV/m and the green line at 56.8 MV/m. The solid and dashed line represent misalignment in x and y direction respectively.

5.7. BBA of solenoids around TWS

The measurement data for the BBA of solenoids around the TWS was acquired during ARES beam times. The measurement was started with the fourth solenoid of TWS1. The TWS1 was powered off during these measurements to avoid the focusing effects of RF fields on the beam trajectory. The gun solenoid and the horizontal and vertical steerers were used to find the straight trajectory (so called "golden orbit") through TWS1. This was achieved by observing the beam position on the screens R1 and R2, i.e. at the entrance and exit of TWS1 with the TWS1 solenoids off. The straight trajectory through the TWS1 ensures that a kick experienced by the beam is caused purely by the solenoid field. The beam spot on screen R1 and R2 is shown in figure 5.39. The gun solenoid was set at -50 A, the horizontal and the vertical steerer at -1.6 A and -0.3 A respectively. The low energy dipole spectrometer and the four solenoids of TWS1 were cycled to zero field values to avoid effects of remnant fields on the beam. The beam on screen R2 is very dispersed, but nevertheless centered, since there was no focusing around TWS1 to transport the beam over a distance of $\sim$7 m (position of R2).

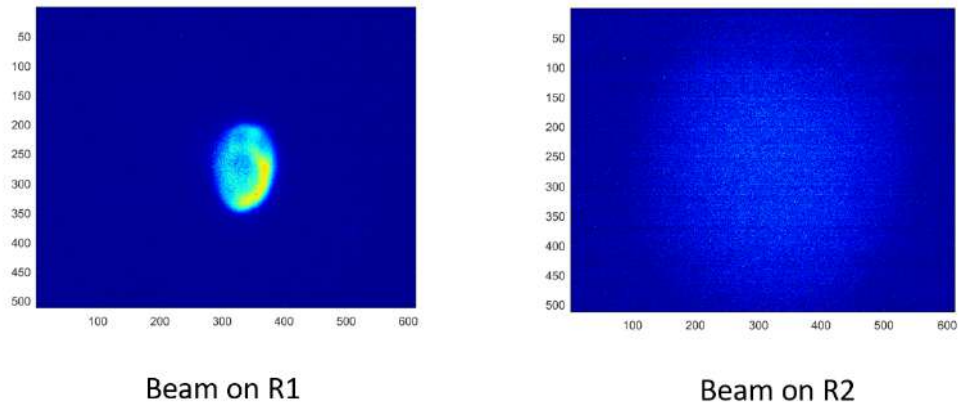

Figure 5.39.: Beam centered on screens R1 and R2 using gun solenoid and horizontal and vertical steerer. Dipole and other solenoids of TWS1 cycled to zero field value.

Once the golden orbit was established, the beam and background images corresponding to the current range of [-48,-38] A for the fourth solenoid of TWS1 (namely SOG4) were recorded. 20 beam and background images were stored for each set point and then averaged. The current range corresponds to the values for which the beam was visible on the screen as shown in figure 5.40. The images were processed to calculate the centroids positions, which were then used by the alignment script as in the case of the gun solenoid explained in section 5.2.2. The measured beam momentum was 3.390 ± 0.045 MeV/c at a gun gradient of 65 MV/m. Table 5.9 gives the calculated misalignment and figure 5.41 shows the image of the Matlab tool panel for one of the measurements.

Table 5.9.: Misalignment calculated from the BBA tool for the fourth solenoid of TWS1. First iteration data taken on 28.10.2020.

Misalignment Direction	Δx (mrad)	Δy **(mm)**
1^{st} measurement	3.155 ± 0.114	4.345 ± 0.114
2^{nd} measurement	3.152 ± 0.116	4.355 ± 0.116

The misalignment calculated from the Matlab tool was verified with ASTRA. The misalignment numbers obtained from the routine were added in an ASTRA simulation and the beam trajectory was compared with the measurement data. Figure 5.42 gives the comparison of ASTRA simulations and the measured data. The blue helical path represents the simulated beam trajectory for the full range of solenoid current up to the maximum value of -130 A. The orange curve shows the measured data which is in good agreement with the ASTRA simulations. In section 4.5, it was discussed that the algorithm has around 6% systematic error. This means that the misalignment is slightly underestimated. In ASTRA, another measurement was simulated with same misalignments as calculated from the measurement data, but adding 6% error in x. This resulted in a perfect agreement with the measurement data and ASTRA as shown in figure 5.43. The dashed rectangle in figure 5.43 represents the field of view of the screen.

The measurement was repeated after the alignment of laser and gun solenoid, by scanning the solenoid

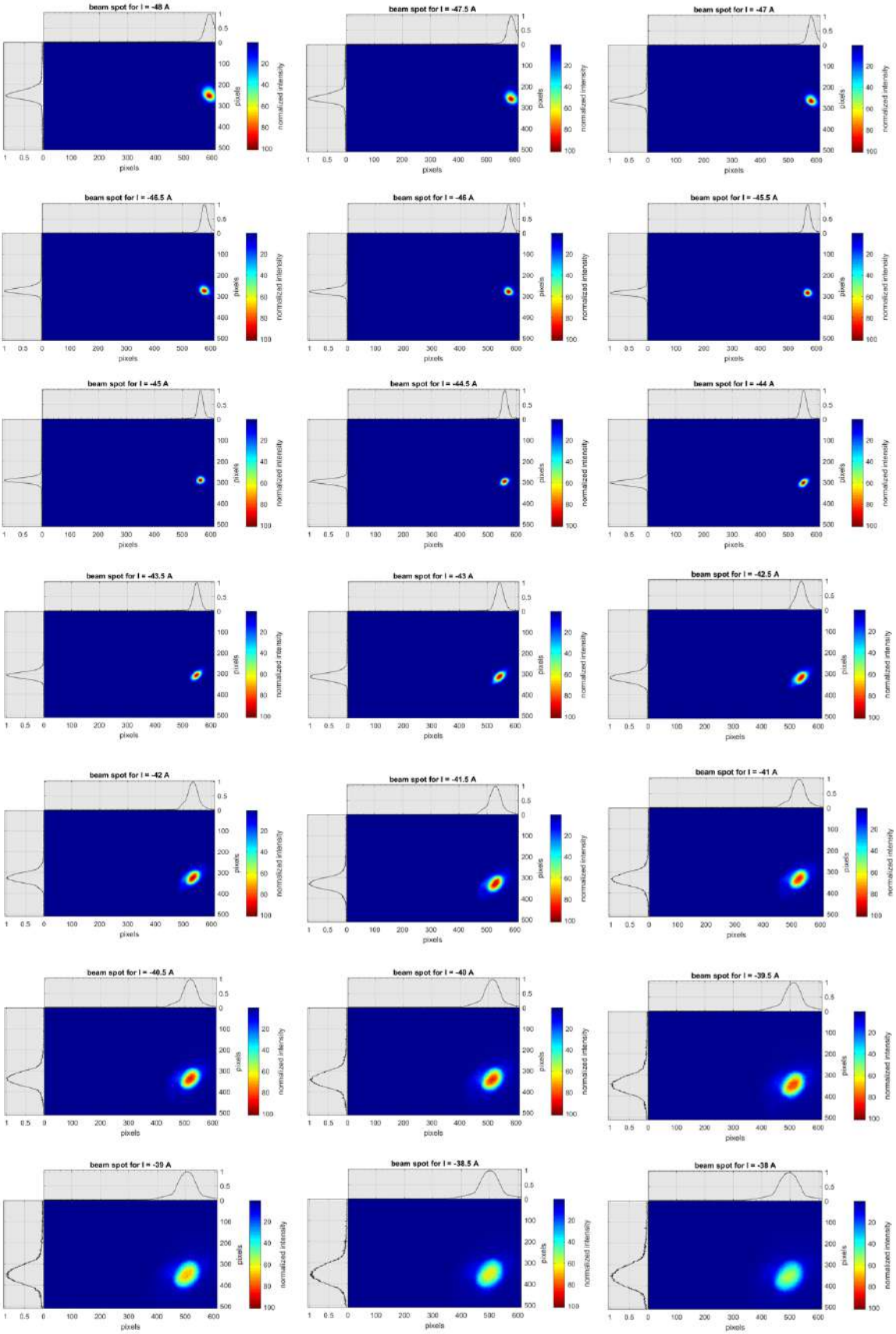

Figure 5.40.: Images of the beam on screen R2 as a function of the current of the fourth solenoid of TWS1.

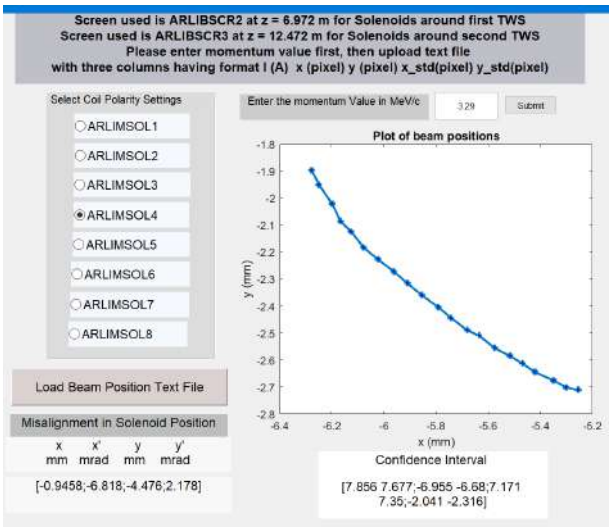

Figure 5.41.: Image of the Matlab tool panel for calculating the misalignment of the fourth solenoid of TWS1.

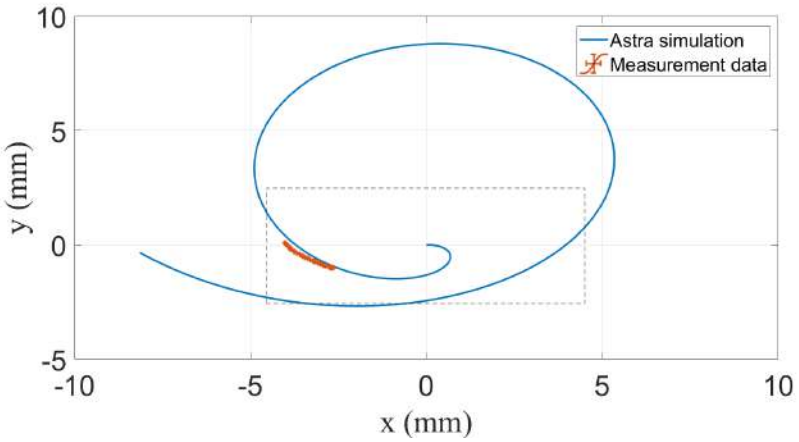

Figure 5.42.: The misalignment values obtained from the routine added in an ASTRA simulation and the beam trajectory were compared with the measurement data. For the measurement data, the current scan range was [-48, -38] A. For ASTRA, the beam trajectory for the full current range [-130, 0] A is plotted. The misalignment of the solenoid is $\Delta x = -3.15$ mm, $\Delta x' = 3.72$ mrad, $\Delta y = -4.34$ mm, and $\Delta y' = 0.67$ mrad. The dashed rectangle represents the field of view of screen R2: $\pm$ 4.35 in x and $\pm$ 2.61 mm in y.

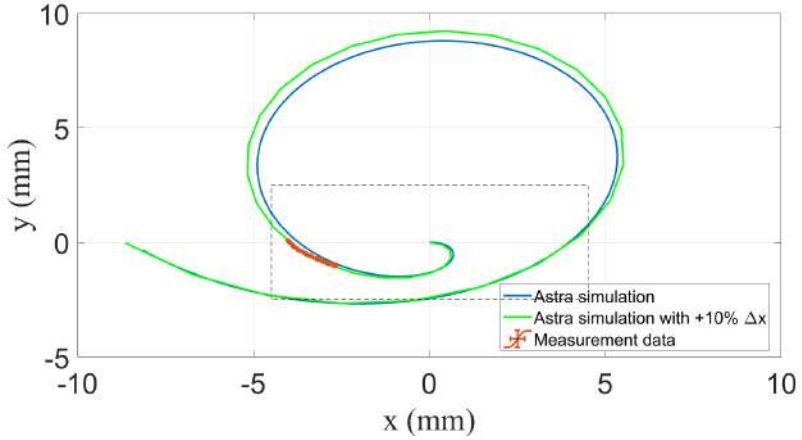

Figure 5.43.: Same misalignment of the solenoid as in figure 5.42 except $\Delta x = -3.4$ mm instead of -3.15 mm.

current from [-48,-36] A at a gun gradient of 70 MV/m corresponding to a beam momentum of 3.5642 ± 0.0005 MeV/c as shown in figure 5.44. The calculated misalignment of TWS1's fourth solenoid, before and after the BBA of gun solenoid, is shown in table 5.10. This resulted in a very stable beam position as a function of the solenoid current, a signature of an aligned solenoid as the beam is travelling on the solenoid axis and not experiencing any kick because of misalignment. The beam stability on screen R2 as a function of the solenoid current is shown in figure 5.46.

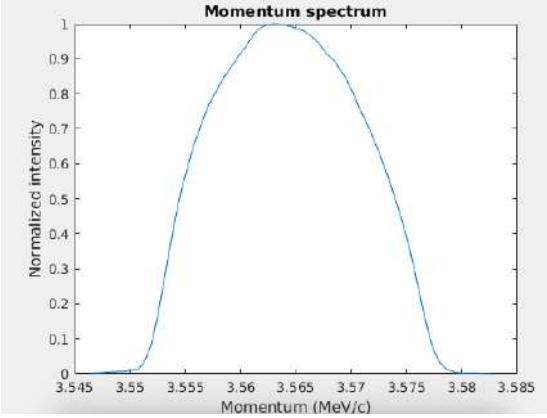

Figure 5.44.: Beam momentum for RF gun at 70 MV/m.

Table 5.10.: Misalignment calculated for the fourth solenoid of TWS1 after the BBA of gun solenoid and laser alignment. Data taken on 07.04.2021.

Momentum (MeV/c)	Δx (mm)	Δy (mm)
3.5640 ± 0.0005	-0.345 ± 0.054	-0.466 ± 0.054

Alternatively, the beam stability on screen R2 as a function of the solenoid current before and after the BBA of gun solenoid is shown in figure 5.46. The fourth solenoid was well aligned according to the measured data represented by orange curve in figure 5.46 as shown by beam offset as a function of

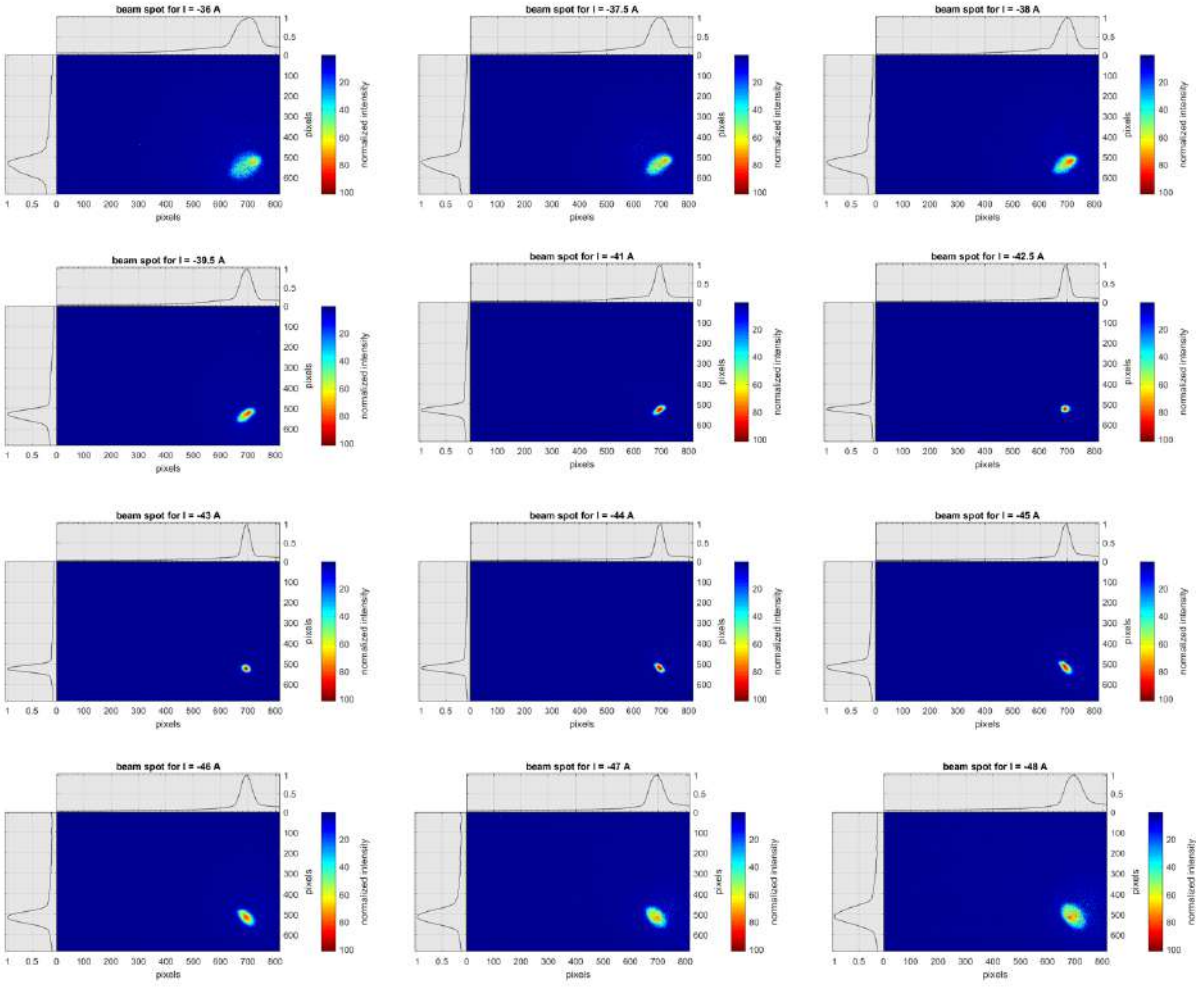

Figure 5.45.: Selected snapshots of beam on screen R2 as a function of the SOL4 solenoid current after the 1st iteration. The beam is stable on screen R2, a signature of an aligned solenoid.

solenoid current. The rest of the three solenoids of first TWS were aligned with respect to the coordinates of fourth solenoid.

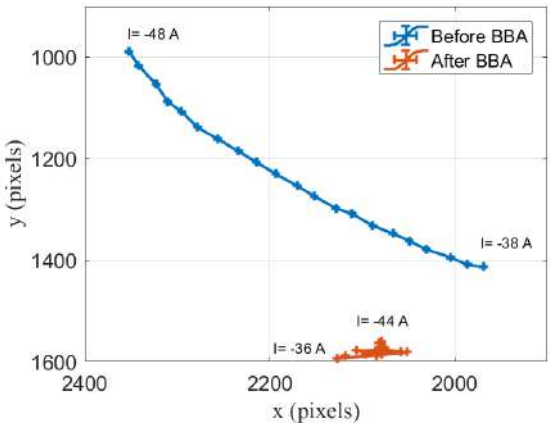

Figure 5.46.: Beam trajectory on screen R2 as a function of the SOL4 current before and after the BBA of gun solenoid. The beam is stable on screen R2, a signature of an aligned solenoid.

Since the SOL4 was well aligned, the rest of the three solenoids, namely SOL1, SOL2 and SOL3, were aligned with respect to the coordinates of SOL4.

The measurement for SOL4 shows that the solenoid was installed 2.6 cm closer to the gun in the longitudinal direction compared to the lattice design values. The longitudinal position corresponds to the center of the solenoid magnet. This implies that the drift length between SOL4 and the screen is 2.6 cm larger. The measured data was reanalyzed with the new drift matrix. The results are shown in table 5.11. A difference of less than 100μ m is observed with the measured longitudinal position of the SOL4. Practically the alignment system has resolution of 100μ m, and the difference cannot be corrected. This was confirmed by ASTRA simulations. In ASTRA, the misalignments calculated in table 5.10 were introduced in the SOL4. Then the longitudinal position of the solenoid was scanned over ± 5 mm with respect to the design value and the beam positions were recorded. The simulated beam positions were fed in the algorithm to calculate back the misalignment. The percentage error in the misalignment calculation with respect to the design longitudinal position z is shown in figure 5.47. The difference in the calculated misalignment for the simulated measurement is less than 1%. Physically, the drift matrix $\begin{pmatrix} 1 & D \\ 0 & 1 \end{pmatrix}$ changes the divergence, where D is the drift length. Since SOL4 is well aligned, the angular misalignment is only 0.77 mrad, hence the error is also small. However, in case of large angular misalignment, the error could be significant. The longitudinal positions of the other three solenoids of TWS1 were also measured and there were found in good agreement with the design values.

The alignment of the solenoids of TWS1 was followed by the long shutdown of ARES for the Bunch Compressor (BC) installation. In addition to BC, first solenoid for the RF gun, as shown in figure 3.5 will also be installed. The alignment of the solenoids of TWS2 will be continued after the shutdown.

Table 5.11.: Misalignment calculated for the fourth solenoid of TWS1 with the measured longitudinal position. Data taken on 07.04.2021

Momentum (MeV/c)	Δx (mm)	Δy (mm)
3.5640 ± 0.0005	-0.327 ± 0.052	-0.454 ± 0.052

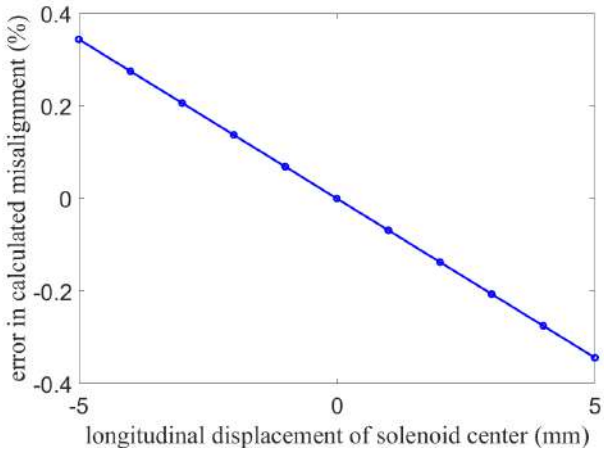

Figure 5.47.: Simulated impact of the longitudinal misalignment of SOL4 with Δx = 0.345 mm, $\Delta x'$ = 0.77 mrad, Δy = 0.446 mm, $\Delta y'$ = -0.775 mrad. The error for the misalignment in x is calculated w.r.t the design value.

5.8. Conclusion

The new particle accelerator called ARES, at the SINBAD facility at DESY, was put into operation during the course of this thesis. The ARES accelerator will produce electron beams with the goal of generation and characterization of ultra-short pulses in the sub-fs to few fs regime. The ARES linac has been commissioned with the beam fully characterized and optimized including the RF gun, the two TWS's and the first experimental area (EA1). Beam-based alignment of the focusing solenoids is an important part of the commissioning to optimize beam trajectory and to preserve the low emittance. For the ARES commissioning, the algorithm developed in chapter 4 to determine the misalignment of the solenoids installed at the RF gun and around the travelling wave structures was used to measure and correct the misalignments of the focusing solenoids at ARES. The sensitivity of the algorithm to the measured momentum was also determined. The impact of the earth magnetic field compensation coils on the beam trajectory was also studied. The comparison of the measured results with ASTRA simulations also determined the coordinates of the screen to align the field of view. As a result of the aligned solenoids, the quality of the produced electron beams could be greatly improved. The developed algorithm is generic and could be applied to any accelerator facility for aligning of the focusing solenoids. The associated work have been published in peer reviewed research articles [59] [58]. In summary, the developed algorithm used is simple, efficient, has been validated against ASTRA simulations and gives reliable results within the accuracy of the micromover system. The work has significantly improved the quality of the electron beam at ARES and can easily be adopted for any accelerator facility with the

hope that the developed algorithm can benefit the accelerator community in general.

6

Design and Simulation Studies of Final Focus System for a Laser Induced External Injection Experiment at ARES

6.1. Introduction

With the focusing system of the ARES linac being optimized, the beam is good to go towards the experimental area. This chapter is dedicated to the discussion of transporting the electron beam from the BC to an experimental area, where a potential LWFA experiment can be performed by externally injecting the ARES beam into a plasma cell. The scope of a LWFA experiment at ARES is discussed. The start to end simulations for the beam dynamics in the matching beam line is performed along with the design of the final focus system. Multiple working points, corresponding to different parameters of electron beam suitable for LWFA, are optimized with transverse phase space successfully matched to the plasma cell. Towards the end of the chapter, extensive tolerance studies for the focusing triplet are presented to determine the robustness of the design. Finally concluding the chapter, limitations and possibility of using electromagnetic quadrupoles for the matching beam lines is presented. The results from this chapter of the thesis have been published in [57, 71, 72].

6.2. Laser induced external injection experiments at ARES

As discussed in chapter 3, SINBAD is dedicated to research in the field of ultrashort electron bunches and will host multiple independent experiments [14], on laser driven advanced high gradient acceleration, techniques to take advantage of unique beam characteristics coming from the conventional RF accelerator. Advanced high gradient acceleration techniques include experiments for Dielectric Laser Acceleration (DLA) [15], Laser Wake Field Acceleration (LWFA) [16] and THz-driven acceleration in the AXSIS project [17]. ARES will be the first independent conventional accelerator at SINBAD based on S-band technology

with a photo-injector gun [20]. It is designed to provide ultrashort high brightness electron beams for injection into novel accelerators. The FWHM length of electron bunches is expected to reach a few fs to sub fs values. The electron gun relies on radio frequency (RF) accelerator technology for producing the electron bunches. This has several advantages. The ARES linac on one hand will allow advancing R&D on the "conventional" production of high brightness ultra-short electron bunches. On the other hand, the well-characterized bunches can be used to explore compact novel accelerators, characterized by accelerating fields with short wavelengths and therefore require the injection into short "acceleration buckets". The ARES bunches have been designed to constitute excellent probes to measure the energy gain and the quality of the acceleration. This section elaborates the two independent laser induced external injection experiments that could be performed at ARES.

6.2.1. External injection in a dielectric structure with transversely coupled drive laser

The first experiment planned and conducted at ARES is the injection of electron beam from the ARES linac into a dielectric micro-structure. In the framework of the ACHIP collaboration [51], aim of the DLA experiment at ARES is to show net acceleration of relativistic-electrons in a grating-type dielectric structure with as short as possible single bunches. As stage II, experiments on accelerating a micro-bunch train using dielectric structures will follow. By producing the micro-bunch train with the same laser as driving the DLA phase-stable acceleration is foreseen. The external injection of ARES beam in a dielectric structure has been studied as independent PhD projects [73, 74]. This subsection is based on the studies done in the aforementioned PhD thesis.

In the DLA experiment at ARES, the electron bunches produced in the RF gun are longitudinally compressed using the two travelling wave structures. A dedicated experimental area, consisting of a vacuum chamber, is installed after the linac which houses the DLA structure and is equipped with diagnostics for the DLA drive laser and electron beam. The DLA drive laser is synchronized with the master oscillator to control relative arrival time of the electron beam and laser pulse. The laser is transversely coupled to the dielectric accelerating structure as shown in figure 6.1. A matching section is located before the interaction point to match the electron beam to small transverse DLA aperture. This experiment aims to inject few fs electron bunches into a dielectric structure. This will allow to probe single cycle properties of accelerating fields and first net energy gain of relativistic electrons in a grating-type laser driven dielectric accelerator.

Figure 6.2 shows the sketch of the fused silica, $Si0_2$ structures to be used in DLA experiments at ARES. The structures were produced at Stanford University. It has one large aperture with an asymmetric aspect ratio, with width of channel being 2.3 μm and 1 mm in height. The matched electron beam also has corresponding asymmetric transverse beam size for maximum charge transmission through the structure. The drive laser has a wavelength of $2.05\mu m$ with a period of 6.85 fs. To see a clear net acceleration

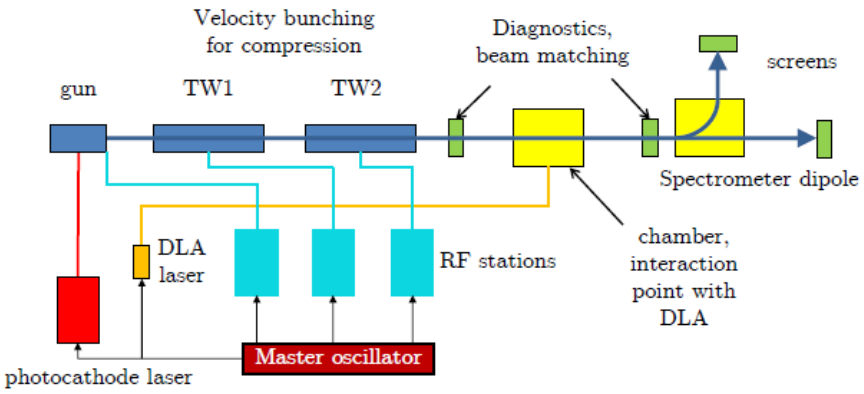

Figure 6.1.: Schematic of DLA experiment at ARES. The drive laser is transversely coupled to the dielectric structure and synchronization of all accelerator components to one master oscillator allows overlapping of ps laser pulse with fs electron bunch at the interaction point. Picture courtesy [74].

signal, a quarter of the period in bunch length is aimed for. In general, for any DLA experiment, following requirements should be considered to match the transverse and longitudinal phase spaces of the electron beam.

- Horizontal beam size should be smaller than the DLA horizontal aperture ($<$ 3 micron at ARES)
- Small vertical beam size at the DLA (~hundreds of micron vertical aperture)
- Bunch length smaller than the acceleration bucket
- Small transverse emittance to maximize the interaction length and hence the charge transmission

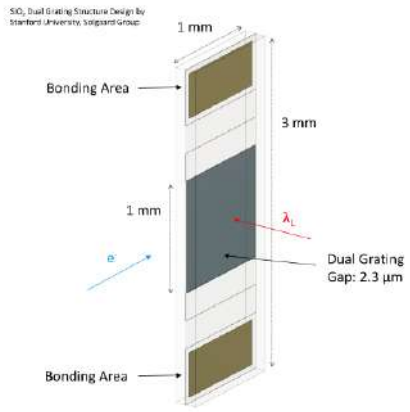

Figure 6.2.: Sketch of SiO_2 DLA structure used at ARES. The structures are produced according to electron and laser beam parameters at ARES. Picture taken from [73].

A quadrupole triplet downstream the second TWS is located to focus the beam in horizontal x-direction to achieve the above mentioned requirements. Since, a symmetric beam in DLA is not a critical requirement, the vertical beam size is kept small enough while achieving the minimum beam size in horizontal

plane. Table 6.1 gives the matched beam parameters at the interaction point for both stage I and stage II experiments. The matching beam line for the DLA consists of a quadrupole triplet, horizontal and vertical beam steerer and DESY MDI screen station for transverse beam profile measurement. Since the laser is transversely coupled, the main beam line has no space constraints for the placement of matching lattice. In other words, quadrupoles and steering magnets can be freely placed to achieve the required matched beam parameters. The experimental chamber is located 4 m down stream of the second travelling wave structure. Because of the low charge WP corresponding to 0.5 pC, the beam can be transported and transversely matched using conventional quadrupole triplet to the small DLA aperture size while maintaining the bunch length of 1.6 fs FWHM. It is worthwhile to note the the BBA of solenoids performed in the chapter 4 and 5 has a significant influence on the emittance preservation down to the experimental chamber which is very important for the DLA experiment since high charge transmission is aimed through the DLA.

Table 6.1.: Simulated ARES beam parameters at the interaction point for DLA experiment [73, 74].

Parameters	**Units**	**Stage I**	**Stage II**
Mean energy	MeV	100	50
Charge	pC	0.5	0.5
rms energy spread	keV	178	∼75
normalized transverse emittance x	nm	45	44.7
normalized transverse emittance y	nm	38	44.2
rms beam size x	μm	2.04	1.5
rms beam size y	μm	9.73	18.1
bunch length FWHM	fs	1.6	112.3

6.2.2. External injection experiment with on axis coupled drive laser

Another potential external injection experiment that can be performed at ARES is Laser Wake Field Acceleration Experiment (LWFA). LWFA provides an accelerating gradient of ∼100 GV/m, which is several orders of magnitude higher than conventional accelerators. This reduces the length of the acceleration channel by orders of magnitude and hence offers the possibility of compact and cost effective accelerators. For example with a stable LWFA, the length of an injector for a synchrotron facility maybe reduced from hundreds of meters to few meters [75, 76]. In LWFA, an intense laser pulse propagating in a plasma generates charge separation by excitation of wake-fields, inducing strong electric fields.

The use of conventional photo injectors for producing electron bunches to inject into novel accelerators has several advantages. The ARES Linac on one hand will allow the R&D on the production of high brightness ultrashort electron bunches. On the other hand short bunches fits into very compact novel accelerators, with short accelerating field wavelength. Hence such bunches constitute excellent probes to measure energy gain and the quality of acceleration. The potential external injection LWFA experiment at ARES can be an important step towards stable LWFA as it combines the reproducible conventional RF-based accelerator technology, with high-power plasma wake field dynamics [13, 16]. The RF-based

technology allows manipulation of the phase space of the electron bunches entering the plasma hence providing better control and quality as well as optimization of the plasma experiment. The preservation of beam quality in novel accelerators depends on the detailed parameters and quality of the injected beam e.g. bunch shape, bunch length, emittance, arrival time stability, energy etc. ARES provides the option of widely tunable WP's and bunch shapes for external injection LWFA accelerator R&D. At ARES, the electron bunches can be compressed either via velocity bunching or by using a magnetic bunch compressor or by using a hybrid scheme to achieve the desired bunch lengths in the range of sub fs to few fs [39, 77, 40]. The characterization of such ultra-short bunches is a research field in itself and ARES will also serve as a test bench for novel diagnostic devices in the low to medium charge range of up to 30 pC and with sub-fs to few fs bunch length [41, 42]. All these features contribute in making ARES a promising candidate where LWFA experiments with external injection could be performed. This potential is explored in this chapter as part of the PhD.

6.3. LWFA concept

Since the LWFA concept was first introduced [6], it has been a subject of extensive studies with significant progress in recent years [9, 10]. Many important milestones have been demonstrated such as achieving GeV energies in only cm scale [12]. Today's focus for these devices is to reach beam stability, similar to established RF accelerators, by deploying various concepts such as feedback control systems. Recently another milestone has been successfully demonstrated at DESY with 24 hours of stable operation of laser plasma acceleration [21].

6.3.1. Injection techniques

For injecting electrons in a plasma wake, several concepts have been developed over the past years. The early days of LWFA experimentation imply the concepts of wave breaking [78]. This method was simplest for experimental realization of LWFA and the first GeV-range beams were achieved employing this technique [9, 12] . The concept of wave breaking was efficient for trapping electron beams in plasma wake but results in low quality accelerated beams with low shot to shot stability. Since the wave breaking concept depends on the properties of the laser driver, and hence has considerable shot-shot variations coming from the high power laser.

Controlled electron injection into LWFA has been a subject of extensive studies over the past few years. Some of these techniques make use of the ionizing capabilities of the laser system so that electrons can be released into wakefields [79]. On the other hand, additional lasers can be implied, to push the electrons into wake fields generated by the main laser, by virtue of their ponderomotive forces [80, 81]. Multiple ionization techniques have been developed and now a days commonly used in experiments for improved beam quality [82, 83, 84, 85, 86].

6.3.2. External injection in LWFA

The beam quality of plasma based accelerators has still a long way to go compared to accelerators with conventional radio frequency technology, specially in terms of beam stability and lower energy spread. Meeting the requirements of low energy spread for applications such as FELs is one of the biggest challenges of plasma based accelerators. In addition to the electron injection techniques listed above, an alternative concept is to inject a beam in the plasma cell, which has been accelerated and optimized in a conventional RF Linac. This technique, known as external injection, will not only give high degree of freedom to tailor the beam properties to the plasma accelerating stage but would also have more beam stability thanks to modern day RF technology. The concept of external injection has been indirectly tested in proof of principal plasma experiments to show the accelerating capabilities of laser driven plasma waves by increasing energy of a part of the injected electron beam [87, 88]. External injection, though comes with freedom for beam control, has many challenges of its own. The biggest difficulty comes from the tight requirements of a plasma cell where beam has to be injected and matched to the size of the accelerating channel in the plasma, i-e Twiss parameter beta function on the mm and bunch length on the femtosecond scale. Promising aspects for external injection has been recently demonstrated with 100% capture efficiency at Tsinghua University [89]. Many projects at research institutes worldwide are researching the concept of external injection in LWFA. These includes SPARC LAB at INFN, Italy [90, 91], European collaboration project EUPRAXIA [92], and the DESY projects REGAE [93] and ARES at SINBAD [40, 54, 16] to name a few. The EUPRAXIA collaboration has recently published the worldwide first conceptual design report [94] for a FEL facility, to present the study for high energy plasma based accelerator with industrial beam quality and user areas.

6.4. Review of final focus systems

Designing the focusing system to inject into laser driven external injection experiments is an important research topic in itself since beam should be properly matched to the small acceleration channel in order to preserve emittance and to get efficient acceleration with preserved beam quality. Conventional accelerators with an intermediate energy range use Electro Magnetic Quadrupoles (EMQ) for transporting and focusing the electron beam up to the experimental point. Accelerators with higher energies in the range of GeV requires larger gradient quadrupoles for beam transport, where electromagnetic technology ultimately reaches its limits. Beyond this limit superconducting magnets becomes a viable option. Superconducting magnets with their cryogenics systems are an expensive option compared to electromagnets both in terms of installation and operation. They are bulky components in a beam line and are well suited for use in big high energy accelerators. However, in applications with compact beam lines, the use of Permanent Magnets (PM) is an alternative and can have many advantages. PM can bring down the size and cost by eliminating infrastructure for water cooling systems and absence of power supplies and cables. Permanent magnetic Quadrupoles (PMQ) can be very much reduced in size with high magnetic

field strengths, making them suitable for use in future compact accelerators like LWFA. The Pros and cons of PM are summarized in Table 6.2.

Table 6.2.: Pros and Cons of using Permanent Magnet

Pros	Cons
Compact with High gradient No power supplies and cooling system required	Limited variability of gradient Can impact neighbouring magnets since degaussing of PM is not possible

Halbach first proposed the idea of building multipole systems using an array of magnets with specific arrangements so that a strong magnetic field is generated on one side and a weak stray field on the opposite side [95]. A Halbach type PMQ triplet is a promising scheme used as a final focus system and provides high gradients for strong focusing required for LWFA. In a Halbach structure, the magnet is segmented into geometrically identical pieces with a continuously varying magnetization for each piece with azimuthal angle ϕ. This geometry augments the field in one direction and cancels the field in the others, hence resulting in nearly ideal quadrupole field profile. A high remnant field B_r permanent magnetic material is used for manufacturing of PMQs. One example is NdFeB, which has a remnant magnetic field of 1.22 T. The achievable field gradient for such geometry is a function of magnet inner and outer radii and can be approximated by an analytical formula expressed as below [95].

$$\begin{aligned} G &= 2B_r K \left(\frac{1}{R_i} - \frac{1}{R_o}\right) \\ K &= \frac{M}{2\pi} cos^2\left(\frac{\pi}{M}\right) sin\left(\frac{2\pi}{M}\right) \end{aligned} \tag{6.1}$$

where B_r is the remnant field, M is the number of segments in the Halbach array, R_i and R_o are the inner and outer radii of the magnet respectively. From equation 6.1, it is clear that the gradient increases with a larger number of segments since K tends towards 1 as M increases. However larger segments imply that the magnet becomes more complicated and expensive to manufacture. In the end, it is a balance between the required gradient and ease and cost of manufacturing.

In conventional electromagnets, the gradient can be easily tuned by varying the current. However tuning the strength of permanent magnet is a much more challenging task. Many designs exist in theory and practice to tune permanent magnetic quadrupoles. Tuning in a limited range can be achieved by longitudinal positioning of the quadrupoles. More complex designs can be employed to have a wider tuning range by using hybrid schemes involving mechanical motions of poles, magnetic rods or having multiple rings of Halbach arrays that can be moved to vary the gradient. In the following paragraphs, some of the PMQ which have been built and are in use at different facilities are discussed. Several facilities uses fixed and variable gradient PMQ for a variety of applications. Some of them are listed below:

- A 16 segment Halbach type PMQ based final focus system has been implemented for Inverse Comp-

ton Scattering experiment at LLNA PLEIADES. Its an asymmetric triplet configuration with gradients as high as 560 T/m with very small inner radius of 2.5 mm and magnetic length of 10.4 mm. This design provides the largest gradient achieved with permenant magnetic quadrupoles. The tunability is achieved through longitudinal movement of the magnets [96].

- A PM Halbach ring system is proposed at Kyoto University in collaboration with SLAC as a final focus lens for a positron-electron linear collider accelerator [97]. This system consists of permanent magnets as well as iron poles. The system has a bore radius of 7 mm with a magnetic length of 100 mm generating a maximum gradient of 289 T/m.

- For a table-top FEL application at the department for Physics in Munich University, two 12 sector Halbach ring systems of 17 mm (15 mm) magnetic length and 3 mm bore radius achieve a gradient of 500 T/m [98].

- At ESRF, a compact PMQ with a hybrid type design, using soft iron and rectangular PM blocks, has been designed for a storage ring. A prototype has been built which provides a gradient of 85 T/m having bore radius of 12 mm and magnetic length of 226 mm [99]. The picture of the magnet is shown in figure 6.3

- At Soleil, a hybrid PMQ called QUAPEVA, has been built for the COXINEL project with an objective of FEL amplification [100]. The QUAPEVA consiste of Nd_2Fe_14B magnets achieving a maximum gradient of 202 T/m with a bore radius of 6 mm. QUAPEVA has a high tunability range of 45% and is obtained by orienting the tuning magnets. The schematic and picture of assembled magnet is shown in figure 6.4. The picture is taken from [100].

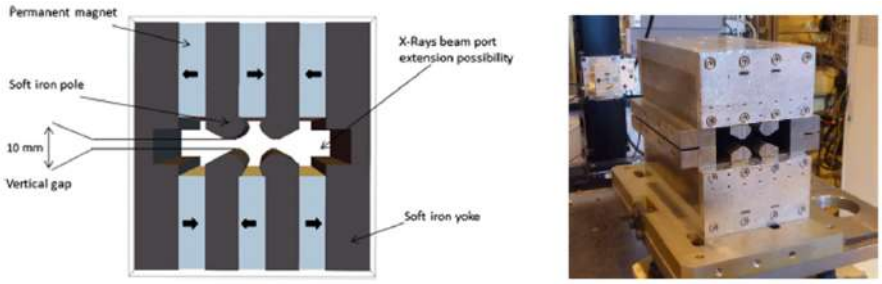

Figure 6.3.: Hybrid permenant magnet based quadrupole with soft iron poles. Picture taken from [99].

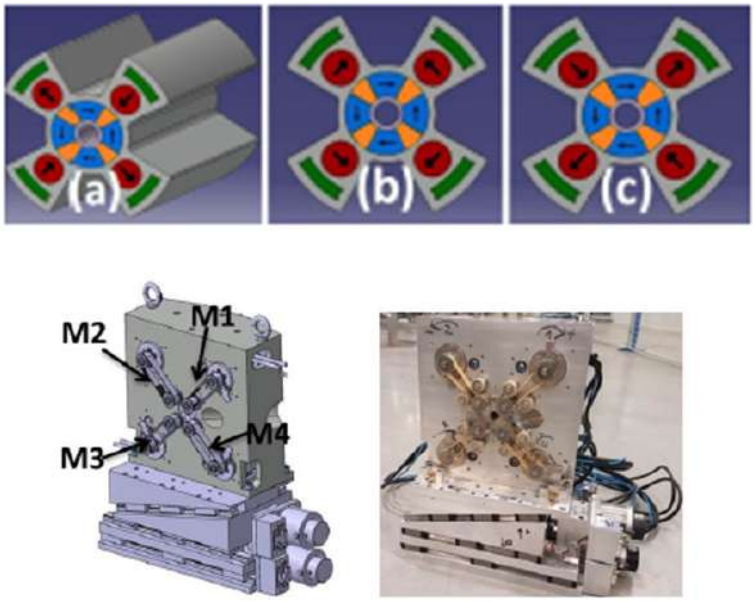

Figure 6.4.: QUAPEVA Magnets. Top pictures shows the permenant magnet blocks (blue) and rotating cylinders (red), with (a) maximum (b) intermediate and (c) minimum gradient. Bottom pictures shows the mechanical design and an assembled magnet. Picture taken from [100].

6.5. Design requirements and constraints for LWFA beam line

6.5.1. Constraints for the matching beam line

In the external injection LWFA experiment, the laser and electron beam are collinearly injected into a plasma target. This collinearity, together with the required beam diagnostic elements, introduces strict constraints on both the transverse and longitudinal dimensions of the final focus system. On one side, the tight matching requirements for the electron beam into the plasma (c.f. section 6.5.3) imply the need for large focusing gradients and hence tight apertures. On the other, the longitudinal extent of the system is constrained due the tight apertures and the growth of the laser spot size w out of focus, which for a Gaussian pulse, is given by [53]

$$w(z) = w_0 \sqrt{1 + \left(\frac{z}{Z_R}\right)^2}\,, \tag{6.2}$$

where $Z_R = \pi w_0^2/\lambda_0$, w_0 and λ_0 are, respectively, the Rayleigh length, spot size at focus and wavelength of the laser, while z represents the distance to its focal position.

Schematic of the laser beam at its waist and the parameter definitions are shown in figure 6.5. Since the divergence of the laser beam depends on the beam waist w_o, the design of the laser beamline and hence in turn the space constraints for our final focus system are strongly dependent on the laser parameters.

The required mirror for the laser incoupling is housed in a beam pipe with a diameter of 10 cm. The beam pipe size is chosen to accommodate the mirror dimensions required for focusing the 100 TW peak power laser beam. A hole in the mirror allows the electron beam transmission and, collinearly to the laser beam, the electron beam enters the plasma cell. At the focal point, the laser beam has a design

waist of 40 μm. For the external injection experiment, the laser beam also has to pass through the PMQ triplet to reach the plasma cell. Hence the free aperture, defined by the distance of the magnetic pole tips of the PMQ should be bigger than the laser spot size at the position of quadrupoles. Considering the laser beam evolution from figure 6.5, the aperture of PMQ is chosen to be 10 mm. The laser parameters and the laser beam line design dictate the limits for the physical dimensions of the PMQ inner and outer radii, the length of the total triplet and also set constraints to the positions of the focusing magnet. The distance between the exit of the BC and the entrance of the plasma cell is ~3.3 m to account for the space required for diagnostics and for focusing the laser beam.

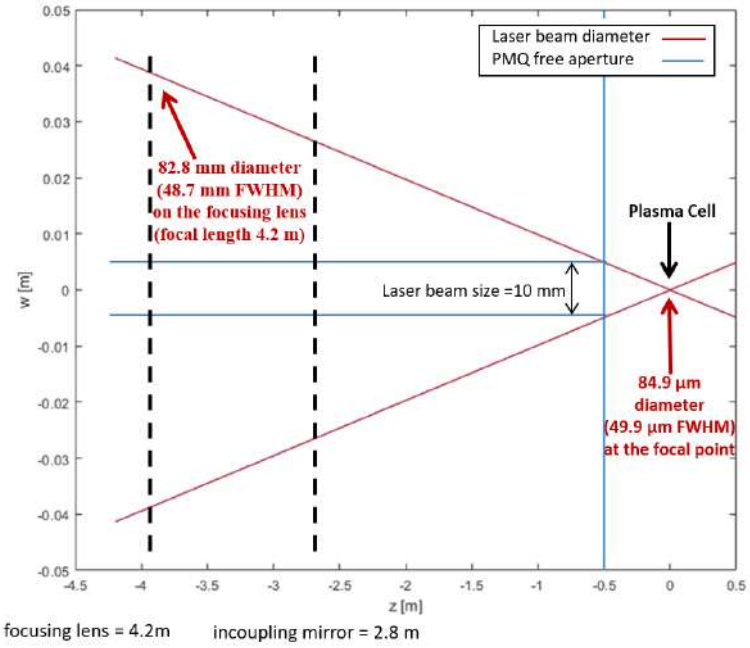

Figure 6.5.: Evolution of the laser beam along the direction of beam propagation. The origin here is set at the focal point of the laser beam which is the entrance position of the plasma cell. A Gaussian laser beam is assumed.

6.5.2. Laser system for LWFA experiment

Two laser systems have been considered for the potential LWFA experimental studies at ARES. The key parameters for both laser systems are presented in Table 6.3. Since the divergence of the laser beam depends on the beam waist w_o, the design of the laser beamline and hence in turn space constraints for our final focus system has strong dependence on the laser parameters. Initially the experiment was designed considering the parameters for the ANGUS laser beamline under the Athena-e project at SINBAD. Recently, a new high power laser project, KALDERA, has been initiated at SINBAD and the LWFA experimental plan was subsequently remodeled taking into account the design parameters for the KALDERA laser. The matching beamline lattice has been designed exploring the possibilities for both cases. Figure 6.6 shows the evolution of the laser beam over the parabola for the two cases of Table 6.3.

As can be seen from the figure 6.6, for the same laser power, having a wider w_o makes the laser less intense, which leads to less strong accelerating and focusing fields in the plasma and therefore to less strong matching conditions. Also a wider w_o changes the divergence of the laser which inturn relaxes the space constraints for the matching lattice.

Table 6.3.: Key parameters for the Laser setup

Parameters	Units	Case 1	Case 2
Wavelength (λ_o)	μm	0.8	0.8
Peak normalized vector potential (a_o)		1.4	1.4
Beam waist (w_o)	μm	42.4	26.6
Pulse energy (E)	J	3	3
Peak power (P)	TW	100	100
Pulse length (Δt_{FWHM})	fs	30	30

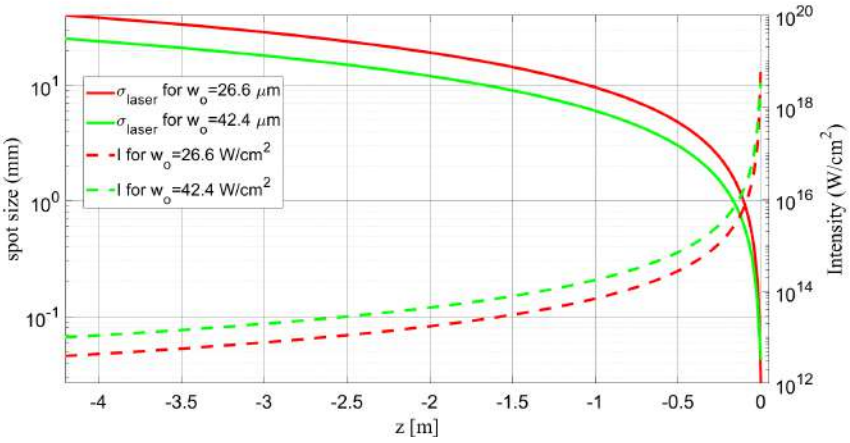

Figure 6.6.: Comparison of laser beam evolution for two cases of Table 6.3.

6.5.3. Matching criterion

It is extremely important to match the externally injected electron beam to the focusing fields of the plasma accelerator for preserving the beam quality. Strong focusing fields in the plasma puts tight requirements on the beta function at the injection point of the beam into the plasma cell. Matching requirements depend on the focusing strength of the plasma channel [101], which in turn depend on the plasma density. For the LWFA experiment potentially designed at ARES, for a plasma density of 10^{17} cm^{-3}, the required $\beta_{x,y} \approx 1$ mm for a quasilinear regime, with beam energy of 100 MeV. The mm range values for matched β is challenging to achieve with conventional quadrupoles. This strict constraints on the matched β however can be significantly reduced by using an upramp of the longitudinal plasma density profile. By properly tailoring the density transition for the plasma, the ramps can allow for larger beta values at the injection point i-e the start of the plasma ramp. The beta function is then gradually reduced by the slowly increasing focusing fields of the plasma, which grows with the plasma density, until the beta function reaches the desired value at the plateau.

In order to preserve the beam emittance during acceleration in the LWFA, matching the Twiss parameters of the injected electron beam to those determined by the large focusing fields inside the plasma is required [102]. Assuming $\alpha_{x,y} = 0$, the matched value of the beta function, for a plasma stage with a uniform focusing gradient g, is given by [102, 103],

$$\beta_m = \sqrt{\frac{cm_e}{e}\frac{\gamma_r}{g}}\ , \tag{6.3}$$

where g is the focusing gradient (in units of $\mathrm{T\,m^{-1}}$) inside the LWFA, γ_r is the relativistic Lorentz factor of the beam and e is the electron charge.

To match the ARES beam to the plasma cell, two possible cases for the plasma density profile have been investigated.

Plasma density profile case 1:

In one case, the longitudinally tailored profile of the plasma target is given by Equation 6.4

$$f_z = \frac{1}{\left(1 - \frac{z - z_{o,u}}{l_u}\right)^2} \tag{6.4}$$

where $z_{o,u}$ is the longitudinal coordinates of the start of the plasma upramp, l_u is the optimized plasma ramp length. The plasma ramp length is given by Equation 6.5 [55]

$$l_u = \beta_{p,o}\sqrt{\left(\frac{(N+1)\pi}{\ln\frac{\beta_i}{\beta_f}}\right)^2 + \frac{1}{4}} \tag{6.5}$$

$\beta_{p,o}$, the beta function of the electron beam matched to the plasma section, is defined by $\beta_{p,o} = \sqrt{\frac{\gamma_b cm_e}{(ge)}}$, where γ_b is the beam Lorentz factor and g is the transverse focusing fields in the plasma, $N = 0, 1, 2...$, β_f is the beta function of the beam matched to the plasma section and β_i is the beta function of the initial beam. Plugging all these definitions, the lengths of the plasma upramps are given by Equation 6.6

$$L_u = \left(\frac{\beta_i}{\beta_f} - 1\right) l_u \tag{6.6}$$

Such tailored density profiles have been studied for matching into and out of the plasma and has been experimentally demonstrated in [104]. The matched beam in this case has $\beta_{x,y} \sim$ few mm with beam being at its waist i-e $\alpha_{x,y} \sim 0$.

Plasma density profile case 2:

A second case was considered for tailored and longer upramps. In the LWFA stage considered for this case, which features a plasma electron density of $10^{17}\,\mathrm{cm^{-3}}$ and a laser driver with the parameters of case II from Table 6.3, the resulting focusing gradient is $g \simeq 1.1\,\mathrm{MT\,m^{-1}}$ at the center of the stage. Thus, for a beam energy of 150 MeV, equation (6.3) yields $\beta_m \simeq 0.7$ mm. This is a strong requirement that could be challenging to achieve, even with the considered PMQ triplet. Fortunately, this condition can be relaxed by using a properly-tailored vacuum-to-plasma transition (or upramp) [105, 106, 107, 101]. In

this study, a plasma upramp following the profile

$$n_{p,r}(z_r) = \frac{n_{p,0}}{\left(1 + \frac{z_r}{L_r}\right)^2} \tag{6.7}$$

has been used, where $n_{p,r}$ is the plasma density along the ramp, $n_{p,0}$ is the on-axis plasma electron density in the plateau, z_r is the distance to the plateau, and L_r is a parameter controlling the plasma density decay rate in the ramp. This profile has been shown to efficiently relax the matching requirements at the plasma entrance [107]. For the present case, $L_r = 2\,\mathrm{mm}$ has been considered, with a total ramp length of 3 cm.

The required Twiss parameters at the entrance of such a ramp can be analytically calculated when the LWFA operates in the so-called blowout regime [107], where a laser driver with $a_0^2 \gg 1$ is able to generate a trailing ion column fully cavitated of plasma electrons [108]. This, however, given the laser parameters in Table 6.3, is not the case here. As such, these parameters have been determined by means of tracking simulations with the Wake-T code [109] using a non-linear 1D fluid model for the plasma wakefields. This model, although simple, allows for an accurate estimate of the required beam parameters, as demonstrated by the results in [57]. In the simulations, a particle bunch with the ARES beam properties, but with $\alpha_{x,y} = 0$ and $\beta_{x,y} = \beta_m$, has been back propagated from the entrance of the plateau until the beginning of the plasma upramp. This technique, also used in [106], yields a final beam with the required Twiss parameters at the ramp entrance such that a matched beam is achieved at the plateau. For the case simulated here, this means a beam with $\beta_{x,y} = 11.8\,\mathrm{cm}$ and $\alpha_{x,y} = 4.4$, which are therefore the target Twiss parameters of the final focus system. These parameters are equivalent to a virtual focus with $\beta_{x,y} \simeq 5.8\,\mathrm{mm}$ at waist, a significant improvement over a case with no ramp.

The entrance of plasma cell refers to start of plasma ramps for which the matching criterion is defined. The two cases of longitudinal plasma density profile, studied in this thesis are shown in Table 6.3.

Table 6.4.: Longitudinal Plasma Density Profiles for matching ARES beam. LWFA stage with plasma electron density of $10^{17}\,\mathrm{cm}^{-3}$ is used for both cases. Upramp refers to the tailored vacuum-to-plasma transition for plasma density profile until it reaches the plateau. Like wise, the downramp is defined as plasma-vacuum transition after the plasma cell.

Plasma Case	Corresponding Laser Case	Upramp cm	Accelerating Region cm	Downramp cm
Case 1	Case I	0.6	9.5	0.6
Case 2	Case II	2	17	2.5

6.5.4. Choice of focusing system at ARES

In section 6.4, many different options for the final focus system employed at various facilities is discussed. The required gradient depends on the application and required beam parameters. At ARES, the final focus system must have sufficiently large bore radius that laser beam could pass through the magnets

and should be sufficiently compact to be placed inside the laser beam pipe. Moreover, the length of the quadrupoles should be small enough that they can be easily installed within the space occupying infrastructures from laser and electron beam lines as explained in section 6.5.1 and section 6.5.2. Also the quadrupoles should be strong enough to meet the matching criterion defined in 6.5.3. A promising option for fulfilling these requirements is the use of a Halbach-type permanent magnetic quadrupole (PMQ) triplet [95]. This offers large focusing gradients in excess of $100\,\mathrm{T\,m^{-1}}$ with only $\sim$1 cm long magnets. The use of this technology has already been explored for applications such as inverse Compton scattering [96] as well as for the focusing, capture and transport of beams from plasma accelerators [110, 111, 112, 113, 114]. As a result, a PMQ triplet was primarily chosen for the final focus system at ARES. It should however be noted that ARES is an evolving science project and the scientific direction of ARES is continuously reviewed. A second design of final focus system using electromagnetic quadrupole triplet, has also been proposed in section 6.9.

6.6. Working points of ARES Linac for LWFA

Two typical working points, covering different ranges of beam parameters, for ARES linac were simulated. The beam was transported through the linac and compressed with magnetic bunch compressor to achieve the desired bunch length. The working points were simulated for the ARES base line design i-e with 100 MeV beam energy. An energy upgrade of the accelerator has been foreseen within the Athena-e project allowing the installation of a third travelling wave structure for energy upgrade and a high energy diagnostic beamline including the novel polarix TDX for bunch length measurement [41]. The two WP's for LWFA at ARES has been studies with both layout of ARES i-e with ARES baseline energy of 100 MeV utilizing two accelerating cavities and the upgraded layout with three accelerating cavities at higher energies.

WP1: The low charge working point with 0.8 pC, namely, WP1, has smallest arrival time jitter $\sim$ 10 fs rms and with sub fs bunch length. The two travelling wave structures are operated at same amplitude and phase. The electron bunches from this WP aim to provide a time resolution to serve as probe particles inside the plasma cell since the amplitude of accelerating field gradients is also of the order of few μm in the plasma cell and hence will be used as first external injection test run at the ARES linac. The sub fs bunch will also be used for DLA experiment at ARES experimental area 1 [15]. For the energy upgrade of ARES utilizing the third travelling wave structure, WP1 was also simulated using on crest acceleration for one of the travelling wave structure to achieve higher energies. This significantly mitigated the strong effects of space charge observed in the low enrgy i-e 100 MeV case where it was extremely difficult to transport and match the beam to large distances keeping the transverse and longitudinal phase spaces intact. However, mitigating the effects of SC by increasing energy, as a result of on crest acceleration, has a trade off on arrival-time jitter. The R56 of the bunch compressor has to be adjusted so that the arrival time jitter is slightly higher now and is around 15 fs compared to 10 fs for 100 MeV beam.

WP1: WP2 uses the same compression scheme as of WP1, i-e pure magnetic bunch compressor, but have bunches with higher charges, 5-10 pC with longer bunch length of 10 fs FWHM, or 4.3 fs rms. The peak current in this case is 1 $\sim$1 kA, approaching the requirements of several use cases [115]. WP2 is useful for studying the external injection concepts to get a useable beam quality after acceleration in a plasma channel. Electron bunches longer than a few fs with energy spreads well below 1% are ideal e.g for plasma-driven FELs. This WP is similar to the WP at BELLA facility in LBNL for which a broad energy spread electron bunch of $\sim$100-200 MeV energy, 6.25 pC charge and 3.3 fs rms length was used for injection into a second stage LWFA [116]. The bunch after plasma stage has an integrated energy spread of 0.25%, a normalized emittance of 0.3 μm and a peak current of 0.45 kA. The simulated FEL peak power is above 10^7 W with a resonant wavelength of 87 nm.

6.7. Simulation results

6.7.1. Design optimization

Start-to-end simulations were carried with a combination of ASTRA [37], ELEGANT [35]. A total of four million macroparticles were used before the energy selective slit-collimator in the bunch compressor. The rms beam size of the inverse parabolic laser shape on the cathode was 181 microns, while the Gaussian rms pulse duration was 3 ps; consistent with ARES photocathode laser infrastructure. IMPACT-T [36] supported the calculation of coherent synchrotron radiation effects in the Bunch Compressor (BC). Design of the BC is beyond the scope of this thesis. Further information about the design and simulations of BC can be found in [49, 57].

In order to optimize the working points of the ARES, beam dynamics simulations for the matching beamline after the BC was done using Elegant (without SC) and then ASTRA [37] to optimize and include the effects of 3D SC. For single objective optimization, optimization routine, linacOpt [38] can be applied. In this routine, the particle swarm optimization algorithm is used to fine the local and global minima of given objective functions. As a starting point, the linacOpt was applied to find the minimum beta function at the focal point i-e the entrance of the plasma cell. However, this procedure was limited to single objective function. In our case, there are several specific constraints leading to extremely long optimization time and making it impossible to optimize several objective functions. Hence the optimization was done manually as follows. Since the electrons are already relativistic, the matching was optimized using transfer matrix based code elegant, without taking space charge into account. Elegant allows to setup multiple objective functions with several constraints. However, since the beam is highly compressed and charge density for WP's are considerably high, it is necessary to optimize in ASTRA including the effects of 3-D space charge. Following the elegant optimization, the quadrupole settings were imported to the ASTRA. The manual optimization and scans in ASTRA then leads to final design.

The optimization parameters for the PMQ triplet were the length of the quadrupoles, the strength of the quadrupoles and the distances between the three quadrupoles. Based on the laser beamline layout, as

shown in Figure 6.6, the constraints for the final focus system were the inner and outer radii, and the focal length. Focal length should b small to avoid electron beam blow-up over long drift propagation. Another constraint was to have sufficient distance between the last quadrupole and the plasma cell to account for diagnostic screens for laser and electron beam profiling. We set the origin of our simulations at the exit of last magnet of the BC and the beam line is simulated from this point till the entrance of plasma cell corresponding to the start of plasma upramp as defined by the matching criterion in section 6.5.3. The matching schemes for two layouts of ARES, namely using two and three travelling wave structures are discussed in following sections.

6.7.2. Simulations for ARES baseline energy

The key parameters for the working points at the BC exit and at the entrance of the plasma cell, simulated in ASTRA, are summarized in Table 6.5. The full beam distribution is included in the calculation of statistical parameters. The three quadrupoles of the triplet have lengths of 0.055 m, 0.033 m and 0.040 m with strengths of 50 m^{-2}, -180 m^{-2} and 130 m^{-2} respectively. The details parameters for the matching triplet is given in appendix B. The distance between the last magnet and the plasma cell is 0.25 m which is sufficient to place screens for laser and electron beam profiling. Figure 3-6 shows the evolution of the electron beam parameters over the drift space from the BC to the plasma cell. Figures 6.8 and 6.10 shows the evolution of the electron beam parameters over the drift space and through the PMQ triplet from the BC to the plasma cell, for WP1 and WP2 respectively. The transverse and longitudinal phase spaces of the electron beam at the BC exit and at the entrance of plasma cell, for WP1 and WP2, are shown in figure 6.9 and 6.11 respectively. From figures 6.8 and 6.10, it is evident that at the start of plasma ramp, the electron beam is well matched with preserved transverse emittance and bunch length shorter than the accelerating wavelength in the plasma, for efficient acceleration. The transverse phase space distributions in figures 6.9 and 6.11 show that beam is symmetric in both planes as required by LWFA. The PMQ triplet also ensures to maintain the current profile from the longitudinal phase space with $\sim$kA of peak current.

It is worthwhile to note that SC plays a significant role specially after the BC when the beam is compressed. The impact of space charge over a drift of 3.5 m, without external focusing is shown in figure 6.7. It could be seen that the beam size quickly blows up and strong external focusing is required to match the beam to the plasma cell.

6.7.3. Simulations for ARES energy upgrade

The use of third travelling wave structure allows the ARES to move to higher energies upto 200 MeV, depending on the injection phase. The third travelling wave structures helps to mitigate the strong effects of SC over the long drift and allows transporting much higher peak current for the same amount of bunch charge. The effects of space charge over the drift space for WP1 and WP2 using 3 TWS, from

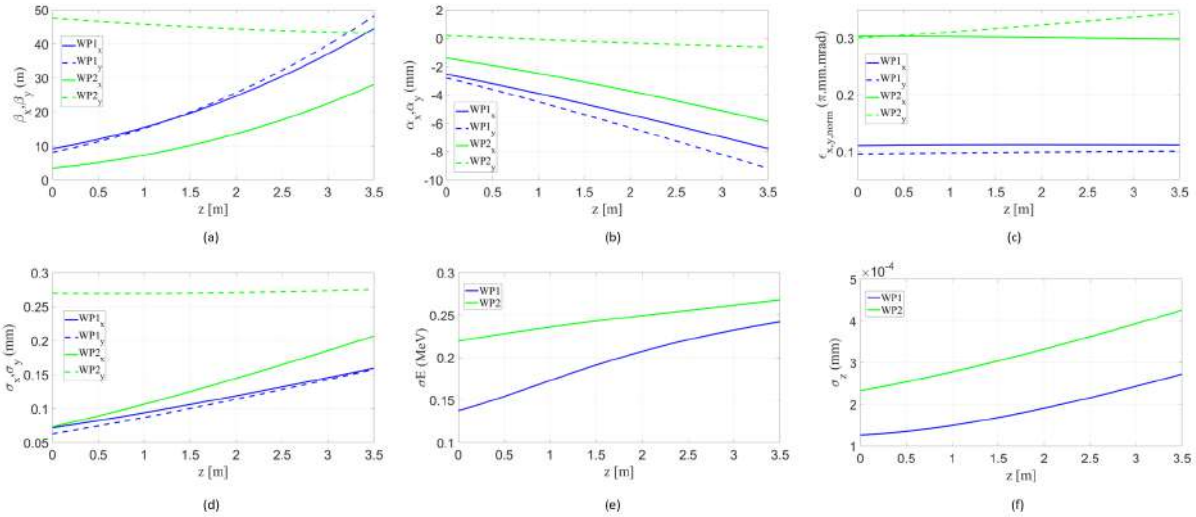

Figure 6.7.: Evolution of the electron beam parameters, without external focusing, for WP1 ARES, simulated in ASTRA, along the beam line from the exit of the BC until the entrance of the plasma cell. The origin here is set at the exit of the last magnet of the BC. The parameters shown are the Twiss parameters in (a) $\beta_{x,y}$ and in (b) $\alpha_{x,y}$, in (c) the normalized transverse emittance $\varepsilon_{x,y}$, in (d) the rms transverse beam sizes $\sigma_{x,y}$, in (e) the energy spread σ_E and in (f) the bunch length σ_z.

Table 6.5.: Bunch Parameters at the BC exit (I), matched beam at the entrance of plasma cell (II).

Parameters	**WP1**		**WP2**	
	I	**II**	**I**	**II**
Energy (MeV)	100	100	100	100
Bunch Charge (pC)	0.8	0.8	5.5	5.5
Bunch length-rms (fs)	0.42	0.89	0.7	2.14
ε_x (π.mm.mrad)	0.11	0.11	0.3	0.3
ε_y (π.mm.mrad)	0.095	0.11	0.3	0.4
β_x (mm)	9.24×10^3	7.55	3.45×10^3	8.89
β_y (mm)	8.21×10^3	7.57	47.22×10^3	8.86
α_x	-2.55	-0.4	-1.39	-0.25
α_y	-2.81	-0.2	0.19	0.10
$\sigma_x\mu m$	71.8	2.09	73.28	3.7
$\sigma_y\mu m$	63.1	2.13	269.75	4.3
RMS energy spread (%)	0.13	0.28	0.22	0.27
Peak Current (kA)	1	0.35	3.5	1.6

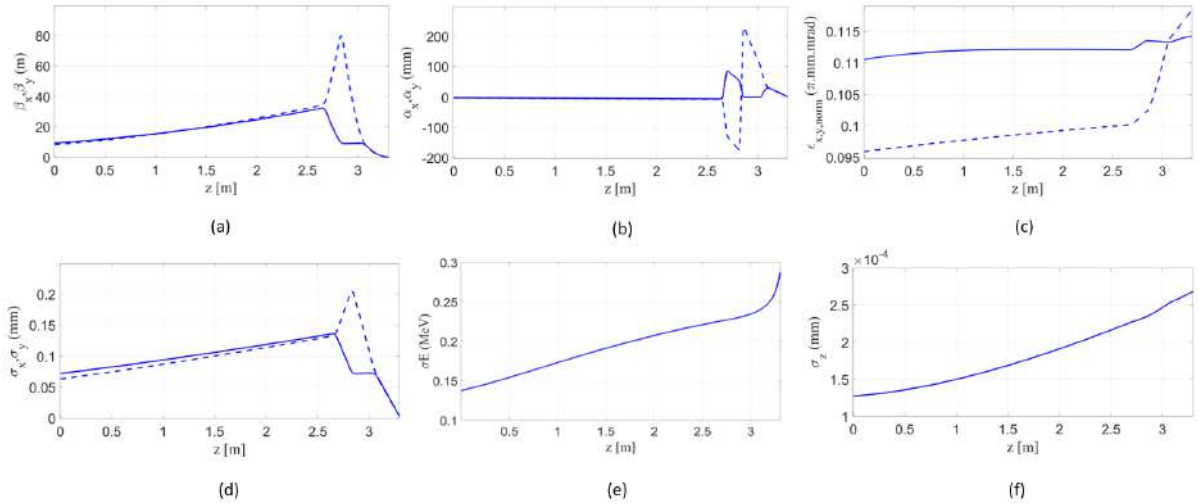

Figure 6.8.: Evolution of the electron beam parameters for WP1 using 100 MeV, simulated in ASTRA, along the beam line from the exit of the BC until the entrance of the plasma cell. The origin here is set at the exit of the last magnet of the BC. The parameters shown are the Twiss parameters in (a) $\beta_{x,y}$ and in (b) $\alpha_{x,y}$, in (c) the normalized transverse emittance $\varepsilon_{x,y}$, in (d) the rms transverse beam sizes $\sigma_{x,y}$, in (e) the energy spread σ_E and in (f) the bunch length σ_z.

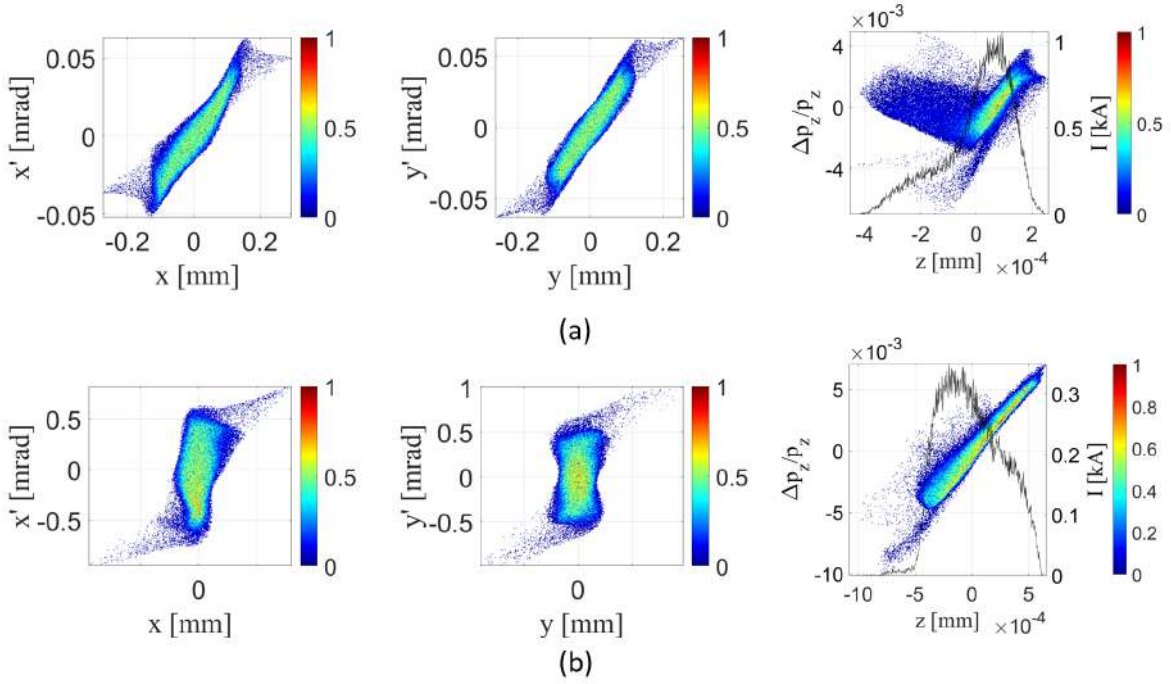

Figure 6.9.: Evolution of the transverse and longitudinal phase spaces for WP1 100 MeV electron beam, simulated in ASTRA, at (a) the BC exit and matched beam at (b) the entrance of the plasma cell. Color scales indicate normalized electron density.

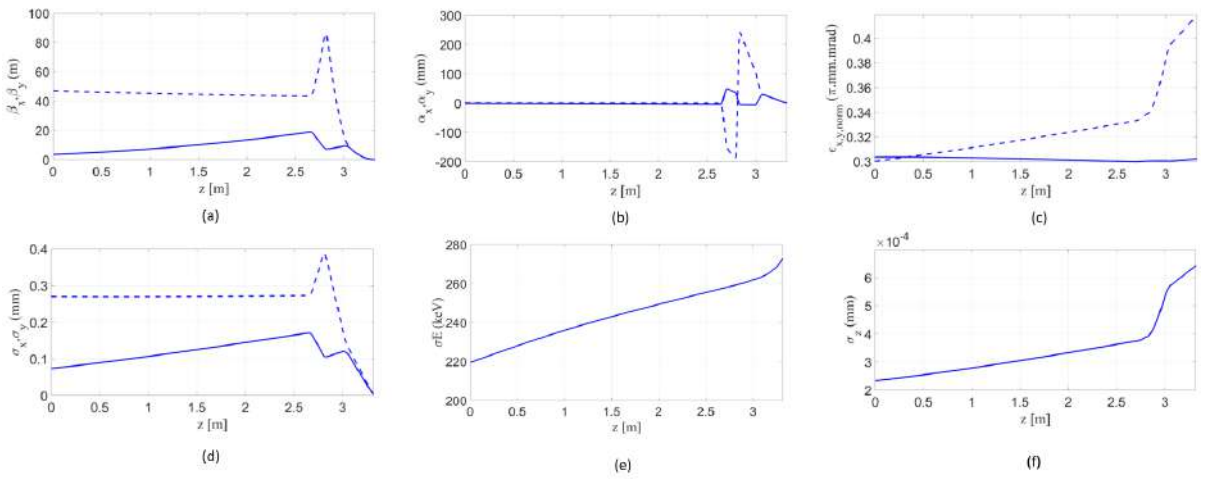

Figure 6.10.: Evolution of the electron beam parameters for WP2 100 MeV electron beam, simulated in ASTRA, along the beam line from the exit of the BC until the entrance of the plasma cell. The origin here is set at the exit of the last magnet of the BC. The parameters shown are the Twiss parameters in (a) $\beta_{x,y}$ and in (b) $\alpha_{x,y}$, in (c) the normalized transverse emittance $\varepsilon_{x,y}$, in (d) the rms transverse beam sizes $\sigma_{x,y}$, in (e) the energy spread σ_E and in (f) the bunch length σ_z.

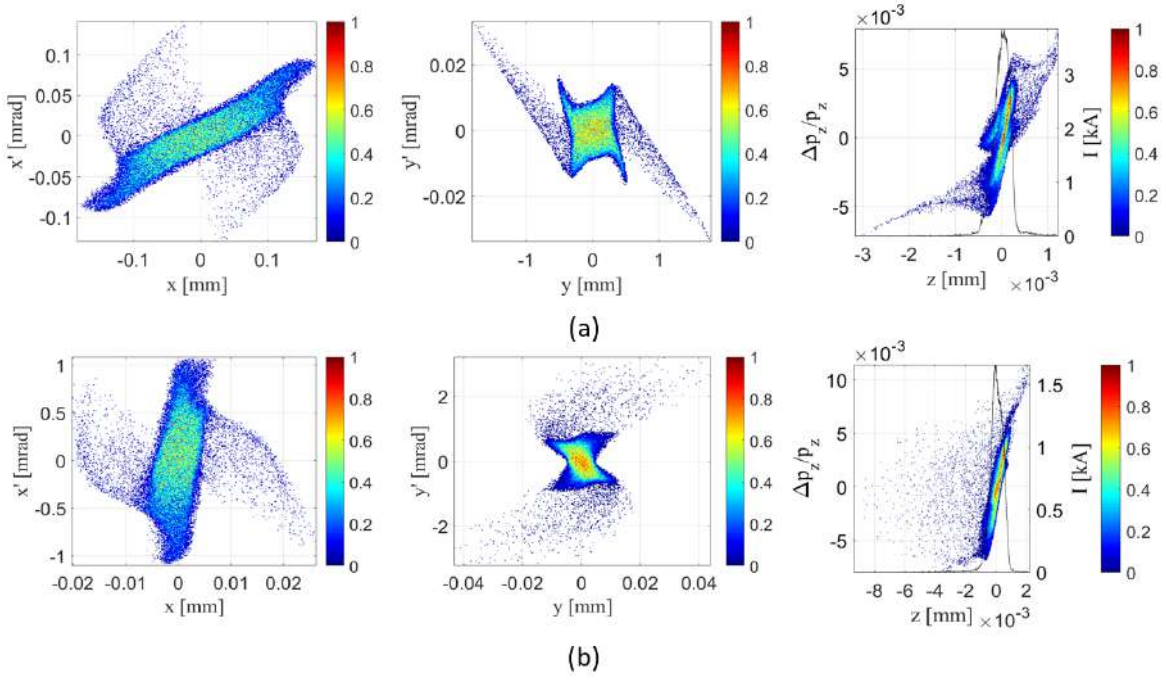

Figure 6.11.: Evolution of the transverse and longitudinal phase spaces for WP2 100 MeV electron beam, simulated in ASTRA, at (a) the BC exit and matched beam at (b) the entrance of the plasma cell. Color scales indicate normalized electron density.

BC exit till the entrance of plasma cell, without external focusing is shown in figure 6.12. The 3rd TW structure also gives a high tuning range of beam parameters in terms of bunch length and much lower energy spread. The lower energy spread is desirable to show stable LWFA with excellent beam quality. Also under the transnational access program of ARIES [14] [50], a certain fraction of ARES beam time will be available to user community for other experiments and the ARES energy upgrade with third TW structure enables to produce wide spectrum of parameters which have a wide range of applications in other fields of as well. The key parameters for the working points at the BC exit and at the entrance of the

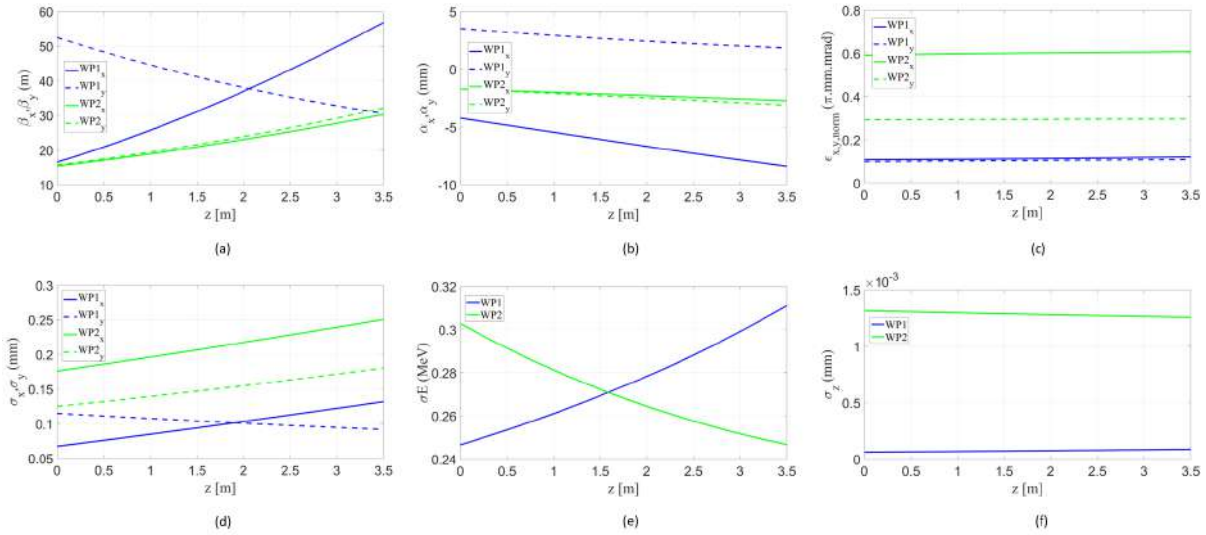

Figure 6.12.: Evolution of the electron beam parameters, without external focusing, for WP1 ARES energy upgrade, simulated in ASTRA, along the beam line from the exit of the BC until the entrance of the plasma cell. The origin here is set at the exit of the last magnet of the BC. The parameters shown are the Twiss parameters in (a) $\beta_{x,y}$ and in (b) $\alpha_{x,y}$, in (c) the normalized transverse emittance $\varepsilon_{x,y}$, in (d) the rms transverse beam sizes $\sigma_{x,y}$, in (e) the energy spread σ_E and in (f) the bunch length σ_z.

plasma cell, simulated in ASTRA, are summarized in Table 6.6. The full beam distribution is included in the calculation of statistical parameters. Figures 6.14 and 6.16 shows the evolution of the electron beam parameters, over the drift space and through the PMQ triplet from the BC to the plasma cell,for WP1 and WP2 respectively. It is evident that at the start of plasma ramp, the electron beam is well matched with preserved transverse emittance and bunch length shorter than the accelerating wavelength in the plasma. The transverse phase space distributions show that the beam is symmetric in both planes as required by LWFA. The PMQ triplet also ensures to maintain the current profile from the longitudinal phase space with $\sim$ kA of peak current to get useable beam quality after the plasma cell.

Detailed simulation studies on beam tracking in the experimental beamline through the PMQ triplet show that the optimized settings for the PMQ triplet provide a good quality working point. The electron beam can be transported and matched into the plasma cell with the PMQ triplet while preserving the beam quality. The transverse and longitudinal phase space distributions show good beam profiles for injecting into LWFA. The symmetric beam distributions with a peak current of $\sim$kA would be sufficient

Table 6.6.: Bunch Parameters at the BC exit (I), matched beam at the entrance of plasma cell (II) for ARES energy upgrade.

Parameters	**WP1**		**WP2**	
	I	**II**	**I**	**II**
Energy (MeV)	200	200	150	150
Bunch Charge (pC)	0.8	0.8	10	10
Bunch length-rms (fs)	0.20	0.24	4.38	4.30
ε_x (π.mm.mrad)	0.10	0.11	0.59	0.57
ε_y (π.mm.mrad)	0.098	0.11	0.29	0.31
β_x (mm)	16.6×10^3	2.8	15.32×10^3	118
β_y (mm)	52.65×10^3	2.8	15.66×10^3	119
α_x	-4.2	-0.2	-1.7	4.5
α_y	3.5	0.1	-1.7	4.4
σ_x (μm)	67.21	0.89	175.8	15.2
σ_y (μm)	114.79	0.91	124.9	11.2
RMS energy spread (%)	0.12	0.15	0.2	0.16
Peak Current (kA)	4	2	1	1

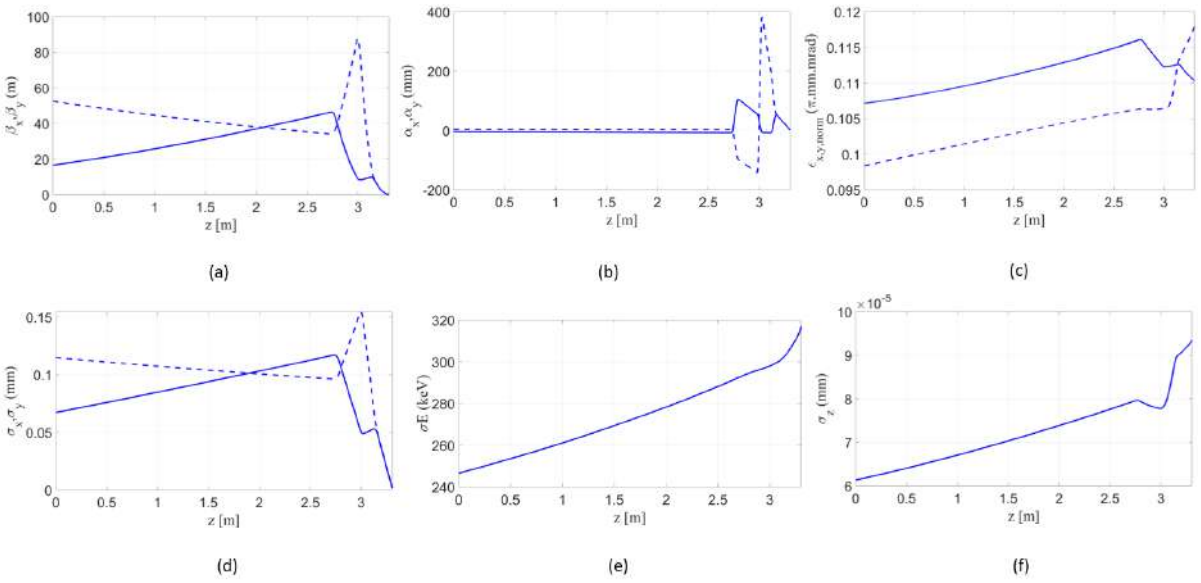

Figure 6.13.: Evolution of the electron beam parameters for WP1 ARES energy upgrade, simulated in ASTRA, along the beam line from the exit of the BC until the entrance of the plasma cell. The origin here is set at the exit of the last magnet of the BC. The parameters shown are the Twiss parameters in (a) $\beta_{x,y}$, in (b) $\alpha_{x,y}$, in (c) the normalized transverse emittance $\varepsilon_{x,y}$, in (d) the rms transverse beam sizes $\sigma_{x,y}$, in (e) the energy spread σ_E and in (f) the bunch length σ_z.

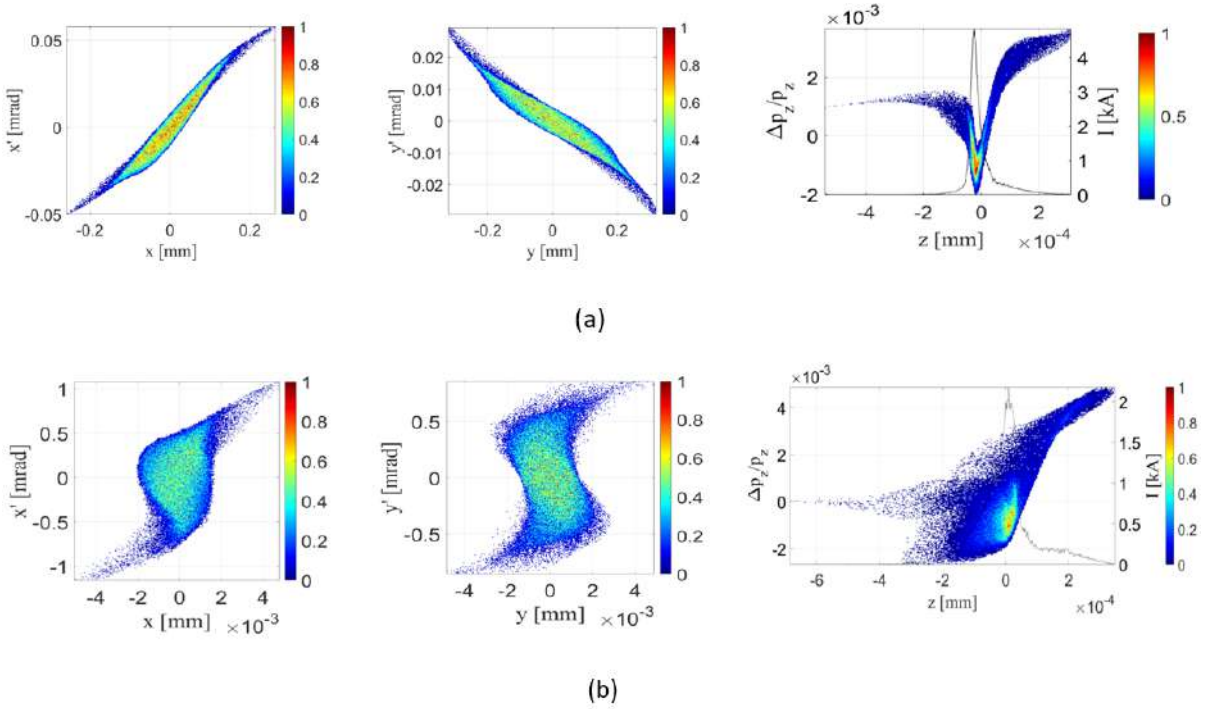

Figure 6.14.: Evolution of the transverse and longitudinal phase spaces for WP1 ARES energy upgrade, simulated in ASTRA, at (a) the BC exit and matched beam at (b) the entrance of the plasma cell. Color scales indicate normalized electron density.

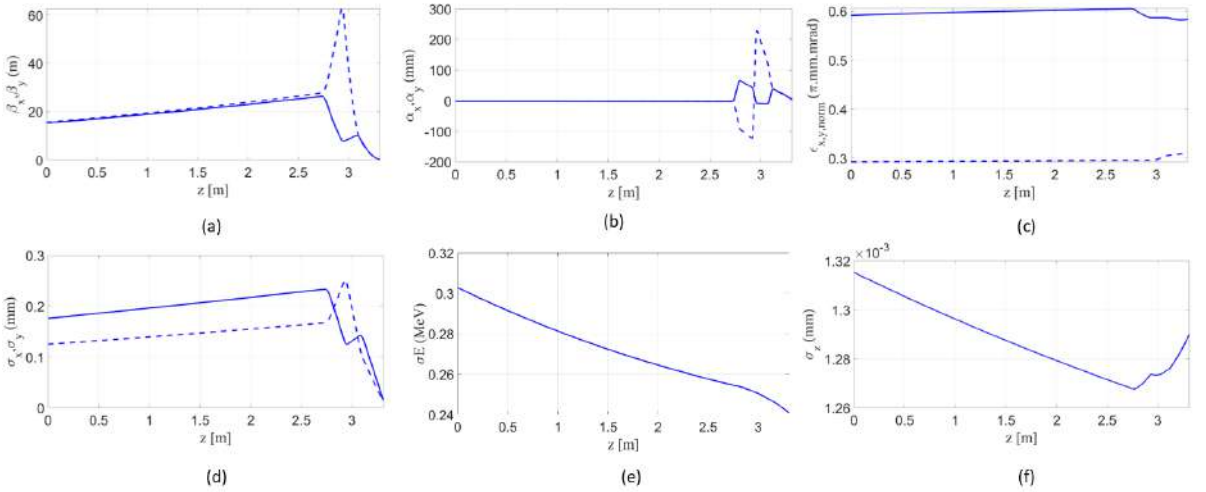

Figure 6.15.: Evolution of the electron beam parameters for WP2 ARES energy upgrade, simulated in ASTRA, along the beam line from the exit of the BC until the entrance of the plasma cell. The origin here is set at the exit of the last magnet of the BC. The parameters shown are the Twiss parameters in (a) $\beta_{x,y}$ and in (b) $\alpha_{x,y}$, in (c) the normalized transverse emittance $\varepsilon_{x,y}$, in (d) the rms transverse beam sizes $\sigma_{x,y}$, in (e) the energy spread σ_E and in (f) the bunch length σ_z.

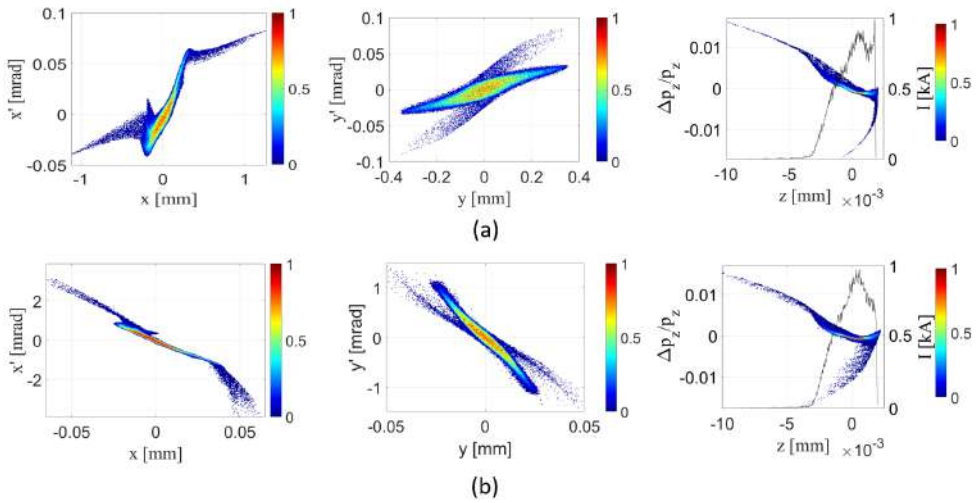

Figure 6.16.: Evolution of the transverse and longitudinal phase spaces for WP2 ARES energy upgrade, simulated in ASTRA, at (a) the BC exit and matched beam at (b) the entrance of the plasma cell. Color scales indicate normalized electron density.

for efficient beam loading [117, 118, 108] in the plasma cell.

6.8. Tolerance studies for the final focus system

The experimental conditions may vary from the ideal design parameters discussed in the previous sections due to temporal and spatial jitter in the beam. Moreover, there are additional sources of errors in the quadrupoles, arising during the manufacturing and installation of the final focus system. For example, offsets between the magnetic field center of the quadrupoles and the ideal beamline can lead to emittance growth and betatron oscillations in the plasma. A tolerance study for the final focus system was performed to estimate the effects of several error sources.

One set of errors can arise from spatial and temporal jitter in the electron beam. The other set of errors is introduced from positioning errors in the quadrupole triplet. In simulation parameters in the beam distribution after the bunch compressor were varied and analyzed. In addition, perturbations from transverse offsets x_{off} and y_{off} in the quadrupole triplets, from rotation errors x_{rot} in the x-z plane, from rotation errors y_{rot} in the y-z plane, from rotation errors z_{rot} in the x-y plane, from longitudinal offset errors z_{off} and from errors in the focusing strength K were included. The quadrupole parameters under study were varied within the given tolerances range. All quadrupoles were assigned the same error as one would realistically expect if errors arise from a common support girder and positioning system. For example, mounting errors between single elements on a common girder are usually much better corrected than offsets or drifts of the whole girder in the tunnel.

$$\Delta b_i = b_{i,ref} \pm b_{off} \, (\pm \, tol) \tag{6.8}$$

where $b_{i,ref}$ is the reference beam parameter at the exit of BC given in table 6.6 and b_{off} is the error in the beam parameter at the same location within the defined tolerance.

In addition, perturbations from transverse offsets x_{off} and y_{off} in the quadrupole triplets, from rotation errors x_{rot} in the x-z plane, from rotation errors y_{rot} in the y-z plane, from rotation errors z_{rot}t in the x-y plane, from longitudinal offset errors z_{off} and from errors in the focusing strength K were included. The quadrupole parameters under study were varied according to equation 6.9

$$A = A_{ref} \pm A_{off} \, (\pm \, tol) \tag{6.9}$$

where A represents an input parameter, A_{ref} is the design parameter of the quadrupole and A_{off} *(*$\pm$ *tol)* is the variation of the design parameter within the given tolerances range. All quadrupoles were assigned the same error as one would realistically expect if errors arise from a common support girder. For example, mounting errors between single elements on a common girder are usually much better corrected than offsets or drifts of the whole girder in the tunnel.

The range of variation is obviously different for each parameter. The transverse and longitudinal offsets were varied within $\pm$ 100 μm, rotational offsets within $\pm$ 100 μrad and the strength were varied by $\pm$10% of the design value. In both cases the variation of the final beam parameter at the entrance of plasma

cell with respect to reference case is calculated according to equation (6.10).

$$\Delta b_f = b_{f,ref} - b_f \tag{6.10}$$

where $b_{f,ref}$ is a final reference beam parameter given in table 3 and b_f are the beam parameters of the perturbed beam.

The observables in simulation include transverse normalized emittance, transverse beam sizes, beam divergence in both planes, Twiss parameters, bunch length and energy spread at the entrance of the plasma cell.

For doing the tolerance studies, the WP2 for the ARES energy upgrade was considered. The design parameters are shown in table 6.6. All parameters were varied one by one while keeping the others fixed to their design values. A total of 50 simulation cases were considered within the ranges mentioned above. The Pearson correlation coefficient was calculated by scanning one parameter in ASTRA and observing its impact on the output beam parameters. The Pearson correlation coefficient is a measure of the linear dependence of two variables. The value of the correlation coefficient ranges between -1 to +1. The range of correlation coefficient depicts *-1* in case of a perfect negative correlation, *0* as no correlation and *+1* of the perfect positive correlation of the two parameters. The correlation coefficient ρ *(A, B)* of two variables A and B is defined as

$$\rho\left(A,B\right) = \frac{cov\left(A,B\right)}{\sigma_A \sigma_B} \tag{6.11}$$

where *cov(A,B)* is the covariance of variables A and B, σ_A is the standard deviation of variable A and σ_B is the standard deviation of variable B.

The correlation matrix between the scanned input parameters and the final beam parameters is shown in figure 5. It can be observed that a response of the final beam parameters to changes in the input beam parameters such as transverse offset only occurs in the plane in which they occur. However, for the offsets in parameters of quadrupoles, it effects the final beam properties in both x and y plane. Since only the linear correlation coefficient was calculated, it is possible that some of the elements have quadratic correlations as well and hence not quite clear in the linear case. The biggest impact in the final beam properties is caused by the variation of the focusing strengths of the quadrupoles and the longitudinal positioning of quadrupoles in the beam line.

In the above analysis, the maximum variation was obtained by varying one parameter at a time, independent of another. However in a real beamline, all the parameters have variations at the same time. Hence in order to assess the robustness of the PMQ triplet solution, a simulation study was performed in which all the input parameters have simultaneous variations. 10000 cases were simulated in which each input parameter was randomly selected for the two cases

Mismatch case 1: Errors are randomly assigned to PMQ triplet and bunch parameters according to Gaussian distribution with mean being the matched design parameter and the cut off of the distribution

at the assigned tolerance. This includes 10 μm errors in bunch position at the BC exit and 10 % errors in beam size, bunch length and bunch charge. For the quadrupole triplet transverse and longitudinal offsets were varied within $\pm$ 10 μm, rotational offsets within $\pm$ 10 μrad and the strength were varied by $\pm$1% of the design value. The minimum tolerance range of 10 µm was chosen according to the precision range of hexapods which can be used for the positioning of the quadrupole triplet [119].

Mismatch case 2: A same set of simulations were carried out in which the tolerance range for transverse and rotational offset of quadrupole was 100 μm and 100 μrad respectively.

The position for observing the final beam parameters in both cases was fixed at the matched case position of table 6.6, which is the entrance of plasma cell as explained in section 6.5.3. Figure 6.18 summarizes the simulated beam parameters at the plasma entrance, as obtained in the two error cases. From figure 6.18, it can be concluded that the mismatch case 1 is an acceptable scenario, since the beam with this set of variations still enters the plasma cell well matched in the transverse plane with only a small increase in emittance. It is worthwhile to note again that this also includes the variation in input beam parameters. It can be safely inferred that the PMQ triplet design is robust and can be used for matching the electron beam to the plasma channel under less than ideal experimental conditions as well.

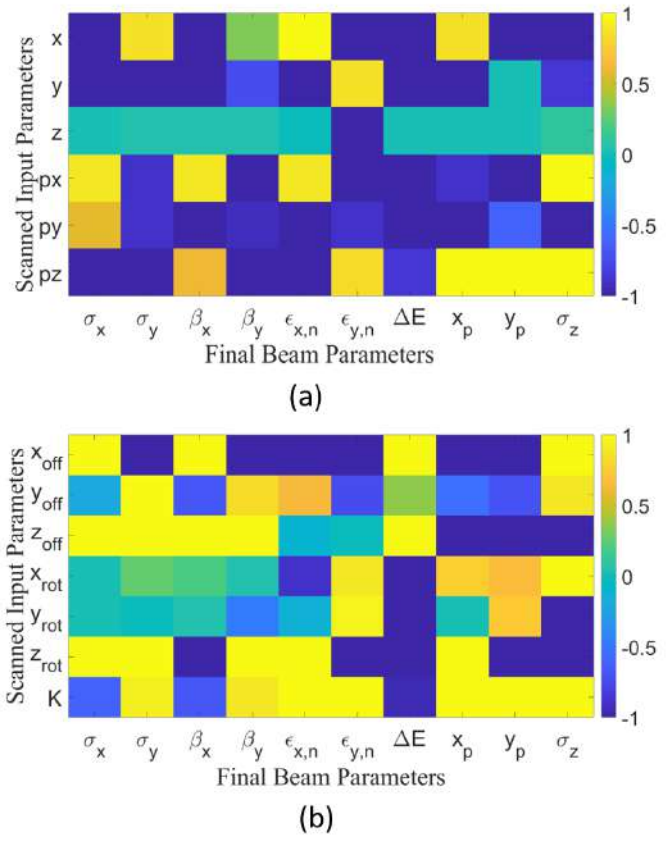

Figure 6.17.: The correlation matrix between (a) scanned input parameters of electron beam at the BC exit and the final beam parameters at the plasma cell entrance (b) scanned input parameters of the quadrupole and the final beam parameters. The color bar shows the strength of the correlation coefficient between the two variables.

Additional errors in the quadrupole triplet can arise during the manufacturing of the permanent magnets. Variations can occur from many sources such as the precision with which the magnetic blocks comprising them are constructed, both in geometry of the cutting of the blocks and in the magnitude and direction of their magnetic moments, as well as the geometrical constraints required to carefully assemble these blocks into a Halbach configuration. The peak gradient is difficult to precisely fabricate, however this can be achieved within 5% and precisely measure. This is followed by cutting the PMQ to the required length for the targeted strength [120]. The individual sources of errors are indirectly incorporated in the quadrupole strength which is included in the presented error analysis Hence as long as the targeted strength of the quadrupole is achieved after manufacturing, despite the manufacturing errors, the quadrupole triplet performance can be considered up to the design settings as in simulations. The assumed sources of errors considered are realistic with reasonable tolerances arising from physical positioning setup that can be used to build the quadrupole triplet [119] with ARES capable of delivering the beam within the given variation from the design values. The required tolerances are summarized in Table 6.7.

Table 6.7.: Maximum tolerable variations in the input parameters for the electron beam at the BC exit, passing through the PMQ triplet and in the PMQ triplet. The shown variations corresponds to the case when all other parameters are also varying from their design values within the variation range.

Parameters	Units	Tolerance range
Error from the beam		
bunch charge	pC	10%
transverse beam jitter in x and y	μm	10%
bunch size in x and y	μm	10%
bunch length	fs	10%
Error from the triplet		
transverse misalignment in x and y	μm	10
rotational misalignment of the quadrupole in the (x-z), (y-z) and (x-y) plane	μrad	10
longitudinal quadrupole position	mm	10%
effective length of the quadrupole	mm	10%
quadrupole strength	m^{-2}	1 %

There can be other sources of error critical for the experimental implementation like errors of the laser beam or the plasma itself. For example laser can fluctuate in energy, have a different spot size or can be off-axis to the plasma cell. Error of laser and plasma cell can translate into energy jitter and emittance growth effecting the performance of LWFA acceleration. To quantify the impact of these errors requires a detail study with large number of plasma simulations that are computationally expensive to perform. The aim of this PhD is to present the design of the final focus system implemented for the LWFA beam line, to effectively transport and focus the electron beam to the plasma cell. The simulated acceleration through the plasma [57] validates the design of the final focus system as the transported beam can be efficiently accelerated with usable beam quality after the plasma cell.

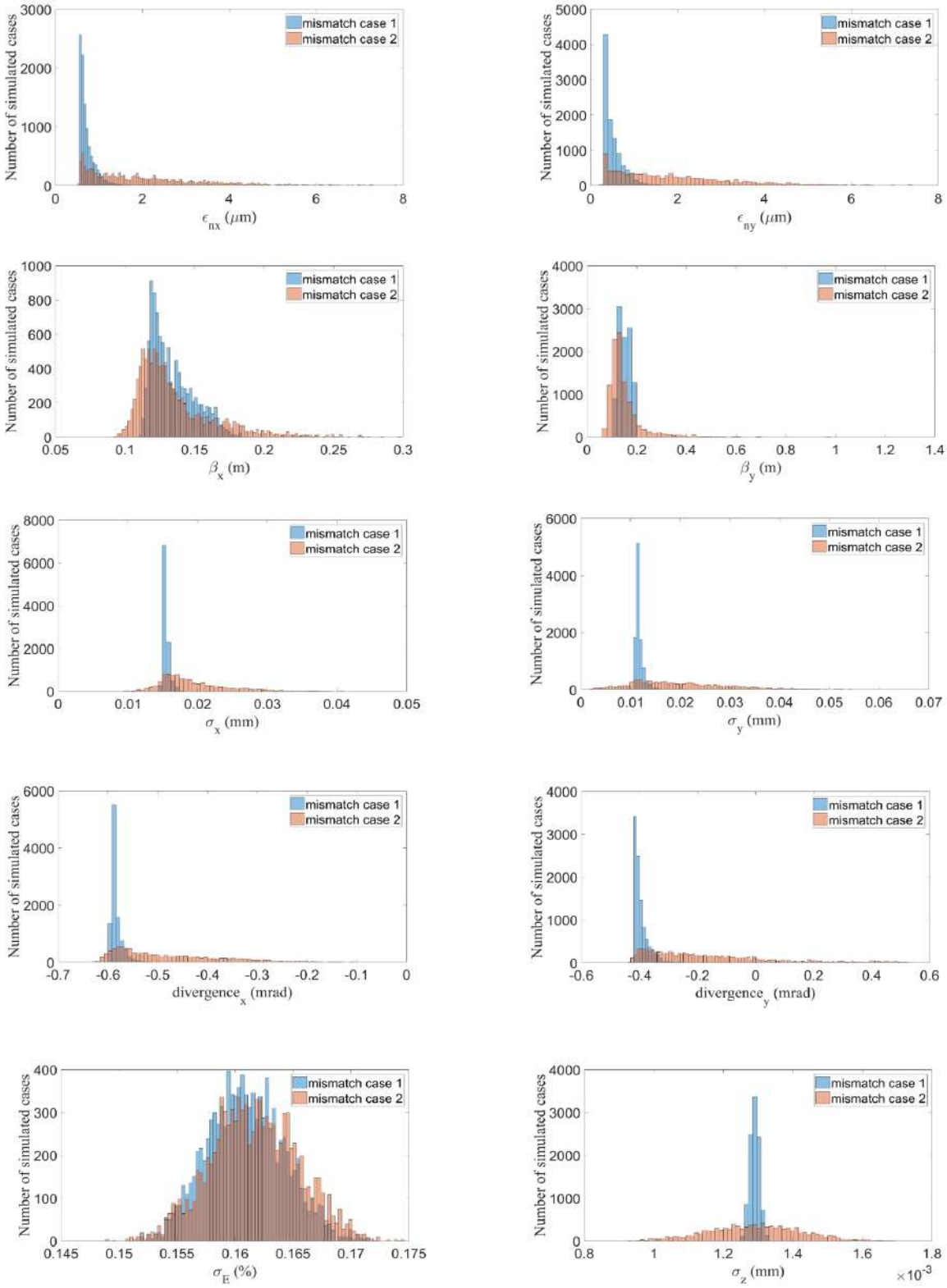

Figure 6.18.: Variation in observed beam parameters at the plasma entrance for the two error scenarios defined in the text (mismatch case 1 and 2) and each 10,000 random cases simulated.

6.9. Exploring the limits with electromagnetic quadrupoles

In section 6.5.2, two options for the choice of laser parameters were discussed, mainly having different beam waist. As can be seen from the Figure 6.6, for the same laser power, having a wider w_o makes the laser less intense, which leads to less strong accelerating and focusing fields in the plasma and therefore to less strong matching conditions. Also a wider w_o changes the divergence of the laser which inturn relaxes the space constraints for the matching lattice. This allows more space in longitudinal plane for positioning the lattice. Hence longer and less stronger magnets can be used to achieve same electron beam configuration at the plasma entrance. Moreover, from section 6.5.3 the matching criterion can be considerably relaxed by using long tailored plasma ramps. Combining these two design features, namely wider spot size and longer plasma ramps with $\beta_{x,y} = 11.8cm$, gives us the freedom to explore the possibility of using electromagnetic quadrupole for matching beam into the plasma cell.

The specifications of ElectroMagnetic Quadrupoles (EMQ) available in the DESY magnet group were thoroughly reviewed and three potential candidates were selected for the matching studies. These includes quadrupoles named XQA used for XFEL facility, TQG used for FLASH and SQA used for SINBAD. All three of them have high gradients and relatively shorter lengths to fit in the matching beam line along with the laser beam line. The specifications for the aforementioned three quadrupoles are given in Table 6.8 and are shown in Figure 6.19.

Table 6.8.: Specifications of electromagnetic quadrupoles available on DESY campus.

Design Parameters \Magnet Type	**XQA**	**TQG**	**SQA**
Aperture radius (mm)	8	7.5	20
Gradient (T/m)	100	45	40
Iron length (mm)	100	120	100
Magnetic length (mm)	107	125	122
Total length (mm)	237	126	200
Nominal current (A)	140	75	300

Figure 6.19.: Electromagnetic quadrupoles with highest gradients available with the DESY magnet group.

The simulations were setup to transport the 10 pC, 150 MeV working point of ARES, using an electromagnetic quadrupole triplet with specifications given in Table 6.8. With the XQA, it was possible to match the beam but the total length of the beamline increase up to 4m, which is not consistent with the

laser beamline, hence this option was dropped. Using the combination of TQG and XQA as a quadrupole triplet, the beam was successfully transported and matched to the plasma cell. The matched beam parameters, of WP2 for ARES energy upgrade, are given in Table 6.9 and compared with the parameters matched with the PMQ and the EMQ triplet settings is given in Table 6.10. The total length of triplet is $\sim$ 1 m which can fit it the beam line for wider w_o. The EMQ triplet settings for the WP's of ARES are given in Appendix . The comparison of matched beam parameters with EMQ and PMQ is also given in Appendix . Here it should be noted that the use of EMQ is only possible if Laser beam parameters i-e divergence and focal spot size allows enough space to use EMQ triplet. Also the laser beam has to pass through the EMQ's. The apertures of the EMQ's should be big enough to take into account tails of the Laser distribution with allowance for the jitter plus at least 1-2 mm for the vacuum pipe wall thickness. In summary the trade off in the matching beam line for using EMQ's is the compromise between using longer longitudinal plasma density profile and wider w_o, leading to less stronger accelerating and focusing fields in the plasma, and therefore to less strong matching conditions but a longer plasma cell to achieve the same final energy.

Table 6.9.: Comparison of matched beam parameters at the entrance of plasma cell with PMQ and EMQ.

Parameters	**EMQ**	**PMQ**
Energy (MeV)	150	150
Bunch Charge (pC)	10	10
Bunch length-rms (fs)	4.27	4.30
ε_x (π.mm.mrad)	0.5	0.57
ε_y (π.mm.mrad)	0.3	0.31
β_x (cm)	11.9	11.8
β_y (cm)	11.9	11.9
α_x	4.4	4.5
α_y	4.2	4.4
σ_x (μm)	15.2	15.2
σ_y (μm)	11.3	11.2
RMS energy spread (%)	0.15	0.16
Peak Current (kA)	1	1

Table 6.10.: EMQ triplet settings for matching the WP2 for ARES energy upgrade

Parameters	**Quadrupole 1**	**Quadrupole 2**	**Quadrupole 3**
Quadrupole Type	SQA	SQA	TQG
Aperture radius (mm)	20	20	7.5
Magnetic Length (mm)	122	122	125
Length of EMQ (mm)	200	200	126
Gradient (T/m)	10.96	26.40	34.57
Current (A)	73.89	30.68	96.75
Drift length between magnets (mm)	200	110	100

6.10. Conclusion

In this Chapter,the design for a final focus system, an experimental beamline for a LWFA with external injection has been developed for the ARES linac in the SINBAD facility at DESY. Detailed numerical simulations show that the electron beam can be transported and focused to a plasma cell. The studies include the effects of SC. SC plays a significant role and deteriorate beam quality in the beamline after the BC when beam is compresses to achieve desired bunch length. After the final focus system, the electron beam has adequate transverse symmetry and is well matched into a plasma channel using plasma ramps. The longitudinal phase space is preserved with a 1 kA peak current, as approaching the requirements for several use cases. We have performed a sensitivity analysis of the PMQ triplet for understanding the tolerances and to mitigate the effect of imperfections of the final focus system. The performed error analysis, which could be generalized for any quadrupole triplet, gives a useful estimate about the performance of the final focus system and suggests critical parameters in the implementation of the experiment. The most significant error is the quadrupole strength and the longitudinal positioning of the quadrupole triplet as this changes the focusing properties of the triplet. The main focus of ARES is the generation and characterization of ultra-short pulses and as test bench for laser based novel external injection acceleration concepts. The beamline is currently under construction. A step wise commissioning plan will be executed until mid 2024 [20]. Meanwhile the scientific direction of ARES will be consistently investigated and reviewed. The aim of this thesis is to present the design of the final focus system which fulfills the matching criterion for LWFA experiment within the defined constraints. Plasma simulations validates the design studies as demonstrated in [57]. The design constraints are in general typical to any LWFA experiment with external injection of electron beam. Matching criterion depends mostly upon the laser and plasma parameters. The design studies for the final focus system and the error analysis, presented can be generalized and adopted for any LWFA experiment with external injection of electron beam. There can be other sources of errors critical for the experimental implementation like errors of the laser beam or the plasma itself. For example laser can fluctuate in energy, have a different spot size or can be off-axis to the plasma cell. Error of laser and plasma cell can translate into energy jitter and emittance growth effecting the performance of LWFA acceleration. To quantify the impact of these errors is a research topic in itself and requires a detail study with large number of plasma simulations that are computationally expensive to perform. Possible sources of error arising from the electron beam and the final focus system have been studied in detail. A plasma simulation shows that external injection of short electron bunches into a LWFA at ARES can achieve high beam quality and can constitute a stepping stone towards a staged multi GeV high performance plasma accelerator.

7

Conclusion

The performance of modern particle accelerators often requires very small dimensions of the beam. Small transverse beam size increase the beam brightness or luminosity. Short bunches allow access to ultra-fast science, e.g. freezing moving processes. In terms of accelerators we aim at electron beams with small transverse emittance (sub-micron radian) and ultra-short duration (around few femto-second and below). Such beams can also be used for developing novel acceleration schemes with dimensions of the accelerating volume in the 10's of micrometer regime and below, e.g. dielectric or plasma accelerators. The new ARES linear accelerator at DESY provides such beams.

In this work, the required optimization of the high quality beam transport during commissioning of the ARES linac is presented. The electron beam from the photoinjector of ARES was optimized by performing beam based alignment of the focusing solenoid in the ARES RF gun and of the solenoids around the travelling wave structures. An alignment algorithm based on linear transfer matrices of the ARES beamline elements was developed for this purpose. The performance of this alignment algorithm was evaluated against ASTRA simulations. Possible sources of errors in the ARES beam line and their impacts in determining the misalignment were investigated and are discussed. Moreover, a user interface was developed in Matlab for use in the various alignment campaigns during ARES commissioning. The algorithm was successfully used to correct the trajectory of the ARES beam through iterative alignment of the solenoids. This beam-based alignment of the focusing solenoid was a centrally important part of the successful commissioning of the ARES linac. Generating low emittance electron beams from a photo injector and preserving it during beam transport in accelerating cavities is strongly affected by the alignment of the beamline elements. Off-axis beam in a magnetic focusing field induces an additional kick and can lead to emittance dilution and growth. We developed and implemented an optimization method at ARES which is simple and efficient. It gives reliable and reproducible results within the accuracy of the solenoid micro-mover system. The developed beam-based alignment algorithm is generic and can be adapted for any accelerator facility that uses focusing solenoids.

As part of this thesis work a design for a final focus system has been developed for the ARES linac. This final focus system is aimed at external injection of a small emittance, ultra-short electron bunch into a laser

wakefield acceleration experiment. ARES had been designed to provide ultrashort high brightness electron beams for injection into novel accelerators. The full width half maximum length of electron bunches is expected to reach a few femto-second and potentially sub femto-second values. The ARES concept relies on an electron gun, on a conventional radio frequency accelerator and on bunch compression schemes for producing such electron bunches. This has several advantages. The ARES linac on one hand will allow advancing R&D on the "conventional" production of high brightness ultra-short electron bunches. On the other hand, the well-characterized bunches can be used to explore compact novel accelerators, characterized by accelerating fields with short wavelengths and therefore require the injection into short "acceleration buckets". Detailed numerical simulations of the developed final focus system show that the ARES electron beam can indeed be transported and focused to a plasma cell. The studies performed include the effects of SC. SC plays a significant role and deteriorates the beam quality in the beamline after the bunch compression area of ARES. After the final focus system, developed in this thesis, the electron beam has adequate transverse symmetry and is well matched into a plasma channel with plasma ramps. The longitudinal phase space is preserved with a 1 kA peak current, approaching the requirements for several use cases. We have performed a sensitivity analysis of the PMQ triplet for understanding the tolerances to unavoidable imperfections, also investigating possible mitigation measures against the effect of imperfections on the final focus system. The performed error analysis gives a useful estimate about the realistically achievable performance of the final focus system and suggests critical parameters for the implementation and optimization of the experiment. The most sensitive error identified in this thesis, is the quadrupole strength and the longitudinal positioning of the quadrupole triplet as this changes the focusing properties of the triplet. The design constraints are in general typical to any LWFA experiment with external injection of electron beams. The matching criterion depends mostly upon the laser and plasma parameters. The presented design studies for the final focus system and the error analysis can be generalized and adopted for a typical LWFA experiment with external injection of electron beam at other facilities. A plasma simulation shows that external injection of short electron bunches into a laser-wakefield experiment at ARES can achieve high beam quality and can constitute a stepping stone towards the understanding and implementation of a staged multi GeV high performance plasma accelerator.

The work performed during the course of this PhD played a major role for achieving important commissioning goals with electron beam in the new ARES accelerator at DESY. The beam-based alignment campaigns for the ARES focusing solenoids were particularly important for the successful commissioning as well as for beam operation. The design of a ARES final focus system prepares possible future experiments and is an important contribution for the development of novel high-gradient acceleration schemes with externally injected electron beams. Further work at ARES will need to commission the bunch compression schemes with the optimized solenoid positions and beam prepared in this thesis, and will need to verify the predicted performance with a new diagnostics system for ultra-short bunches.

A

Transfer Matrix of a Solenoid

In this section, the transfer matrix of a solenoid, used for developing the algorithm for BBA of solenoid at ARES in chapter 4, is derived.

Consider a solenoid magnet of length l with N turns carrying current I. The magnetic field, according to Ampere's law is given by

$$\oint \overrightarrow{B} \cdot \overrightarrow{dl} = \mu_o I_{enclosed}$$
$$B_z = \mu_o \frac{NI}{l} \tag{A.1}$$

According to Maxwell's equation,

$$\oint \overrightarrow{B} \cdot \overrightarrow{ds} = 0 \tag{A.2}$$

Splitting the magnetic field into changing radial and constant longitudinal magnetic field inside the body of solenoid leads to

$$B_z = \mu_o \pi r^2 + 2\pi r \int B_r.dz = 0$$
$$\int B_r.dz = -\frac{r}{2} B_z$$
$$B_r = -\frac{r}{2} B'_z \tag{A.3}$$

A solenoid can be considered as a three piece process:

- entry region: action of radial field
- Body of solenoid: action of longitudinal magnetic field
- exit region: action of radial field

Equation of motion of a charged particle in a solenoid magnetic field evolves as follows.

$$\frac{d\overrightarrow{p}}{dt} = q\overrightarrow{v}\, x \overrightarrow{B} \tag{A.4}$$

which then yields

$$\begin{aligned} \frac{dp_\theta}{dt} &= qv_z B_r \\ \frac{dp_\theta}{dz}\frac{dz}{dt} &= qv_z\left(-\frac{r}{2}\frac{dB}{dz}\right) \\ \frac{dp_\theta}{dz} &= \left(-\frac{qr}{2}\frac{dB}{dz}\right) \\ \Delta p_\theta &= \left(-\frac{qr}{2}\frac{dB}{dz}\right) \end{aligned} \tag{A.5}$$

and

$$\begin{aligned} \Delta p_x = -\Delta p_\theta sin\theta = \frac{qr}{2}B_z sin\theta \\ \Delta p_x = \frac{qB_z}{2}y \end{aligned} \tag{A.6}$$

The divergence of the charge particle inside the solenoidal field, using equation A.8 can be written as

$$\Delta x' = \frac{\Delta p_x}{p_z} = \frac{qB_z}{2p_z}y \tag{A.7}$$

which can be written as

$$\begin{aligned} \Delta x' &= Ky \\ \Delta y' &= -Kx \end{aligned} \tag{A.8}$$

where $K = qB_z/2p_z = B_z/2B\rho$ is defined as the strength of the solenoid magnet with $B\rho$ being the beam rigidity (as defined in equation 2.38). The 4D transfer matrix in the two transverse plane for the entry and exit region is written as

$$\begin{aligned} M_{entry} &= \begin{pmatrix} 1 & 0 & 0 & 0 \\ 0 & 1 & K & 0 \\ 0 & 0 & 1 & 0 \\ -K & 0 & 0 & 1 \end{pmatrix} \\ M_{exit} &= \begin{pmatrix} 1 & 0 & 0 & 0 \\ 0 & 1 & -K & 0 \\ 0 & 0 & 1 & 0 \\ K & 0 & 0 & 1 \end{pmatrix} \end{aligned} \tag{A.9}$$

In the body of the solenoid, the magnetic field is constant along the z-axis with circular motion in the x-y plane. The total rotation angle θ over the length of the solenoid l is

$$\theta = \omega t = -\frac{qB_z}{m}\frac{l}{v_z} = -B_z l\frac{q}{p_z} = -\frac{B_z l}{B\rho} = -2Kl \tag{A.10}$$

Using basic trigonometry, the position transformations can be written as following.

$$\begin{aligned} x_f &= x_i + \Delta x \\ x_f &= x_i + \rho_\theta \left(cos\left(\phi + \theta\right) - cos\phi\right) \\ x_f &= x_i + \rho_\theta \left(cos\phi\left(cos\theta - 1\right) - sin\phi sin\theta\right) \\ x_f &= x_i + \rho_\theta \left(y_i' \frac{1}{\rho_\theta}\frac{l}{\theta}\left(cos\theta - 1\right) + x_i' \frac{1}{\rho_\theta}\frac{l}{\theta} sin\theta\right) \\ x_f &= x_i + x_i' \frac{l}{\theta} sin\theta - y_i' \frac{l}{\theta}\left(1 - cos\theta\right) \end{aligned} \tag{A.11}$$

where

$$\begin{aligned} cos\phi &= \frac{v_{yi}}{v_\theta} = \frac{v_{yi}}{v_z}\frac{v_z}{v_\theta} = y_i' \frac{1}{\rho_\theta}\frac{l}{\theta} \\ sin\phi &= -\frac{v_{xi}}{v_\theta} = -\frac{v_{xi}}{v_z}\frac{v_z}{v_\theta} = -x_i' \frac{1}{\rho_\theta}\frac{l}{\theta} \end{aligned} \tag{A.12}$$

has been used. Similarly, the position transformation in y gives

$$\begin{aligned} y_f &= y_i + \Delta y \\ y_f &= y_i + \rho_\theta \left(sin\left(\phi + \theta\right) - sin\phi\right) \\ y_f &= y_i + \rho_\theta \left(sin\phi\left(cos\theta - 1\right) + sin\phi sin\theta\right) \\ y_f &= y_i + \rho_\theta \left(-x_i' \frac{1}{\rho_\theta}\frac{l}{\theta}\left(cos\theta - 1\right) + y_i' \frac{1}{\rho_\theta}\frac{l}{\theta} sin\theta\right) \\ y_f &= y_i + y_i' \frac{l}{\theta}\left(1 - cos\theta\right) + y_i' \frac{l}{\theta} sin\theta \end{aligned} \tag{A.13}$$

The angle transformation is given by

$$\begin{aligned} x_f' &= x_i' cos\theta - y_i' sin\theta \\ y_f' &= x_i' sin\theta + y_i' cos\theta \end{aligned} \tag{A.14}$$

The position and angle transformation gives the body transfer matrix as

$$M_{entry} = \begin{pmatrix} 1 & \frac{l}{\theta} sin\theta & 0 & -\frac{l}{\theta}\left(1 - cos\theta\right) \\ 0 & cos\theta & 0 & -sin\theta \\ 0 & \frac{l}{\theta}\left(1 - cos\theta\right) & 1 & \frac{l}{\theta} sin\theta \\ 0 & sin\theta & 0 & cos\theta \end{pmatrix} \tag{A.15}$$

where $\theta = -2Kl$ and K has the same sign as qB_z. The total transfer matrix for a solenoid is given by

the product of entry, body and exit matrices.

$$M_{sol} = M_{exit} \cdot M_{body} \cdot M_{entry} =$$

$$M_{sol} = \begin{pmatrix} cos^2(Kl) & \frac{sin(Kl)cos(Kl)}{K} & sin(Kl)cos(Kl) & \frac{sin^2(Kl)}{K} \\ -Ksin(Kl)cos(Kl) & cos^2(Kl) & -Ksin^2(Kl) & sin(Kl)cos(Kl) \\ -sin(Kl)cos(Kl) & \frac{-sin^2(Kl)}{K} & cos^2(Kl) & \frac{sin(Kl)cos(Kl)}{K} \\ Ksin^2(Kl) & -sin(Kl)cos(Kl) & -Ksin(Kl)cos(Kl) & cos^2(Kl) \end{pmatrix} \quad (A.16)$$

It is worth mentioning that the determinant of 2x2 diagonal matrix M_{xx} and M_{yy} are not equal to 1. This implies that the xx' and yy' emittances are not preserved in a solenoidal field. Also the M_{xy} and M_{yx} matrices are non null indicating that the transvers motion in x and y plane inside a solenoid is coupled.

The transfer matrix in equation A.16 can be rewritten as a global focusing matrix in both xx' and yy' planes and a rotation matrix of phase spaces.

$$M_{sol} = M_{rotation} \cdot M_{focusing} \quad (A.17)$$

where

$$M_{rotation} = \begin{pmatrix} cos(Kl) & 0 & sin(Kl) & 0 \\ 0 & cos(Kl) & 0 & sin(Kl) \\ -sin(Kl) & 0 & cos(Kl) & 0 \\ 0 & -sin(Kl) & 0 & cos(Kl) \end{pmatrix}$$

$$M_{focusing} = \begin{pmatrix} cos(Kl) & \frac{sin(Kl)}{K} & 0 & 0 \\ -Ksin(Kl) & cos(Kl) & 0 & 0 \\ 0 & 0 & cos(Kl) & \frac{sin(Kl)}{K} \\ 0 & 0 & -sin(Kl) & cos(Kl) \end{pmatrix} \quad (A.18)$$

Thus a solenoid focuses in both transverse planes and a rotation of xy space of angle Kl.

B

Specifications of the Final Focus System

Table B.1.: PMQ triplet specifications as final focus system for LWFA working points of ARES.

	ARES baseline energy		ARES energy upgrade	
Parameters (Units)	**WP1**	**WP2**	**WP1**	**WP2**
K_1 (m^{-2})		65.284		
K_2 (m^{-2})		-151.730		
K_3 (m^{-2})		64.186		
z_1 (m)	2.6741	2.6741	2.70	2.7220
z_2 (m)	2.8401	2.8149	2.8770	2.8808
z_3 (m)	3.0650	3.0354	3.0923	3.1057
z_{plasma} (m)		3.305		

Table B.2.: EMQ triplet settings as final focus system for LWFA working points of ARES.

Parameters	**Quadrupole 1**	**Quadrupole 2**	**Quadrupole 3**
Quadrupole Type	SQA	SQA	SQA
Aperture radius (mm)	20	20	20
Magnetic Length (mm)	122	122	122
Length of EMQ (mm)	200	200	200
Drift length between magnets (mm)	200	110	100
		ARES baseline energy	
		WP1	
Gradient (T/m)	7.796	-18.556	26.943
Current (A)	58.269	-139.1737	202.0725
		WP2	
Gradient (T/m)	7.796	-18.314	27.355
Current (A)	58.470	-137.355	205.162
		ARES energy upgrade	
		WP1	
Gradient (T/m)	15.90	-36.20	49.56
Current (A)	119.25	-271.5	371.7
		WP2	
Gradient (T/m)	10.96	-26.40	34.57
Current (A)	82.2	-198	259.27

It should be noted that for WP1 using 3 TWS, the required gradient is bigger then the design value. However, according to equation (B.1) the gradient of a quadrupole for a given number of Ampere-turns

goes with the r^{-2}. Hence, by reducing the aperture of the third quadrupole of the triplet, the design of the SQA magnet could be easily modified to achieve the higher gradients [121].

$$G = \frac{2\mu_o NI}{r^2} \tag{B.1}$$

where G is the gradient of the quadrupole, r is the aperture i-e radius of quadrupole from center to the pole tip, NI is the Ampere-turns and μ_o is the permeability of free space. By reducing the aperture from 20 mm to 17.88 mm, a gradient of 50 T/m can be achieved. The technical drawings for SQA magnets were developed by magnet group, MEA at DESY. The iron yoke and coil were manufactured at Efremov – Institute , St. Petersburg, Russia. The drawings can be amended at DESY to achieve the target gradient of 50 T/m for the last quadrupole of the triplet. This could be done in two ways. Either the pole length should be increased to decrease the aperture. Alternatively, external shims can be added on top of the pole. Addition of external shims is a more commonly adopted practice to alter the gradient and increase the field quality. A similar scheme has been adopted for LUX experiment at DESY for increasing the quadrupole gradient from 100 T/m to 140 T/m for optimization of beam transport [122]. The use of existing quadrupoles to design a final focus system saves time and resources without compromissing on the achieveable beam quality at the injection of the plasma cell.

C

Magnetic Modeling of a Halbach PMQ triplet in CST

Since the maximum achievable gradient of a PMQ strongly depends on the diameters of the quadrupole, 3D modeling and numerical analysis of Halbach PMQ was done in CST to see the effect of finite length and inner and outer radii and to set the limits on maximum achievable gradients for PMQ design optimization. The segmentation of PMQ in a number of sections may also have an effect on the gradient of PMQ. Figure C.1 gives the numerical analysis of 16 piece Halbach geometry, with inner radius of 5 mm, outer radius of 12.5 mm and length of 30 mm. The theoretically achievable gradient is 292 T/m while CST simulations gives a gradient of 275 T/m. This corresponds to decrease in gradient of around 6% of the theoretically predicted value.

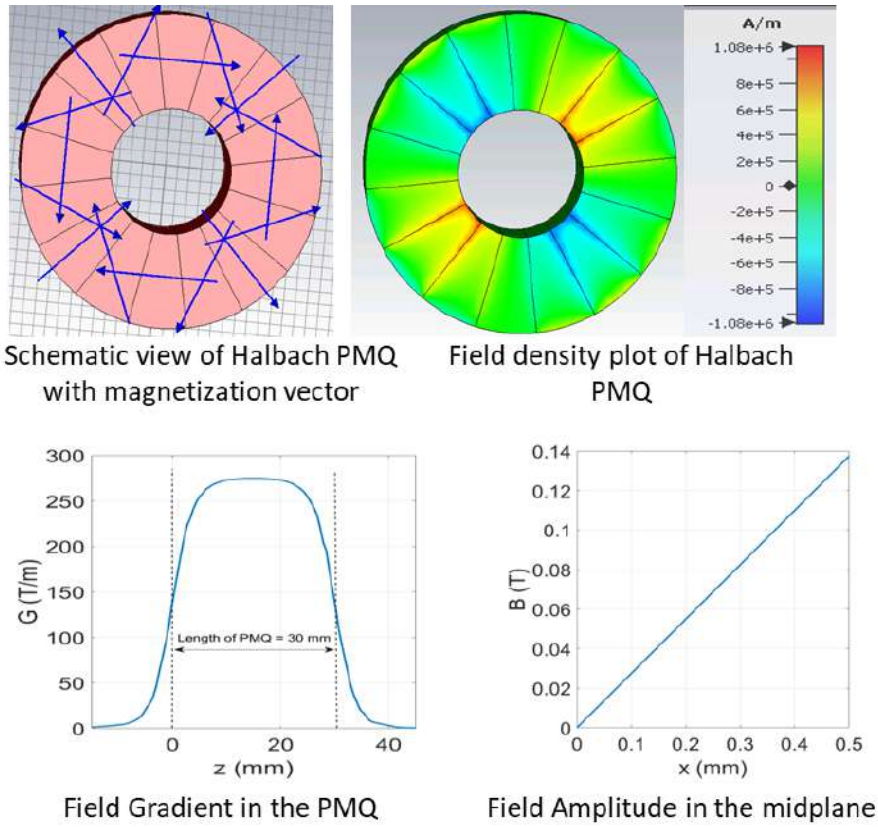

Figure C.1.: CST simulations of PMQ. Top figure shows the direction of magnetization and the corresponding field density plot. The bottom figure gives the maximum achievable gradient and field amplitude of a Halbach type PMQ with 12 sections and inner radius of 5 mm.

References

[1] T. P. Wangler. *RF linear accelerators; 2nd, compl. rev. and enl.* Physics textbook. Wiley-VCH, Weinheim, 2008.

[2] CERN, `https://home.cern/`.

[3] R. Abela, et al. *XFEL: The European X-Ray Free-Electron Laser - Technical Design Report.* DESY, Hamburg, 2006.

[4] Accelerotors at DESY, `https://accelerators.desy.de/`.

[5] R. J. England, et al. Dielectric laser accelerators. *Rev. Mod. Phys.*, 86:1337–1389, Dec 2014.

[6] T. Tajima and J. M. Dawson. Laser electron accelerator. *Phys. Rev. Lett.*, 43:267–270, Jul 1979.

[7] E. A. Peralta, et al. Demonstration of electron acceleration in a laser-driven dielectric microstructure. *Nature*, 503:91, November 2013.

[8] J. Breuer and P. Hommelhoff. Laser-based acceleration of nonrelativistic electrons at a dielectric structure. *Phys. Rev. Lett.*, 111:134803, Sep 2013.

[9] W. P. Leemans, et al. GeV electron beams from a centimetre-scale accelerator. *Nature Physics*, 2:3909–3912, 2006.

[10] M. Litos, et al. 9 GeV energy gain in a beam-driven plasma wakefield accelerator. *Plasma Physics and Controlled Fusion*, 58(3):034017, feb 2016.

[11] D. Cesar, et al. Enhanced energy gain in a dielectric laser accelerator using a tilted pulse front laser. *Opt. Express*, 26(22):29216–29224, Oct 2018.

[12] A. J. Gonsalves, et al. Petawatt Laser Guiding and Electron Beam Acceleration to 8 GeV in a Laser-Heated Capillary Discharge Waveguide. *Physical Review Letters*, 122(084801):1–6, 2019.

[13] J. Grebenyuk, et al. Laser-Driven Acceleration with External Injection at SINBAD. In *Proc. of International Particle Accelerator Conference (IPAC'14), Dresden, Germany, 15-20 June, 2014*, pages 1515–1518, Geneva, Switzerland, 2014. JACoW.

[14] U. Dorda, et al. Status and objectives of the dedicated accelerator R&D facility SINBAD at DESY. *Nuclear Inst. and Methods in Physics Research, A*, 909:239–242, February 2018.

[15] F. Mayet, et al. Simulations and Plans for Possible DLA Experiments at SINBAD. *Nuclear Inst. and Methods in Physics Research, A*, 909:1–4, February 2018.

[16] B. Marchetti, et al. Conceptual and Technical Design Aspects of Accelerators for External Injection in LWFA. *Applied Sciences*, 8(5), 757:1–30, May 2018.

[17] F. Kärtner, et al. Axsis: Exploring the frontiers in attosecond x-ray science, imaging and spectroscopy. *Nuclear Instruments and Methods in Physics Research Section A: Accelerators, Spectrometers, Detectors and Associated Equipment*, 829:24 – 29, 2016. 2nd European Advanced Accelerator Concepts Workshop - EAAC 2015.

[18] LASER PLASMA DRIVEN LIGHT SOURCES. `https://lux.cfel.de/`.

[19] E. Panofski et al. Status Report of the SINBAD-ARES RF Photoinjector and LINAC Commissioning. In *Proc. 10th International Particle Accelerator Conference (IPAC'19), Melbourne, Australia, 19-24 May 2019*, number 10 in International Particle Accelerator Conference, pages 906–909, Geneva, Switzerland, Jun. 2019. JACoW Publishing. https://doi.org/10.18429/JACoW-IPAC2019-MOPTS026.

[20] B. Marchetti, et al. SINBAD-ARES - a photo-injector for external injection experiments in novel accelerators at DESY. *Journal of Physics: Conference Series*, 1596:012036, jul 2020.

[21] A. R. Maier, et al. Decoding sources of energy variability in a laser-plasma accelerator. *Phys. Rev. X*, 10:031039, Aug 2020.

[22] Athena: Helmholtz ARD Distributed Test Facility, `https://www.helmholtz-ard.de/e26746/`.

[23] H. Wiedemann. *Particle Accelerator Physics*. Graduate Texts in Physics. Springer, 4th edition, 2015.

[24] A. van steenbergen. Recent developments in high intensity ion bean production and preacceleration. *IEEE Transactions on Nuclear Science*, 12:746–764, 1965.

[25] M. J. Rhee. Refined definition of the beam brightness. *Physics of Fluids B: Plasma Physics*, 4(6):1674–1676, 1992.

[26] P. Musumeci, High brightness beam science, FEIS workshop, 2013, Florida `https://bt.pa.msu.edu/FEIS2013/talks/musumeci.pdf`.

[27] E. D. Courant and H. S. Snyder. Theory of the alternating gradient synchrotron. *Annals Phys.*, 3:1–48, 1958.

[28] USPAS course material `https://uspas.fnal.gov/materials/13Duke/SCL_Chap3.pdf`.

[29] S. Cousineau, J. Holmes, Y. Zhang, Transverse Beam Optics, Part I USPAS, 2011 `https://uspas.fnal.gov/materials/11ODU/Lecture6_Transverse_Beam_Optics_1.pdf`.

[30] H. Wiedemann. *Particle Accelerator Physics.* 3rd edition, August 2007.

[31] T. Rao and D. H. Dowell. An engineering guide to photoinjectors, 2014.

[32] L. Serafini and J. B. Rosenzweig. Envelope analysis of intense relativistic quasilaminar beams in rf photoinjectors: A theory of emittance compensation. *Phys. Rev. E*, 55:7565–7590, Jun 1997.

[33] M. Ferrario, et al. Space Charge Effects. (arXiv:1601.05214. arXiv:1601.05214):331–356. 26 p, Jan 2016. 26 pages, contribution to the CAS - CERN Accelerator School: Advanced Accelerator Physics Course, Trondheim, Norway, 18-29 Aug 2013.

[34] K. Floettmann. Emittance compensation in split photoinjectors. *Phys. Rev. Accel. Beams*, 20:013401, Jan 2017.

[35] M. Borland. elegant: A Flexible SDDS-Compliant Code for Accelerator Simulation, APS LS-287, September 2000.

[36] J. Qiang, et al. Three-dimensional quasistatic model for high brightness beam dynamics simulation. *Phys. Rev. ST Accel. Beams*, 9:044204, Apr 2006.

[37] K. Floettmann. ASTRA - A Space Charge Tracking Algorithm, `http://www.desy.de/~mpyflo`.

[38] J. Zhu. *Design Study for Generating Sub-femtosecond to Femtosecond Electron Bunches for Advanced Accelerator Development at SINBAD.* Dissertation, University of Hamburg, 2017. Dissertation, University of Hamburg, 2017.

[39] B. Marchetti, et al. Compression of an Electron-Bunch by Means of Velocity Bunching at ARES. In *Proc. of International Particle Accelerator Conference (IPAC'15), Richmond, USA, 3-8 May, 2015*, pages 1472–1475, Geneva, Switzerland, May 2015. JACoW.

[40] J. Zhu, et al. Sub-fs electron bunch generation with sub-10-fs bunch arrival-time jitter via bunch slicing in a magnetic chicane. *Phys. Rev. Accel. Beams*, 19:054401, May 2016.

[41] D. Marx, et al. Simulation Studies for Characterizing Ultrashort Bunches Using Novel Polarizable X-band Transverse Deflection Structures. *Scientific Reports*, 9(19912):1–17, 2019.

[42] S. Jaster-Merz, et al. Development of a beam profile monitor based on silicon strip sensors for low-charge electron beams. *Journal of Physics: Conference Series*, 1596:012047, jul 2020.

[43] B. Marchetti, et al. Experimental demonstration of novel beam characterization using a polarizable x-band transverse deflection structure. *Scientific Reports*, 11, 2021.

[44] W. Leemans. High average power laser plasma accelerator project at desy. European Advanced Accelerator Conference, 2019.

[45] REGAE, `https://regae.desy.de/`.

[46] D. Lipka, et al. Resonator for Charge Measurement at REGAE. In *IBIC 2013*, pages 872–875, October 2013.

[47] K. Kamada, et al. Crystal growth and scintillation properties of ce doped $gd_3(ga, al)_5o_{12}$ single crystals. *IEEE Transactions on Nuclear Science*, 59(5):2112–2115, 2012.

[48] M. Daniel. *Characterization of Ultrashort Electron Bunches at the SINBAD ARES Linac* . PhD thesis, Hamburg, 2019.

[49] F. Lemery, et al. Overview of the ARES Bunch Compressor at SINBAD. In *Proc. 10th International Particle Accelerator Conference (IPAC'19), Melbourne, Australia, 19-24 May 2019*, number 10 in International Particle Accelerator Conference, pages 902–905, Geneva, Switzerland, Jun. 2019. JACoW Publishing. https://doi.org/10.18429/JACoW-IPAC2019-MOPTS025.

[50] Accelerator research and innovation for European science and society, `https://aries.web.cern.ch/`.

[51] Accelerator on a chip international program, `https://achip.stanford.edu/`.

[52] D. Cesar, et al. High-field nonlinear optical response and phase control in a dielectric laser accelerator. *Communications Physics*, 1, August 2018.

[53] E. Esarey, et al. Physics of laser-driven plasma-based electron accelerators. *Rev. Mod. Phys.*, 81:1229–1285, Aug 2009.

[54] M. Weikum et al. Improved Electron Beam Quality from External Injection in Laser-Driven Plasma Acceleration at SINBAD. In *Proc. of International Particle Accelerator Conference (IPAC'17), Copenhagen, Denmark, 14 to 19 May, 2017*, number 8 in International Particle Accelerator Conference, pages 1707–1710, Geneva, Switzerland, May 2017. JACoW. https://doi.org/10.18429/JACoW-IPAC2017-TUPIK013.

[55] E. Svystun, et al. Numerical Studies on Electron Beam Quality Optimization in a Laser-Driven Plasma Accelerator with External Injection at SINBAD for ATHENAe. In *Proc. 10th International Particle Accelerator Conference (IPAC'19), Melbourne, Australia, 19-24 May 2019*, number 10 in International Particle Accelerator Conference, pages 3628–3631, Geneva, Switzerland, Jun. 2019. JACoW Publishing. https://doi.org/10.18429/JACoW-IPAC2019-THPGW023.

[56] E. Svystun, et al. The Effect of the Transverse Beam Jitter on the Accelerated Electron Beam Quality in a Laser-Driven Plasma Accelerator with External Injection at SINBAD for ATHENAe.

In *Proc. 10th International Particle Accelerator Conference (IPAC'19), Melbourne, Australia, 19-24 May 2019*, number 10 in International Particle Accelerator Conference, pages 3624–3627, Geneva, Switzerland, Jun. 2019. JACoW Publishing. https://doi.org/10.18429/JACoW-IPAC2019-THPGW022.

[57] S. Yamin, et al. Final focus system for injection into a laser plasma accelerator. *Phys. Rev. Accel. Beams*, 24:091602, Sep 2021.

[58] S. Yamin, et al. Study for the alignment of focusing solenoid of ares rf gun and effect of misalignment of solenoid on emittance of space charge dominated electron beam. *Journal of Physics: Conference Series*, 1350:012014, nov 2019.

[59] S. Yamin, et al. Beam dynamics studies for beam focusing and solenoid alignment at SINBAD. *Journal of Physics: Conference Series*, 1067:032019, sep 2018.

[60] K. Kubo. Estimation of orbit change and emittance growth due to random misalignment in long linacs. *Phys. Rev. ST Accel. Beams*, 14:014401, Jan 2011.

[61] T. O. Raubenheimer. Estimates of emittance dilution and stability in high-energy linear accelerators. *Phys. Rev. ST Accel. Beams*, 3:121002, Dec 2000.

[62] M. Krasilnikov, et al. Beam-based procedures for rf guns. In *Proceedings of the 2005 Particle Accelerator Conference*, pages 967–969, 2005.

[63] C. Gulliford, et al. Demonstration of low emittance in the cornell energy recovery linac injector prototype. *Phys. Rev. ST Accel. Beams*, 16:073401, Jul 2013.

[64] C. Gulliford and I. Bazarov. New method for generating linear transfer matrices through combined rf and solenoid fields. *Phys. Rev. ST Accel. Beams*, 15:024002, Feb 2012.

[65] J. H. Park, et al. Experimental approaches of emittance dilution induced by misalignments in a photoinjector. In *Proceedings of FEL08*, FEL Conference, pages 247–250.

[66] I. Pinayev, et al. Using solenoid as multipurpose tool for measuring beam parameters. *Review of Scientific Instruments*, 92(1):013301, 2021.

[67] Danfysik, `https://www.danfysik.com/`.

[68] S. Chatterjee. *Regression analysis by example*. Wiley series in probability and statistics. Texts and references section. Wiley, New York, 3rd ed edition, 2000.

[69] Scanditronix for TWS solenoids, `https://www.scanditronix-magnet.se/`.

[70] E. Panofski, et al. Commissioning results and electron beam characterization with the s-band photoinjector at sinbad-ares. *Instruments*, 5(3), 2021.

[71] S. Yamin, et al. Design considerations for permanent magnetic quadrupole triplet for matching into laser driven wake field acceleration experiment at SINBAD. *Journal of Physics: Conference Series*, 1596:012010, jul 2020.

[72] S. Yamin et al. Design Considerations for Permenant Magnetic Quadrupole Triplet for Matching Into Laser Driven Wake Field Acceleration Experiment at SINBAD. In *Proc. 10th International Particle Accelerator Conference (IPAC'19), Melbourne, Australia, 19-24 May 2019*, number 10 in International Particle Accelerator Conference, pages 143–146, Geneva, Switzerland, Jun. 2019. JACoW Publishing. https://doi.org/10.18429/JACoW-IPAC2019-MOPGW027.

[73] F. Mayet. *Acceleration and Phase Space Manipulation of Relativistic Electron Beams in Nano- and Micrometer-Scale Dielectric Structure* . PhD thesis, Hamburg, 2019.

[74] W. Kuropka. *Studies towards Acceleration of Relativistic Electron Beams in Laser Driven Dielectric Microstructures* . PhD thesis, Hamburg, 2019.

[75] E. Panofski et al. Developing a 50 mev lpa-based injector at athena for a compact storage ring. In *presented at the 12th Int. Particle Accelerator Conf. (IPAC'21)*, page 1765. JACoW Publishing, May 2021.

[76] S. A. Antipov, et al. Design of a prototype laser-plasma injector for the desy-ii synchrotron, 2021.

[77] J. Zhu, et al. Sub-fs Electron Bunch Generation Using Magnetic Compressor at SINBAD. In *Proc. of International Particle Accelerator Conference (IPAC'15), Richmond, USA, 3-8 May, 2015*, pages 207–209, Geneva, Switzerland, May 2015. JACoW.

[78] C. I. Moore, et al. Electron Trapping in Self-Modulated Laser Wakefields by Raman Backscatter. *Physical Review Letters*, 79(20):3909–3912, 1997.

[79] U. Umstadter, et al. Laser Injection of Ultrashort Electron Pulses into Wakefield Plasma Waves. *Physical Review Letters*, 76(12):2073–2076, 1996.

[80] E. Esarey, et al. Electron Injection into Plasma Wake Fields by Colliding Laser Pulses. *Physical Review Letters*, 79(14):2682–2685, 1997.

[81] H. Kotaki, et al. Improvement of the Quality and Stability of Electron Bunch Using Countercrossing Laser Beam. *IEEE TRANSACTIONS ON PLASMA SCIENCE*, 36(4):1760–1764, 2008.

[82] C. I. Moore, et al. A Laser-Accelerator Injector Based on Laser Ionization and Ponderomotive Acceleration of Electrons. *Physical Review Letters*, 82(8):1688–1691, 1999.

[83] T. P. Rowlands-Rees, et al. Laser-driven acceleration of electrons in a partially ionized plasma channel. *Physical Review Letters*, 100:105005, 2008.

[84] B. B. Pollock, et al. Demonstration of a narrow energy spread, ~ 0.5 GeV electron beam from a two-stage laser wakefield accelerator. *Physical Review Letters*, 107:045001, 2011.

[85] M. Zeng, et al. Self-truncated ionization injection and consequent monoenergetic electron bunches in laser wakefield acceleration. *Physics of Plasmas*, 21:030701, 2014.

[86] L. L. Yu, et al. Two-color laser-ionization injection. *Phys. Rev. Lett.*, 112:125001, 2014.

[87] C. E. Clayton, et al. Ultrahigh-gradient acceleration of injected electrons by laser-excited relativistic electron plasma waves. *Phys. Rev. Lett.*, 70:37–40, Jan 1993.

[88] F. Amiranoff, et al. Observation of laser wakefield acceleration of electrons. *Phys. Rev. Lett.*, 81:995–998, Aug 1998.

[89] J. Hua, et al. External injection from a Linac into a LWFA with 100efficiency (Conference Presentation). In E. Esarey, et al., editors, *Laser Acceleration of Electrons, Protons, and Ions V*, volume 11037. International Society for Optics and Photonics, SPIE, 2019.

[90] A. R. Rossi, et al. The external-injection experiment at the sparclab facility. *Nuclear Instruments and Methods in Physics Research Section A: Accelerators, Spectrometers, Detectors and Associated Equipment*, 740:60 – 66, 2014. Proceedings of the first European Advanced Accelerator Concepts Workshop 2013.

[91] A. R. Rossi, et al. Plasma boosted electron beams for driving free electron lasers. *Nuclear Instruments and Methods in Physics Research Section A: Accelerators, Spectrometers, Detectors and Associated Equipment*, 909:54–57, 2018.

[92] P. A. Walker, et al. Horizon 2020 EuPRAXIA design study. *Journal of Physics: Conference Series*, 874:012029, July 2017.

[93] B. Zeitler. *Phase Space Linearization and External Injection of Electron Bunches into Laser-Driven Plasma Wakefields at REGAE.* Dissertation, Universität Hamburg, Hamburg, 2017. Dissertation, Universität Hamburg, 2016.

[94] Eupraxia, `http://www.eupraxia-project.eu/eupraxia-conceptual-design-report.html`.

[95] K. Halbach. Design of permanent multipole magnets with oriented rare earth cobalt material. *Nuclear Instruments and Methods*, 169(1):1 – 10, 1980.

[96] J. K. Lim, et al. Adjustable, short focal length permanent-magnet quadrupole based electron beam final focus system. *Phys. Rev. ST Accel. Beams*, 8:072401, Jul 2005.

[97] T. Mihara, et al. Super strong permanent magnet quadrupole for a linear collider. *IEEE Transactions on Applied Superconductivity*, 14(2):469–472, 2004.

[98] T. Eichner, et al. Miniature magnetic devices for laser-based, table-top free-electron lasers. *Phys. Rev. ST Accel. Beams*, 10:082401, Aug 2007.

[99] P. Ngotta, et al. Hybrid high gradient permanent magnet quadrupole. *Phys. Rev. Accel. Beams*, 19:122401, Dec 2016.

[100] F. Marteau, et al. Variable high gradient permanent magnet quadrupole (quapeva). *Applied Physics Letters*, 111(25):253503, 2017.

[101] X. Li, et al. Preserving emittance by matching out and matching in plasma wakefield acceleration stage. *Phys. Rev. Accel. Beams*, 22:021304, Feb 2019.

[102] R. Assmann and K. Yokoya. Transverse beam dynamics in plasma based linacs. *Nucl. Instrum. Meth. A*, 410:544–548, 1998.

[103] T. Mehrling, et al. Transverse emittance growth in staged laser-wakefield acceleration. *Phys. Rev. ST Accel. Beams*, 15:111303, Nov 2012.

[104] L. Schaper, et al. Longitudinal gas-density profilometry for plasma-wakefield acceleration targets. *Nuclear Instruments and Methods in Physics Research Section A: Accelerators, Spectrometers, Detectors and Associated Equipment*, 740:208 – 211, 2014. Proceedings of the first European Advanced Accelerator Concepts Workshop 2013.

[105] K. Floettmann. Adiabatic matching section for plasma accelerated beams. *Phys. Rev. ST Accel. Beams*, 17:054402, May 2014.

[106] I. Dornmair, et al. Emittance conservation by tailored focusing profiles in a plasma accelerator. *Phys. Rev. ST Accel. Beams*, 18:041302, Apr 2015.

[107] X. L. Xu, et al. Physics of phase space matching for staging plasma and traditional accelerator components using longitudinally tailored plasma profiles. *Phys. Rev. Lett.*, 116:124801, Mar 2016.

[108] K. V. Lotov. Efficient operating mode of the plasma wakefield accelerator. *Phys. Plasmas*, 12(5):053105, 2005.

[109] A. Ferran Pousa, et al. Wake-T: A Fast Particle Tracking Code for Plasma-Based Accelerators. *J. Phys. Conf. Ser.*, 1350(1):012056, 2019.

[110] M. P. Anania, et al. An ultrashort pulse ultra-violet radiation undulator source driven by a laser plasma wakefield accelerator. *Applied Physics Letters*, 104(264102), 2014.

[111] G. G. Manahan, et al. Characterization of laser-driven single and double electron bunches with a permanent magnet quadrupole triplet and pepper-pot mask. *New Journal of Physics*, 16(10):103006, oct 2014.

[112] R. Weingartner, et al. Imaging laser-wakefield-accelerated electrons using miniature magnetic quadrupole lenses. *Phys. Rev. ST Accel. Beams*, 14:052801, May 2011.

[113] M. Fuchs, et al. Laser-driven soft-x-ray undulator source. *Nature Physics*, 5:826–829, Nov 2009.

[114] G. Travish, et al. A pmq-based, ultra-short focal length, final focus system for next generation beam-radiation and beam-plasma experiments. *AIP Conference Proceedings*, 737(1):400–406, 2004.

[115] A. Ferran Pousa, et al. Compact multistage plasma-based accelerator design for correlated energy spread compensation. *Phys. Rev. Lett.*, 123:054801, Jul 2019.

[116] J. van Tilborg, et al. Free-electron lasers driven by laser plasma accelerators. *AIP Conference Proceedings*, 1812(1):020002, 2017.

[117] S. van der Meer. Improving the power efficiency of the plasma wakefield accelerator. Technical Report CERN-PS-85-65-AA. CLIC-Note-3, CERN, Geneva, 1985.

[118] M. Tzoufras, et al. Beam loading in the nonlinear regime of plasma-based acceleration. *Phys. Rev. Lett.*, 101:145002, Sep 2008.

[119] Smaract hexapods, `https://www.smaract.com/positioning_systems`.

[120] Radiabeam, private Discussion, `http://www.radiabeam.com`.

[121] CERN Accelerator school: Magnets, `https://cds.cern.ch/record/1158462/files/cern-2010-004.pdf`.

[122] P. Winkler. Electron Beam Focusing at the Laser Wakefield Accelerator LUX . Master's thesis, Hamburg, 2015.

C

List of Publications

- S. Yamin, et al. Final focus system for injection into a laser plasma accelerator, (2021) Phys. Rev. Accel. Beams, 24:091602, Sep 2021. https://doi.org/10.1103/PhysRevAccelBeams.24.091602
- S. Yamin, et al. A final focus system for injection into a laser plasma accelerator at the ARES linac, (2021) https://arxiv.org/abs/2102.08878.
- S Yamin et al, Design studies for permanent magnetic quadrupole triplet for matching into laser driven wake field acceleration experiment at SINBAD, J. Phys.: Conf. Ser. 1596 (2020) 012010 https://doi.org/10.1088/1742-6596/1596/1/012010
- S. Yamin et al, Study for the alignment of focusing solenoid of ARES RF gun and effect of misalignment of solenoid on emittance of space charge dominated electron beam, J. Phys.: Conf. Ser. 1350 (2019) 012014 https://accelconf.web.cern.ch/ipac2019/papers/mopgw028.pdf
- S. Yamin et al, Design Considerations for Permanent Magnetic Quadrupole Triplet for Matching Into Laser Driven Wake Field Acceleration Experiment at SINBAD, in Proc. of 10th Int. Particle Accelerator Conf. IPAC 2019, Melbourne, Australia. http://jacow.org/ipac2019/papers/mopgw027.pdf
- S. Yamin et al, Beam dynamics studies for beam focusing and solenoid alignment at SINBAD, J. Phys.: Conf. Ser. 1067 (2018) 032019 https://doi.org/10.1088/1742-6596/1067/3/032019
- E. Panofski et al, Commissioning Results and Electron Beam Characterization with the S-Band Photoinjector at SINBAD-ARES, Instruments 5 (2021) 18 https://doi.org/10.3390/instruments5030028
- B. Marchett et al, SINBAD-ARES - A photo-Injector for external injection experiments in novel accelerators at DESY, 2020 J. Phys.: Conf. Ser. 1596 012036 https://doi.org/10.1088/1742-6596/1596/1/012036
- E. Panofski et al, Status report of the SINBAD-ARES RF photoinjector and linac commissioning, in Proc. of IPAC2019, Melbourne, Australia http://jacow.org/ipac2019/papers/mopts026.pdf

- B. Marchetti et al, Status of the ARES RF gun at SINBAD: from its characterization and installation towards commissioning, in Proc. of IPAC2018, Vancouver, BC, Canada

  https://accelconf.web.cern.ch/ipac2018/papers/tupmf086.pdf

C

Acknowledgement

In my view, any doctoral candidate success is not only the result of his/her hard work, but one always get positive synergies from his/her supervisors, colleagues and the working environment in general. In that regard, I have been blessed with one of the most talented and supportive group of scientist the field has to offer. I would like to express deepest gratitude to my supervisor Dr. Ralph Assmann and Prof. Dr. Wolfgang Hillert for their guidance, support and encouragement throughout my doctoral journey. I would also like to acknowledge the support of my DESY mentor Dr. Barbara Marchetti for her guidance and wisdom as I have learnt a lot from her.

I would like to thank many people at DESY for their support and useful discussions. Special thanks are due to Dr. Klaus Floettmann for discussion and guidance. I would also like to thank Dr. Frank Mayet for discussion and help during this PhD. I would like to thank my colleagues in alphabetical order: Dr. Florian Burkart, Dr. Hannes Dinter, Dr. Farzad Jafarinia, Sonja Jaster-Merz, Dr. Angel Ferran Pousa, Dr. Willi Kuropka, Dr. Francois Lemery, Dr. Daniel Marx and Dr. Thomas Vinatier for providing advice, guidance and support. I would also like to thank ARES shift leaders for their support and collaborative work during the ARES beamtime. Working with such wonderful people is an honor for me and I am humbled by it every day. I would also like to thank DESY technical groups for their support during ARES operation.

Last but not the least, I would like to acknowledge my parents, siblings and friends for their moral support, encouragement and prayers. Special thanks goes to Nadeem, Rizwana, Asma, Nabeel, Najeeb and Mehwish. A big thank you to my husband Zeeshan and my children Arsheen and Ayyan for their love and for standing by me on this journey.

Eidesstattliche Versicherung

Hiermit versichere ich an Eides statt, die vorliegende Dissertationsschrift selbst verfasst und keine anderen als die angegebenen Hilfsmittel und Quellen benutzt zu haben. Die eingereichte schriftliche Fassung entspricht der auf dem elektronischen Speichermedium. Die Dissertation wurde in der vorgelegten oder einer ähnlichen Form nicht schon einmal in einem früheren Promotionsverfahren angenommen oder als ungenügend beurteilt.

DESY, Hamburg. 21.12.2021

Ort, Datum

Unterschrift